University of Nevada, Reno

Tertiary Volcanic Rocks, Hydrothermal Alteration, and Epithermal Precious Metal Deposits of the Patterson Mining District, Sweetwater Mountains, Mono County, California and Lyon County, Nevada

A thesis submitted in partial fulfillment of the requirements for the degree of Master of Science in Geology

by
Carli H. Balogh

Dr. Peter G. Vikre/Thesis Advisor

December, 2016

THE GRADUATE SCHOOL

We recommend that the thesis
prepared under our supervision by

CARLI H. BALOGH

Entitled

Tertiary Volcanic Rocks, Hydrothermal Alteration, And Epithermal Precious Metal Deposits Of The Patterson Mining District, Sweetwater Mountains, Mono County, California And Lyon County, Nevada

be accepted in partial fulfillment of the
requirements for the degree of

MASTER OF SCIENCE

Dr. John L. Muntean, Advisor

Dr. Peter G. Vikre, Committee Member

Dr. Thom Seal, Graduate School Representative

David W. Zeh, Ph.D., Dean, Graduate School

December, 2016

i. Abstract

The Sweetwater Mountains (Mono County, California and Lyon County, Nevada) contain a basement complex of felsic plutons of the Sierra Nevada batholith and overlying roof pendants and septa of metasedimentary and metavolcanic rocks that are unconformably overlain by Miocene-Pliocene volcanic rocks and Tertiary-Recent surficial deposits. The mountain range is situated in the Walker Lane, a zone of transtension and shear deformation that accommodates the transition of the Pacific-North American plate margin from a convergent margin to the north to a strike-slip margin to the south. Volcanic rocks of the Sweetwater Mountains belong to the western andesite assemblage, a subduction-related continental margin arc that erupted mostly within the Walker Lane in the southern part of the arc, forming the ancestral Cascade Mountains. The western andesite assemblage hosts both low-sulfidation and high-sulfidation epithermal mineral deposits related to ancestral Cascades volcanic activity.

The Patterson mining district in the Sweetwater Mountains produced 4.5 Moz. of silver, 3,000 oz. of gold, and 35,000 lb. of copper during the 1880s-1940s from low-sulfidation epithermal silver-gold deposits that occur in veins and silicified breccias, mostly in Tertiary volcanic rocks. Goals of this study included producing a geologic map of the district and determining time-space relationships between volcanism and hydrothermal activity. The spatial and temporal relationships between Tertiary volcanism and hydrothermal mineral assemblages in alteration zones and precious metal deposits in the Patterson district were established by determining stratigraphy, structure, mineralogy, and ages of Tertiary volcanic rocks, silver-gold deposits, and zones of hydrothermal alteration. A geologic map and map of hydrothermal mineral assemblages of the district were produced.

Tertiary volcanic rocks are high-K calc-alkaline and include small volume andesite flows, more voluminous dacite and rhyolite flows and domes, and associated tuffs, mudflows, volcaniclastic breccias, and block and ash flow deposits. Rhyolite and dacite units of the Sweetwater volcanic field, a late Miocene-early Pliocene felsic eruptive center, are ~6.6-5.3 Ma, based on dates of igneous minerals. Precious metal deposits and alteration zones formed during or after the later stages of felsic volcanism, based on dates of adularia and alunite that are ~5.6-5.1 Ma. Altered rocks and mineral deposits form three north-to-northeast trending zones which are interpreted to be high angle fault zones. Groups of precious metal deposits that form in these north-trending zones were named the Cameron belt, the Clinton belt, and the California Comstock belt by miners in the 1800s. These mineral belts exhibit different deposit styles, silver to gold ratios, geochemical signatures, mineralogy, and structure.

Deposits of the Cameron belt contain the highest gold grades in the district in disseminated mineralized zones. Deposits consist of chalcedonic quartz, minor adularia and calcite, pyrite, and minor acanthite, chalcopyrite, galena, molybdenite, and sphalerite. Pyrite often contains micron to sub-micron scale inclusions of mostly acanthite and galena, and minor sphalerite and molybdenite. Multiple partly eroded sinter terraces, and a geochemical signature which includes high concentrations of arsenic and antimony, support near surface formation of these deposits and association with hot springs. The Clinton belt deposits exhibit high concentrations of silver in zones of stockwork veins. Mineralized rocks are spatially associated with a rhyolite porphyry dike and contain

quartz, adularia, acanthite, hessite (Ag_2Te), base metal sulfides, chlorargyrite, and iron tellurite minerals. The geochemical signature includes high concentrations of copper, molybdenum, lead, tellurium, and zinc. Deposits of the California Comstock belt consist of stockwork vein zones and 1-3 m thick veins which contain pseudomorphs of quartz after bladed calcite. Vein samples contain quartz, adularia, bladed calcite, electrum, acanthite with up to 4 weight percent selenium, and minor hessite, chalcopyrite, and galena, and exhibit high concentrations of mercury and selenium.

Volcanic rocks and silver-gold deposits of the Patterson mining district belong to a small suite of ~7-5 Ma volcanic fields and low-sulfidation epithermal deposits in the Walker Lane. Volcanic rocks and low-sulfidation epithermal deposits of similar age to those in the Patterson district occur in the Como, Gilbert, Pine Nut, and Silver Peak districts. All of these volcanic rocks and precious metal deposits formed south of the southern edge of the subducting Farallon plate. In addition to the Patterson district, telluride minerals occur in other Walker Lane reported in precious metal deposits including veins in the Bodie, Bullfrog, Olingshouse, and Wahmonie districts.

Future work in the Patterson district could include more detailed structural mapping, dates of emplacement of deposits of the Cameron and California Comstock belts, Re-Os dating of molybdenite in a proposed porphyry Mo system, identification of gold minerals in the Cameron belt, and determination of δD and $\delta^{18}O$ values of gangue minerals in the Clinton belt deposits to determine if there was magmatic input in the system. Future work in the Walker Lane could include a more thorough investigation of low-sulfidation epithermal deposits which contain telluride minerals. Identifying the tectonic controls on

telluride-bearing precious metal deposits in the western andesite assemblage could help understanding of Au-Ag-Te deposits worldwide.

ii. Acknowledgements

Thank you to the Ralph J. Roberts Center for Research in Economic Geology (CREG) and the sponsors of the program for supporting my research assistantship. This project would not have been possible without the support of the CREG sponsors. Thanks to Dr. Peter Vikre for being an incredibly knowledgeable, supportive, and patient thesis advisor, for making several trips to the field which greatly increased my understanding of the geology, and for allowing me to work on a fantastic project in a beautiful area. I extend my gratitude to Dr. John Muntean for serving on my committee, helping with fieldwork, teaching me much of what I know about ore deposits, and giving a student from Michigan a chance. Thanks to Dr. Thom Seal for serving on my committee.

I would like to thank the many scientists who contributed to the geochronology section of this study, including Lisa Peters, Dr. Willis Hames, Dr. Christopher Holm-Denoma, and Dr. Robert Fleck. Thanks to Dr. John McCormack for aid with the Scanning Electron Microscope and reflected light microscopy, and to Dr. Joel DesOrmeau for helping with the Scanning Electron Microscope and always talking hockey with me. Ryan Anderson was extremely kind to provide a geodatabase which assisted greatly in drafting the geologic map. Fleetwood Koutz and Jerry Baughman both provided exploration reports and maps which aided greatly in the writing of this thesis.

I am deeply grateful for Rick Kauffman and Neil Pearson, who both provided assistance in the field in extremely rugged terrain and excellent discussions about geology. I will never forget the kindness shown to me by many folks on the Eastern Sierra, including Bill McClenney and Art at the “Sweetwater Hilton”, David and Betsy

Lewis, Clay, and Jeremey at the Sweetwater Ranch, Veronika and Alan at Paradise Shores RV Park, and many other people I met in Bridgeport and at Travertine Hot Springs. Between the meals shared, help with flat tires, and discussions about geology, travelling, and life, the many acts of kindness shown made this lone traveler feel not so lonely.

Thank you to my fellow graduate students, especially to my friends and CREG colleagues: Wilson Bonner, Steve Howell, Tyler Hill, Tracy Anderson, Micah Claypoole, Dave Freedman, Ajeet Milliard, Justin Milliard, Sergey Konyshev and Elizabeth Hollingsworth. I could not ask for a more fantastic group of people to share work, stories, and laughter with the past couple of years. Thank you especially to Patrick Quillen for tolerating my constant presence at the desk adjacent to his for 2.5 years. I am grateful for my roommate Claire Pfeiffer and her dog Eoin, Lauren Banish, Peter Chutcharavan, Neil Pearson, Andrew Sadowski, and Carol Zamora and their steadfast friendship and support. Lastly, thank you to my parents, Jerry Balogh and Lynn Halton, and the rest of my family for their love and support, which is always felt strongly even from 2,000 miles away.

iii. Table of contents

iv. List of tables

v. List of figures

I. Introduction

i. Location

The Sweetwater Mountains (Mono County, California and Lyon County, Nevada) are a north-south trending mountain range on the western edge of the Walker Lane that contain a large volume of hydrothermally altered rocks, including Pre-Tertiary metasedimentary and metavolcanic rocks, Mesozoic granitic rocks, and late Miocene to early Pliocene volcanic rocks. The range lies to the west of the Bodie Hills across Sweetwater Flat (Figs. 1, 2), through which the East Walker River flows. Peaks include Mt. Patterson (11,673 feet), Wheeler Peak, South Sister, Middle Sister, and East Sister (Fig. 2).

The silver-gold mining camps of Belfort, Clinton, and Kentuck arose due to prospecting and mining activity in the Patterson district in the mid-1800s. The Patterson mining district encompasses these camps and the entirety of the Sweetwater Mountains, but exploited silver, gold, and other metal deposits are mostly located on the eastern flank of the range north of Fryingpan Canyon and south of Sweetwater Canyon in an area of altered rocks with approximate dimensions of 6 miles north-south and 3 miles east-west. This area constitutes the part of the Patterson mining district described in this study. The district is accessed by driving north on California Road 182 from Bridgeport, California or south from Wellington, Nevada and subsequently turning west onto unimproved Forest Service roads near the Sweetwater Ranch.

ii. Tectonic setting

Subduction beneath the continental margin of the western U.S. initiated the Cordilleran magmatic arc in the Mid-Early Triassic (Dickinson, 2006). The oldest rocks in this part of western Nevada and eastern California, Triassic-Jurassic (?) metasedimentary and metavolcanic rocks deposited in a back arc basin (Dickinson, 2006), were intruded by felsic plutons of the Sierra Nevada batholith from 217-80 Ma (Chen and Moore, 1982). There was a lull in magmatic activity on the western edge of the continental margin from the Late Cretaceous-Eocene due to flat slab subduction that caused magmatism to move further east. Cenozoic magmatism associated with the rollback of the Farallon plate subsequent to flat slab subduction was active in the ancestral Cascades of western Nevada and eastern California from 30-3 Ma (du Bray et al., 2014).

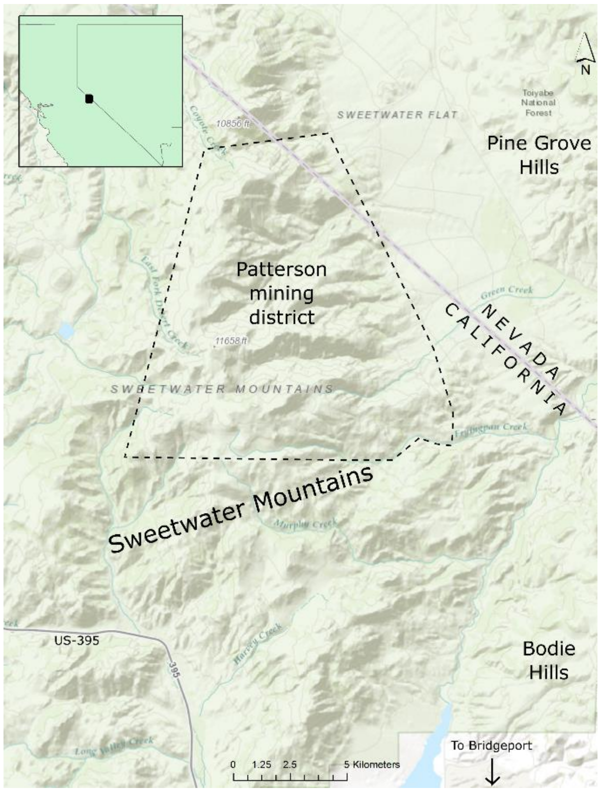

Figure 1. Location of the Patterson mining district, Sweetwater Mountains, and Bodie Hills in eastern California and western Nevada.

The volcanic rocks of the Sweetwater Mountains are a part of the western andesite assemblage, a subduction-related continental margin arc that erupted mostly within the

Walker Lane in the southern part of the arc, forming the ancestral Cascade magmatic arc (du Bray et al., 2014). The Walker Lane is a tectonic belt of transtension and shear deformation that accommodates the transition of the Pacific-North American plate margin from a convergent margin to the north to a strike-slip margin in the south. Stratovolcanoes, lava dome complexes, subvolcanic plutons, and associated volcaniclastic rocks are the common expressions of magmatism in the Walker Lane. Typical rock compositions in the southern Cascades magmatic arc are calc-alkaline andesite and dacite, with minor rhyolite (John, 2001). Magmas typically intruded dilatant zones caused by oblique faulting.

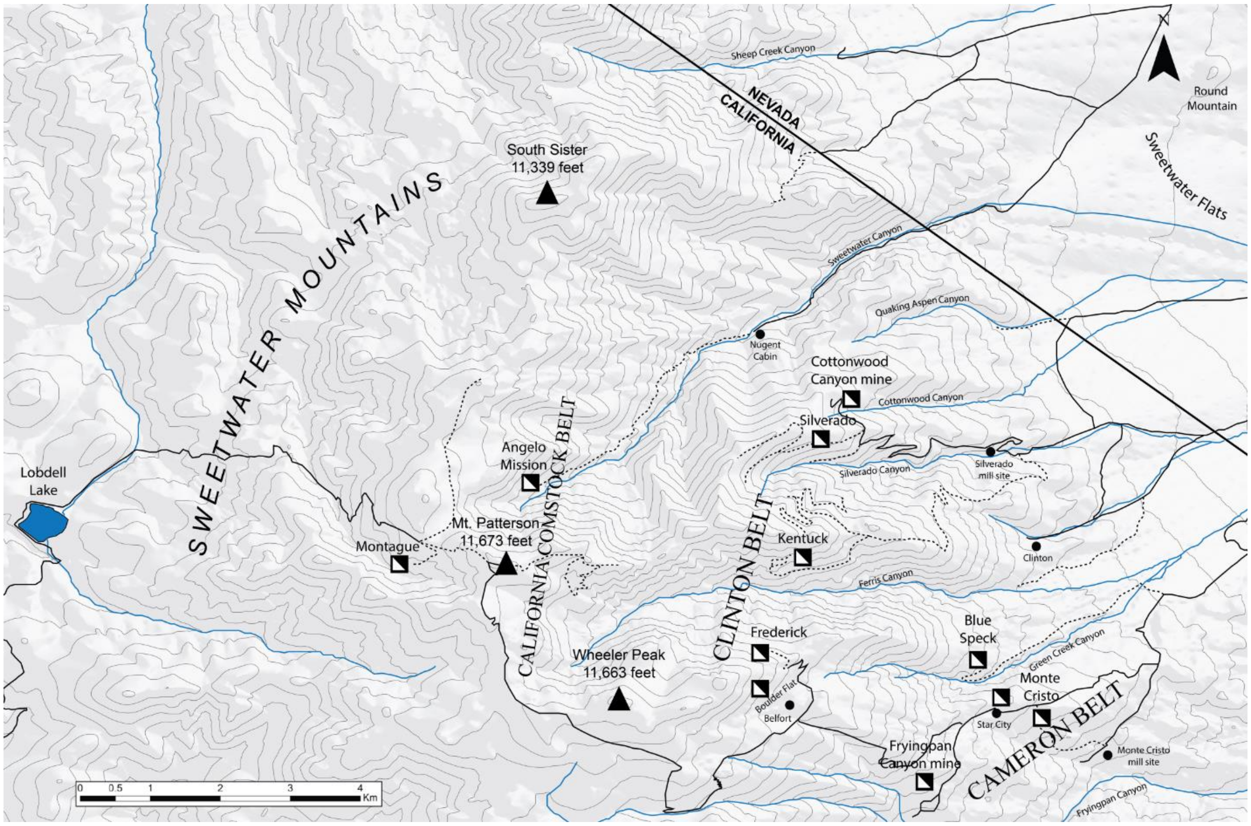

Figure 2. Index map of geographic place names in the Sweetwater Mountains. Solid lines are 4WD roads and dashed lines are jeep roads or pack roads. Creeks are shown in blue.

The western andesite assemblage hosts both low-sulfidation and high-sulfidation gold-silver-copper-mercury-sulfur deposits related to ancestral Cascades volcanic activity. Low-sulfidation epithermal deposits in part similar to those found in the Sweetwater Mountains include Bodie, Aurora, Rawhide, Tonopah, and the Comstock Lode (John, 2001), all of which are in the Walker Lane (Fig. 3). Magmatic-hydrothermal fluids and interaction with groundwater led to the deposition of metals in this type of deposit. While major Walker Lane faults are not likely to have been important for mineralization, extensional or transtensional second- or third-order structures may have been conduits for hydrothermal fluids.

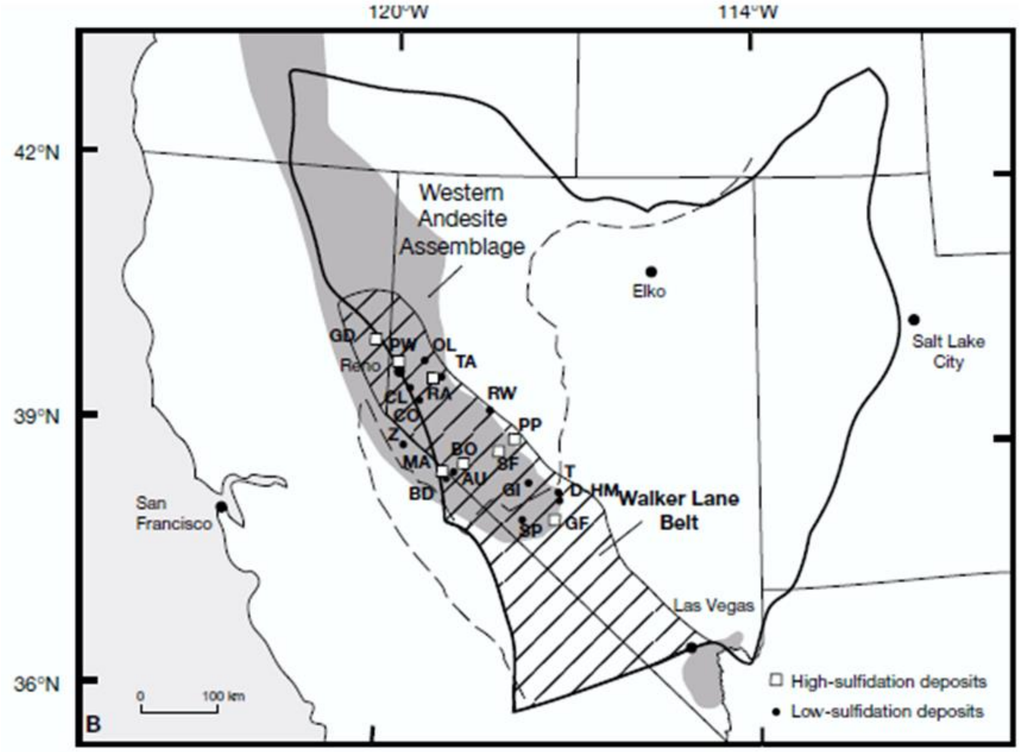

Figure 3. Map showing the distribution of western andesite assemblage rocks and associated gold-silver epithermal deposits in the Great Basin (black line). The shaded area is the western andesite assemblage and the area with diagonal lines is the Walker Lane. AU = Aurora, BD = Bodie, BO = Borealis, CL = Comstock Lode, CO = Como, D-HM = Divide-Hasbrouck Mountain, GD = Golden Dome, GF = Goldfield, MA = Masonic, OL = Olinghouse, PP = Paradise Peak, PW = Peavine-Wedekind, RA = Ramsey, RW = Rawhide, SF = Santa Fe, SP = Silver Peak, T = Tonopah, TA = Talapoosa, Z = Zaca (Monitor district). From John, (2001).

iii. Mining and exploration history

The Patterson mining district was established in 1860 and encompasses the entire Sweetwater range, but exploited mineral deposits are typically confined to the east slope of the range (Irelan and Whiting, 1888). Low-sulfidation epithermal silver-gold deposits in the Patterson district occur in veins and silicified breccias, mostly in Tertiary volcanic rocks. The recorded production of the district from 1860-1940s includes 4.5 Moz. of silver, 3,000 oz. of gold, and 35,000 lb. of copper, most of which was produced from the Silverado mine (Brem et al., 1983). Actual production was likely higher, based on scattered production records from other producers, such as the Kentuck and Monte Cristo mines. A small amount of molybdenum was also produced from a mine in Green Creek Canyon. Much of the molybdenum mineralization in the district could be related to the Mesozoic plutons in the district; however, testing this possibility was outside the scope of this investigation.

The Patterson district is poorly described in scientific literature. A report on the geology and mines of the district by Irelan and Whiting (1888) describes the existence of three minerals belts with varying amounts of gold and silver, and provides early production figures from the Kentuck and Monte Cristo mines. Other publications involving the Sweetwater Mountains include a Ph.D. dissertation on the geology of the Bridgeport quadrangle (Halsey, 1953), and a M.S. thesis describing the volcanic stratigraphy and structural setting of the northeastern part of the Patterson district with a 1:18,000 scale geologic map (Hunter, 1976). During the 1980s a former roadless area was assessed for mineral resource potential by the United States Geological Survey (USGS) and United States Bureau of Mines (USBM). As a part of this Roadless Area Review and

Evaluation (RARE II) assessment, a geologic map of the range at 1:62,500 scale (Brem, 1984), a report on chemical analyses of rocks, stream sediments, and heavy metal concentrates (Chaffee et al., 1983), and a mineral resource assessment and map which describes areas of high mineral potential and over 60 mines and prospects (Brem et al., 1983) were completed. An additional USBM report provides much of the same information (Lambeth, Campbell, and Scott, 1983). The Sweetwater Mountains were removed from roadless area designation in 1995 at the recommendation of the USGS, and there have been no geologic investigations since.

Several mining companies have explored the Wheeler Peak and Star City areas, including AMAX, Homestake, Golconda, Santa Fe, Fjordland, Minerva Exploration, Stuart Resources, and Placer Dome (Brem et al. 1983; F. Koutz, G. Baughman, personal communication). AMAX drilled through rhyolite altered to quartz-alunite near the top of Mt. Patterson for porphyry molybdenum deposits in the 1970s (Brem et al., 1983). Other companies explored for precious metal deposits, and one report called the Wheeler Peak area “one of the best untested bonanza-type occurrences in the western U.S” (Cannulli, 2003). At least three drill programs (Homestake Mining Company, Golconda Mining Corporation, and Minerva Minerals) targeted low grade, potentially bulk mineable precious metal mineralization in the Wheeler Peak and Fryingpan areas in the 1980s-2000s. Based on 8 shallow core holes and 16 rotary holes drilled in 1983-1985, Homestake Mining Company calculated a geological resource of 8 million tons at 0.024 troy ounces per ton (opt) Au within shallow, flat-lying deposits in the Upper Fryingpan area (Bybee, 1986). Golconda Mining Corporation drilled 109 short rotary holes in 1988-1992 and calculated a geological resource of 20 million tons at 0.025 opt Au in the Upper

Fryingpan Sinter target (Kowall, 1996). Interest in exploring the Patterson district waned after the early 2000s and there are currently few active mining claims in the Sweetwater Mountains.

iv. Scope and purpose

The purpose of this study was to determine the spatial and temporal relationships between Tertiary volcanism and hydrothermal mineral assemblages in alteration zones and epithermal precious metal deposits in the Patterson district. In order to accomplish this goal stratigraphy, structure, mineralogy, and ages of Tertiary volcanic rocks, silver-gold deposits, and alteration zones have been described and determined. Geologic mapping and mapping of hydrothermal mineral assemblages were employed to understand spatial and temporal associations. These relationships were compared to the volcanic stratigraphy and gold-silver deposits in the adjacent Bodie Hills and in other Tertiary volcanic fields in the Walker Lane to provide broader context for Tertiary precious metal deposits in the southern ancestral Cascades magmatic arc. The detailed characterization of Tertiary precious metal deposits in the Patterson district reported here will likely refine exploration concepts for epithermal precious metal deposits in the arc.

II. Methods

Geologic mapping focused on volcanic stratigraphy was conducted during the summers of 2015 and 2016 at 1:1000 scale in areas of highly altered rocks near mineral deposits and 1:3000 scale in less altered stratigraphy. Mapping was constrained to a region south of Sweetwater Canyon and north of Fryingpan Canyon, and east of the crest of the Sweetwater Mountains. This region (approximately 40 km^2) encapsulates the majority of the Patterson district and areas of altered rocks. Mapping was conducted using satellite imagery from Bing Maps with topographic overlays and a handheld global positioning system (GPS). The mapping was digitally compiled with ArcMap software.

Descriptions of volcanic rocks and hydrothermal minerals are based on field observations, petrography, short wave infrared spectrometry (SWIR), and scanning electron microscopy (SEM) of ~300 samples. Samples were initially cut into slabs and described using a binocular scope. Petrographic sections were made from selected slabs and hand specimens for characterization of volcanic rocks and hydrothermal mineral assemblages. Major and minor element concentrations were determined by various analytical techniques.

SWIR was used to identify fine-grained minerals in hydrothermally altered rocks that could not be distinguished by petrography. Spectra were recorded using an ASD TerraSpec and analyzed with SpecWin software. Igneous and hydrothermal minerals were also identified in thin section by petrography and SEM. Photomicrographs of thin sections were captured using integrated software from Olympus. Images captured with a JEOL 6010 tungsten filament SEM revealed mineral identities and atomic proportions of minerals (i.e. electrum) that were determined using integrated software.

Several igneous and hydrothermal minerals were dated by the $^{40}Ar/^{39}Ar$ and U-Pb methods. Two $^{40}Ar/^{39}Ar$ dates of alunite were determined by the USGS prior to this study. Additional $^{40}Ar/^{39}Ar$ dates were obtained by laser fusion and incremental heating methods. Three samples (RSW-JM004, RSW-CB002b, RSW-CB011a) were separated and dated at the New Mexico Geochronology Research Laboratory. Four samples (RSW-056, RSW-165, RSW-177, RSW-199) were dated at the Auburn Noble Isotope Mass

Analysis Laboratory, following crushing and processing with a Franz magnetic separator and heavy liquids. Mineral separates were irradiated with neutrons in a reactor, and were cooled for a month. Radiogenic ^{40}Ar and ^{39}Ar produced by neutron bombardment of ^{39}K were measured by mass spectrometry, using Fish Canyon Tuff as a standard (McDougall and Harrison, 1999). Separates were laser-fused or step-heated to release radiogenic Ar. For separates analyzed by step heating, plateau ages were defined where sets of incremental heating steps included more than 50% of total ^{39}Ar release, and in which no difference in age is observed between any two steps at the 95% confidence interval (Fleck et al., 1977). Plateaus indicate that the Ar system was undisturbed during initial cooling, while a lack of plateau indicates Ar loss or gain (McDougall and Harrison, 1999). Laser fusion releases all Ar from the sample in a single step and provides total gas dates. Weighted mean ages are calculated for each sample, with uncertainties reported as one standard error of the weighted mean (Renne et al., 2009).

Zircon crystals from two samples were dated using the U-Pb method at the USGS Central Mineral and Environmental Resources Center. Laser ablation inductively coupled plasma mass spectrometry (LA-ICP-MS) of individual zircons and statistical methods are used to determine ages of rock crystallization. The U-Pb method relies on the radiogenic decay of ^{238}U to ^{206}Pb, ^{235}U to ^{207}Pb, and ^{232}Th to ^{208}Pb (Gehrels et al., 2008). The ICP-MS records concentrations of these isotopes, and Pb isotopic ratios are used to calculate zircon dates, which are commonly plotted on a concordia diagram for evaluation of Pb loss.

Geochemical analysis of altered and unaltered rocks was conducted by ALS Minerals and SGS Mineral Services using several multi-element analytical methods.

Fifty-four altered/mineralized samples and 22 unaltered igneous rocks were analyzed. Methods used on altered rocks include fire assay for Au, cold vapor atomic absorption for Hg, and inductively coupled-mass spectrometry (ICP-MS) and inductively coupled plasma atomic emission spectroscopy (ICP-AES) for all other elements (Ag, Al, As, Ba, Be, Bi, Ca, Cd, Ce, Co, Cr, Cs, Cu, Fe, Ga, Ge, Hf, In, K, La, Li, Mg, Mn, Mo, Na, Nb, Ni, P, Pb, Rb, Re, S, Sb, Se, Sn, Sr, Ta, Te, Th, Ti, Tl, U, V, W, Zn, and Zr). ICP-AES was also used on samples that contained >100 ppm Ag using ICP-MS. SGS Mineral Services utilized hydride atomic absorption spectroscopy for Se and Te. Unaltered igneous rocks were analyzed by fused disc X-ray fluorescence (XRF) for major elements and major element oxides (Al_2O_3, BaO, CaO, Cr_2O_3, Fe_2O_3, K_2O, MgO, MnO, Na_2O, P_2O_5, SrO, and TiO_2), by combustion furnace for C and S, and by ICP-MS and ICP-AES for all other elements.

III. Geology and Volcanic Stratigraphy

i. Geology of the Sweetwater Mountains

Rocks in the Sweetwater Mountains include a basement complex of Mesozoic felsic plutons (mostly quartz monzonite), and overlying roof pendants and septa of metamorphic rocks, that are overlain unconformably by Miocene-Pliocene volcanic rocks and late Tertiary-Quaternary surficial deposits. Plutons intruded a Mesozoic (?) volcanic and sedimentary sequence of sandstone and micritic limestone with locally interbedded shale, which are overlain by intermediate lava flows and tuffs (Brem, 1984; Hunter, 1976). Some of the limestone has been metamorphosed to marble, presumably during intrusion of the felsic plutonic rocks. These sedimentary and volcanic rocks are thought to be part of the middle Triassic-middle Jurassic Pine Nut Assemblage (Manuszak et al., 2000). In the Sweetwater roof pendants, these rocks are altered to epidote and chlorite, and the limestone locally contains pyrite, chalcopyrite, and bornite (Hunter, 1976). They were intruded by Jurassic quartz monzonite of the Sierra Nevada batholith (C. Holm-Denoma, written communication, 2016).

Multiple felsic plutons occur within the Sweetwater Mountains, and have been described as the Granite of East Fork, Granite of Belfort, and the Granite of Green Creek, among others (Brem, 1984). Plutonic rocks in the Sweetwater Mountains have been dated as Cretaceous in past studies (Schweickert, 1976). These plutonic rocks are part of the Sierra Nevada batholith; which typically range from granite to tonalite (Bateman, 1992). Both quartz monzonite and amphibolitized granodiorite occur in the Patterson mining district. However, granodiorite occurs only as two small exposures near Boulder Flat, and has been grouped with quartz monzonite in this study (unit Jqm). Quartz monzonite typically is medium- to fine-grained with purple orthoclase phenocrysts and a groundmass of 20% quartz, 10-20% orthoclase, 35-40% plagioclase, and 10-15% hornblende (Fig. 4). Milky quartz veins, aplite dikes, and pegmatites occur locally in the quartz monzonite. Quartz monzonite is often propyliticly altered to epidote + albite + chlorite + montmorillonite, and to quartz + sericite + pyrite adjacent to faults and joints. The erosional surface on which Tertiary volcanic rocks erupted upon in the Sweetwater Mountains exhibited significant relief, based on several lines of evidence. Tertiary volcanic rocks show no signs of having been rotated by faulting, and few faults with significant displacements occur. Rhyolite, dacite, and andesite eruptive centers occur at elevations of 11,563 feet to 7,800 feet. Flow banding attitudes of several rhyolite units consistently dip moderately east, which may be the result of eruption onto a non-horizontal, east dipping erosional surface. Attitudes of volcaniclastic sediments, water lain tuffs, and sinter vary and may be the result of tilting or magmatic inflation. A thin veneer of Tertiary volcanic rocks (likely <250 m, based on exposures in deeply eroded canyons) erupted onto the Mesozoic quartz monzonite erosion surface. Tertiary volcanic strata consist of rhyolite, trachydacite, trachyandesite, and basaltic andesite, as well as associated tuffs, mudflows, volcaniclastic breccias, and block and ash flow deposits (Plate I). Most Tertiary rocks have been highly altered by hydrothermal fluids. Young surficial deposits, including Tertiary-Recent landslide, talus, and alluvial fan deposits, cover a significant area of bedrock in the range, and Sweetwater Flat to the east (Plate I).

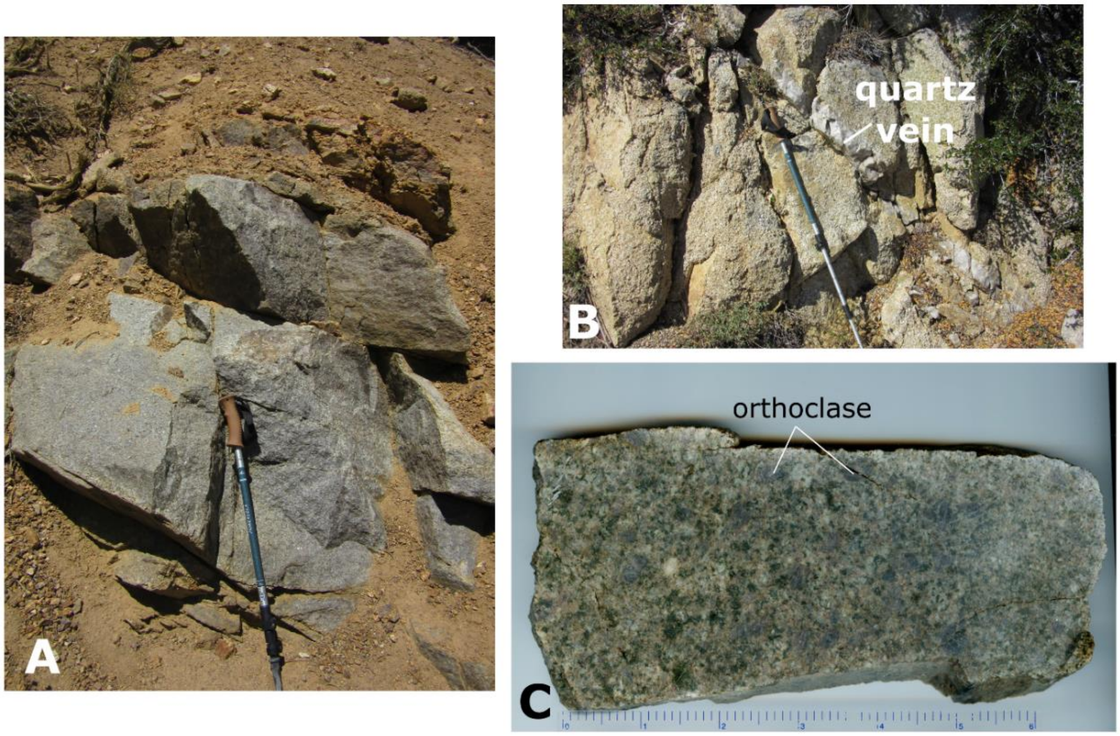

Figure 4. Quartz monzonite (Jqm). A.) Typical outcrop of quartz monzonite, trekking pole for scale. B.) Milky quartz vein cutting propyliticly altered quartz monzonite. C.) Hand sample of equigranular quartz monzonite. Scale is in inches.

ii. Stratigraphy of Tertiary volcanic rocks

Surface mapping revealed that Tertiary volcanism generally consists of heterogeneous, small volume effusive flows and domes that nonconformably overlie Jurassic quartz monzonite (Plate I). Eight rhyolite units and four dacite units make up the Sweetwater volcanic field, a late Miocene to early Pliocene group of felsic eruptive rocks. The middle Miocene trachyandesite of Masonic (John et al. 2015), here mapped as hornblende trachyandesite (Tac), is the oldest Tertiary volcanic rock in the district, based on a $^{40}Ar/^{39}Ar$ date (Table 1). The flow of hornblende trachyandesite (Tac) is thought to have originated in the Bodie Hills; all other Tertiary volcanic rocks appear to have erupted from vents in the Sweetwater volcanic field. The general progression of late Miocene-early Pliocene volcanism in the Sweetwater Mountains is initial eruption of trachyandesite (Tab), followed by eruption of dacite, and then widespread, more voluminous eruptions of rhyolite.

Most flows of porphyritic trachyandesite (Tab) are small volume erosional remnants and occur in contact with underlying quartz monzonite, with the exception of a large intrusion of andesite that occurs on Wheeler Peak. This andesite was previously mapped as Relief Peak formation based on mineralogy and stratigraphic relationships with the overlying ~9.3 Ma Stanislaus Formation to the west of the Patterson district (Brem, 1984). The Relief Peak formation is a 16-10 Ma assemblage of andesite lava flows and mudflow breccias that is sourced from south of Sonora Pass (Roelofs et al., 2004). It is unknown if porphyryitic trachyandesite (Tab) in the Sweetwater Mountains is the same age as the Relief Peak Formation. Flow foliation plane measurements generally dip to the south, indicating that the small-volume andesite flows seem to be local to the

Sweetwater Mountains. The source of the flows is possibly near South Sister (Brem, 1984). Most dacite units are also small-volume, with the exception of large domes and flows of porphyritic trachydacite (Td) that form both the south and north rims of Sweetwater Canyon.

Rhyolite flows and domes are the most voluminous volcanic rocks, and at least seven rhyolite units with distinct chemistry, mineralogy, and texture occur in the mapped area. Fissile flow-banded rhyolite (Tra) and associated rhyolite tuff-breccia (Trt) are the most widespread units in the district. Consistent east-dipping flow banding in several rhyolite units suggests that rhyolite flows originated at higher elevations and flowed eastward to lower elevations. Emplacement of rhyolite dikes (and possibly domes) was controlled by north-south trending faults, based on the north-south strike of rhyolite porphyry dike (Trp) and glassy rhyolite dikes associated with flow-banded porphyritic rhyolite (Trc).

Clast rich tuff-breccia (Tbx3) is inferred to have been deposited in a northeast-southwest trending depression near Star City. This unit includes water-lain crystal tuff beds, lake sediments, and cm-scale pockets of silica sediments that show syn-sedimentary deformation. It is overlain by three small, partly to entirely dismembered sinter terraces. This basin-filling unit (Tbx3) was silicified and now forms inverted topography in the Star City and upper Fryingpan Canyon areas. Local hydrothermal breccias (Tbx4), defined as breccias that contain elongated clasts of underlying rock units in quartz + iron oxide ± pyrite matrices, occur in this area and south of Wheeler Peak.

Landslides are common because of instability of steep slopes. These landslides are thought to be Tertiary-Quaternary because some are eroded, highly vegetated, and do not exhibit hummocky geomorphic forms typical of recent slides, whereas other landslides cover historic mine roads and thus occurred in the past century. A large landslide above Fryingpan Canyon has caused a slide block with mineralized clast-rich tuff breccia and sediments (Tbx3) to be displaced to lower elevations. Another landslide block forms Boulder Flat and exposed a rhyolite porphyry dike (Trp) on the steep hillside west of Belfort. Steep slopes also prevented access to Ferris Canyon, and some felsic volcanic units were mapped using satellite imagery as Tu- “Tertiary undifferentiated”.

Cross sections were constructed to illustrate stratigraphic relationships, structures, and volumes of volcanic rocks of the Sweetwater volcanic field. Cross-sections are schematic and unit thicknesses are estimated in many cases (Plate I). Cross-sections illustrate that Tertiary volcanic rocks range from <10 m to ~200 m in thickness and consist of both flows and domes. A maximum thickness of 500 m is possible, but the depth to basement rock is unknown for much of the map. Cross section C-C’ shows that volcanic units do not form continuous north-south trends.

iii. Classification of Tertiary volcanic rocks

Field characteristics, petrography, and geochemical analyses (Appendix A) provide the basis for classification of Tertiary volcanic rocks in the Sweetwater Mountains. Most Tertiary volcanic rocks belong to the high-K calc-alkaline to shoshonitic series (Fig. 5). The largest volumes of volcanic rocks are trachydacite and rhyolite; trachyandesite and

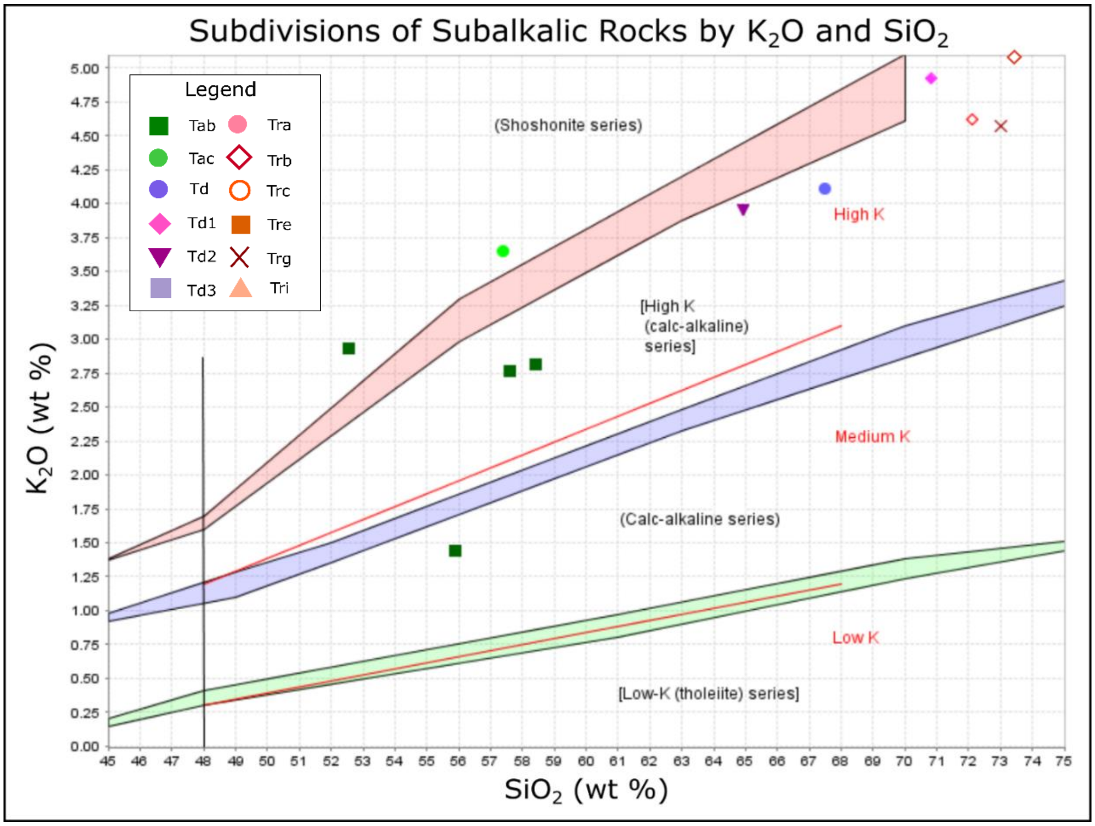

Figure 5. Subdivisions of subalkalic rocks by SiO_2 (weight percent) vs. K_2O (weight percent). Tertiary volcanic rocks of the Patterson mining district belong to the high K calc-alkaline and shoshonite series. Subdivision boundaries from two classification schemes are shown. Subdivisions of (Le Maitre et al., 1989) include the red lines and text. Shaded bands and black text are fields in which boundary lines from several studies fall, as summarized by (Rickwood, 1989). The SiO_2 and K_2O data are in Appendix A. See text for description of units symbolized along the left side of the diagram.

basaltic trachyandesite are volumetrically minor (Fig. 6). Andesites generally contain hornblende and plagioclase phenocrysts, with minor quartz biotite phenocrysts, in and dark grey to light grey-green matrices. There are often small volumes of lithified mud flows associated with andesite flows. Dacites typically contain sanidine, biotite, and hornblende phenocrysts, but some contain quartz and plagioclase phenocrysts. Dacite matrices are typically dark to light purple, some are glassy, and flow banding is not well-developed. Rhyolites typically contain sanidine, quartz, and biotite phenocrysts but some also contain plagioclase and hornblende. Anatase, sphene, zircon, and primary (magmatic) monazite often occur as accessory phases in rhyolites. Rhyolites form flows and domes with well-developed flow banding, and some rhyolite contains abundant spherulites. Rhyolites often have a glassy matrix and are purple, red-purple, grey, or green.

Effort was made to analyze unaltered or the least altered volcanic rocks (Appendix A); however, some analyzed volcanic rocks have likely experienced loss of cations such as Na^+, K^+, and Ca^{2+} and gain of Si^{4+} because of extensive hydrothermal alteration. Andesites are metaluminous and rhyolites and dacites are weakly to strongly peraluminous (Fig. 7). Rare earth element (REE) spider diagrams are useful in distinguishing generations of volcanism and chemistry of source magmas (Fig. 8). Andesites have a higher concentration of REEs, whereas dacites and rhyolites have lower REE concentrations. Rhyolite units Tra, Trc, and Trg all show a pronounced negative europium anomaly, which results from substitution of Eu^{2+} into plagioclase in plagioclase-stable source melts (Winter, 2009). Thus, the melts that generated rhyolites originated from shallow depths (<40 km).

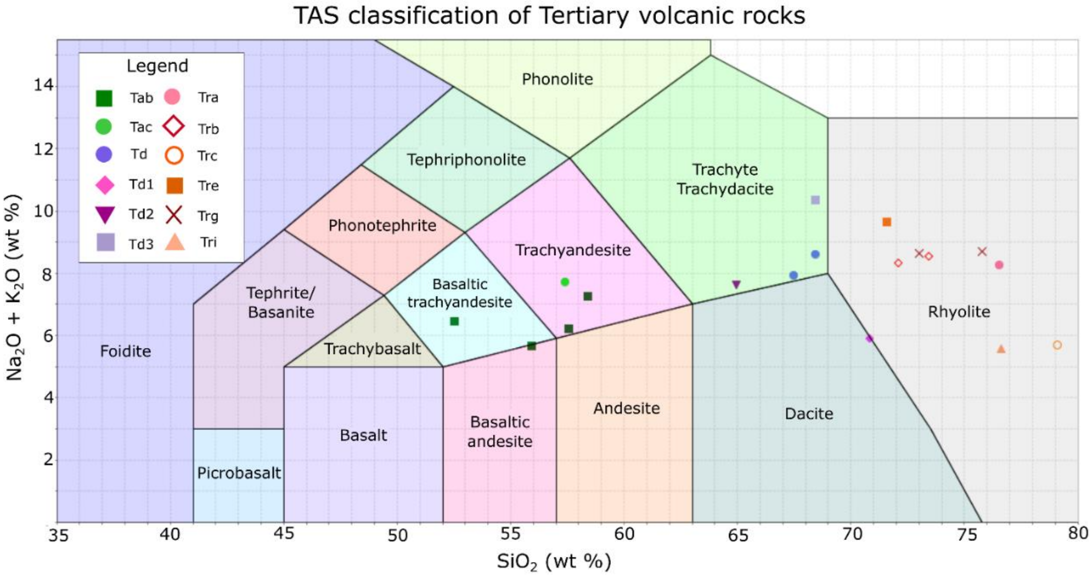

Figure 6. Total alkali vs. silica (TAS) diagram for Tertiary volcanic rocks of the Patterson mining district. Divisions are from (Le Maitre et al., 1989). See text for description of units symbolized along the left side of the diagram.

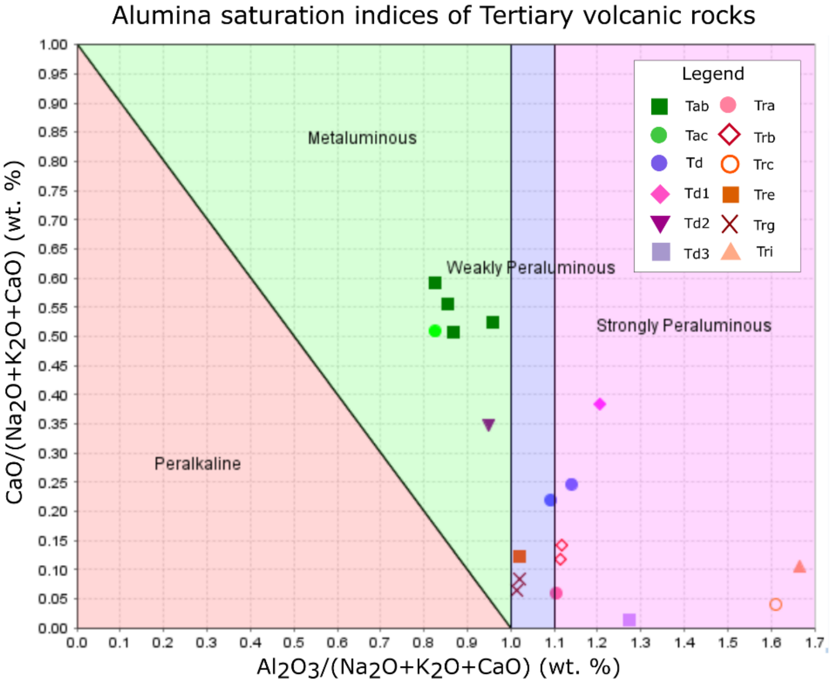

Figure 7. Alumina saturation defined by Al_2O_3/ (Na_2O + K_2O + CaO) vs. (CaO/(Na_2O + K_2O + CaO), weight percent. Andesites (Tab, Tac) are metaluminous, while dacites and rhyolites (Td, Td1, Td2, Td3, Tra, Trb, Trc, Tre, Trg, Tri) are weakly to strongly peraluminous, while dacites and rhyolites (Td, Td1, Td2, Td3, Tra, Trb, Trc, Tre, Trg, Tri) are weakly to strongly peraluminous. Divisions are from (Barton and Young, 2002). See text for description of units symbolized along the right side of the diagram.

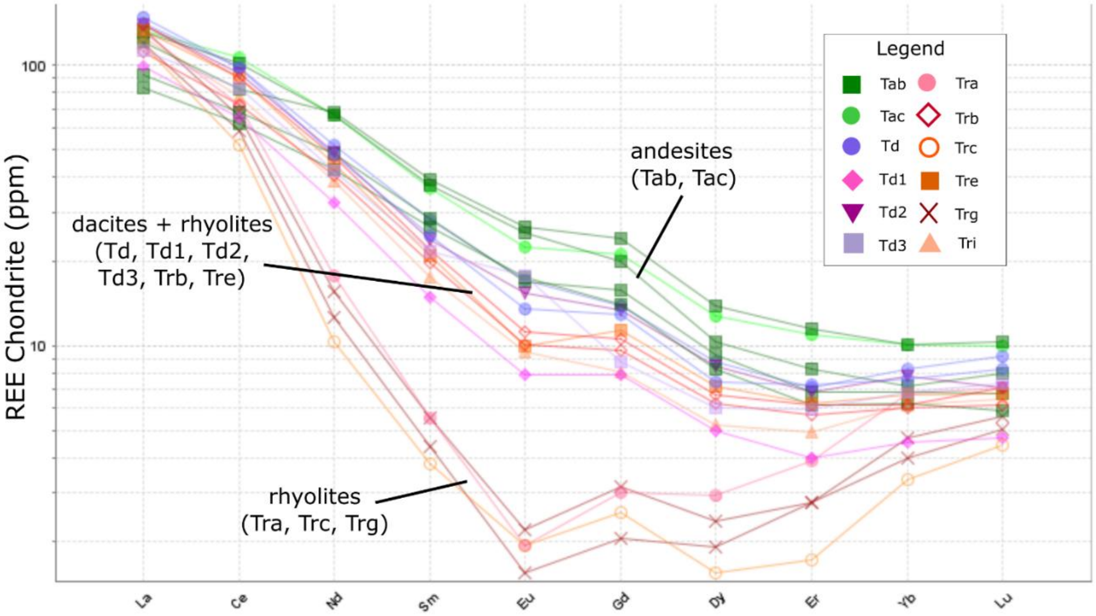

Figure 8. Rare-earth element (REE) chondrite spider diagram (Nakamura, 1973), for Tertiary volcanic units. Rhyolites (Tra, Trc, and Trg) exhibit a negative europium anomaly. See text for description of units symbolized along the right side of the diagram.

iv. Description of Tertiary units

Age relationships between units were determined by field relationships and isotopic dating. However, the lack of exposed contacts between units, occurrence of isolated units, and lack of isotopic dates for many units causes uncertainty in their position within the Tertiary stratigraphic section. Tertiary volcanic units differ greatly in the northern and southern portions of the map and separate stratigraphic columns were determined for each area (Plate I). Herein, the northern portion of the map refers to north of Ferris Canyon, and the southern portion of the map is south of Ferris Canyon (Fig. 2). Tertiary units from oldest to youngest in the northern and southern halves of the map, are described below (Plate I):

Northern half of the map:

- Tab is a fine-to-medium grained porphyritic trachyandesite that contains corroded <4 mm hornblende phenocrysts (2-5%), and laths of 1-5 mm plagioclase phenocrysts (5-10%) in an aphanitic groundmass. It is black to purplish to blue-greenish. The weathered surfaces are often reddish to purple because of staining by iron oxides. This unit can be locally vesicular. There are often small volume andesitic lahars associated with exposures of this unit. The age of the fine-to-medium grained porphyryitic trachyandesite (Tab) is unknown, but it is older than all rhyolites and dacites.
- Td2 is a dark red to purple trachydacite that consists of 2-4 mm feldspar (5%), 2-4 mm hornblende (2%), and locally 1-2 mm biotite (1%) phenocrysts in a quartz and feldspar-rich groundmass which contains irregular, black glassy layers.
- Td is a porphyritic trachydacite which consists of 2-6 mm sanidine phenocrysts (10%) and 1-3 mm biotite and hornblende phenocrysts (3%). It is purple-grey and often flow-banded, with steep attitudes. Vertical jointing is common in cliffs of this unit in Sweetwater Canyon. (Fig. 9)

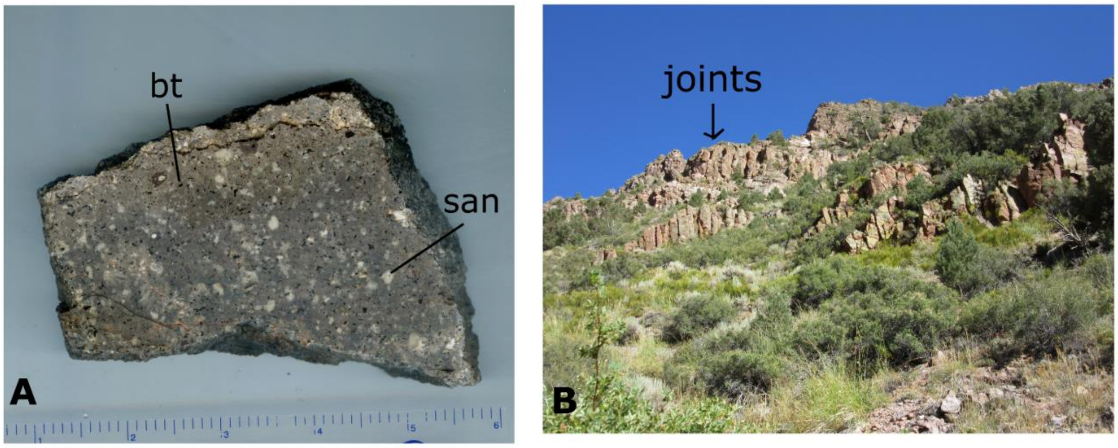

Figure 9. Unit Td, a porphyritic, purple grey trachydacite with sanidine (10%) and biotite and hornblende (3%). A.) Hand sample showing biotite (bt) and sanidine (san) phenocrysts that were dated by the $^{40}Ar/^{39}Ar$ method. Scale is inches. B.) Vertical jointing in cliffs of Td on the south side of Sweetwater Canyon.

- Trd is a very fine-grained, almost aphanitic, silicified to clay-altered rhyolite which consists of <1 mm quartz (1%), 2 mm sanidine (1%), 2 mm biotite (1%), and 3 mm plagioclase (2%) phenocrysts, and locally 3 mm hornblende phenocrysts (< 2%). All phenocrysts except for quartz are leached from intense hydrothermal alteration in Silverado Canyon, leaving voids. There is local columnar jointing in this unit.
- Trp is a green-grey coarsely porphyritic rhyolite which contains 0.5-2 cm sanidine (2-4%), 1 mm plagioclase (1%), and 1-3 mm biotite (5%) phenocrysts with accessory sphene in a quartz-rich groundmass. Biotite glomerocrysts occur locally. This unit includes a >8 m wide dike, heavily silicified and altered. Weathered exposures of the dike are dark brown to black from iron oxides, and contain 2 cm sanidine (4%) crystals that in part have been removed by weathering, leaving distinctive rectangular cavities in the rock. (Fig. 10)

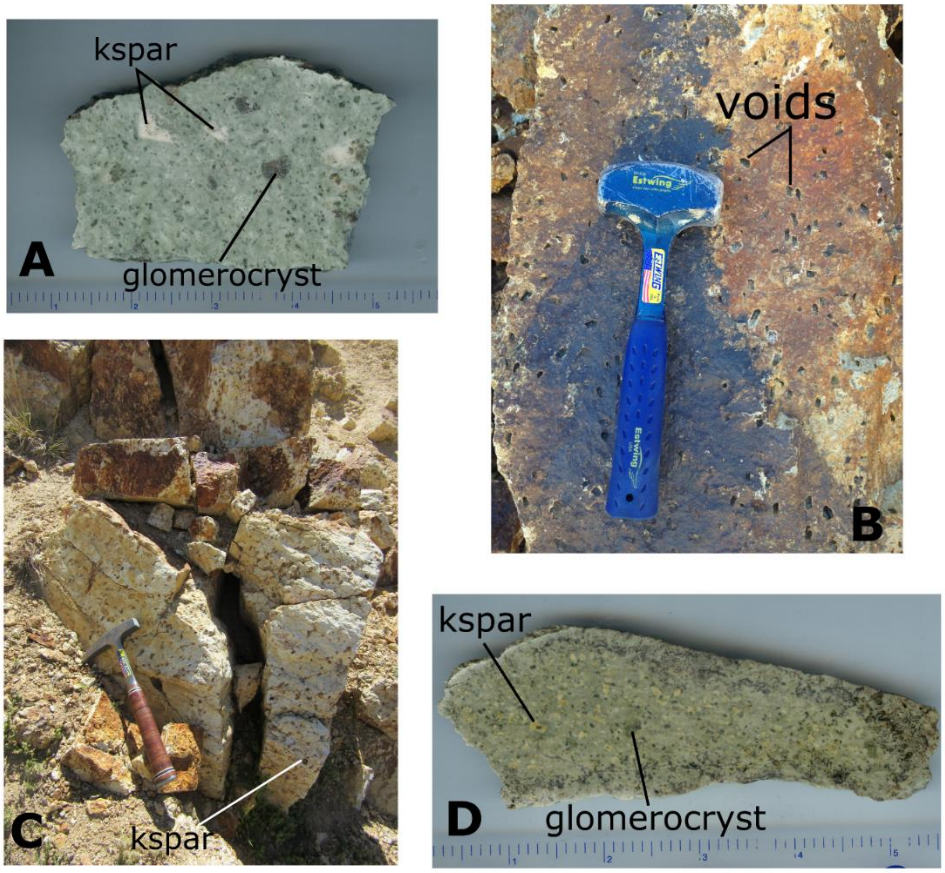

Figure 10. Unit Trp, a grey-green coarsely porphyritic rhyolite with sanidine phenocrysts. A.) Silicified, potassium feldspar-megacrystic Trp dike. The dike contains sanidine (kspar) crystals up to 3 cm and glomerocrysts of mostly biotite. B.) The Trp dike is stained brown to black on weathered surfaces and often contains rectangular voids of sanidine removed by weathering. C.) Outcrop of Trp dike that has been argillized. D.) Finer-grained Trp with a green groundmass and smaller feldspar crystals that may represent a part of the dike with smaller phenocrysts. A and D scale is inches.

- Tu is an undifferentiated rhyolite or dacite unit which occurs in Ferris Canyon.
- Tra is a flow-banded, fissile rhyolite which consists of <3 mm quartz and feldspar phenocrysts (3-4%) in a clay altered to silicified groundmass. Weathered surfaces are distinctively light red to pink, and fresh surfaces are red to white. It often

contains small vesicles up to 7 mm in length. It is altered everywhere, and feldspars have commonly been replaced by clay minerals. (Fig. 11)

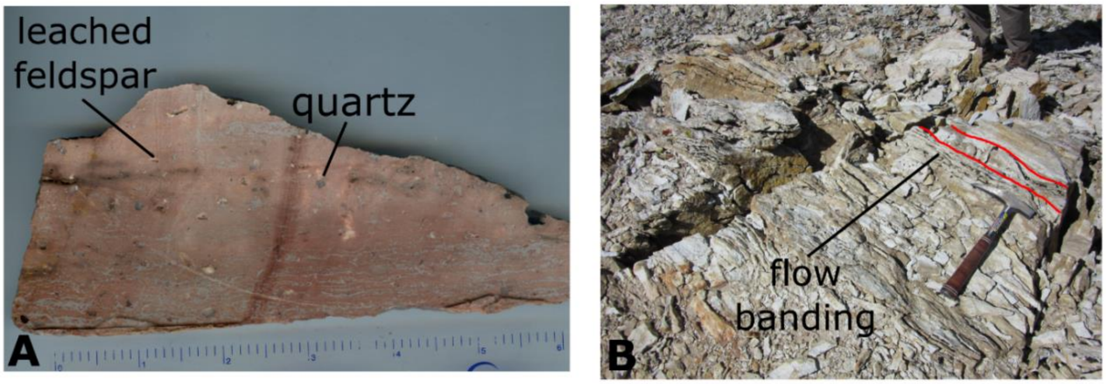

Figure 11. Unit Tra, a flow banded fissile rhyolite with quartz and feldspar phenocrysts that is argillized and/or silicified throughout the district. A.) Hand sample of Tra, which is flow banded and contains quartz phenocrysts and leached feldspar sites. Scale is inches. B.) Outcrop of Tra on Mt. Patterson showing fracturing along flow bands.

- Trc is a porphyritic flow-banded rhyolite which contains 2-6 mm sanidine phenocrysts (5%) and 1-2 mm plagioclase (3%) and quartz phenocrysts (1%). The groundmass is green to pink and glassy. This unit commonly contains abundant spherulites up to 4 cm in diameter. (Fig. 12)
- Trt is a rhyolite tuff-breccia associated with block and ash flows of unit Tra. This unit is widespread and consists of clasts of flow banded rhyolite (Tra) and pumice in matrix of ash. Lithic fragments are subangular and are usually between 1 cm and 4 cm wide, but can be as wide as a meter. This rock is orange-tan to grey and has a pocked appearance from the weathering of clasts. (Fig. 13).

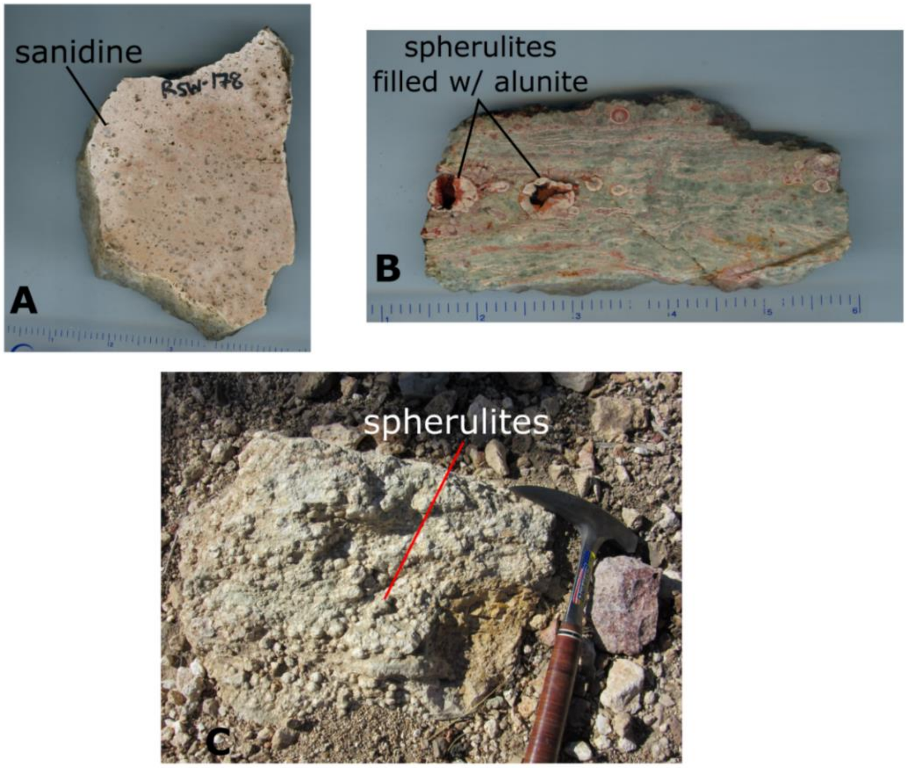

Figure 12. Unit Trc, a porphyritic rhyolite with sanidine phenocrysts (5%) and lesser quartz and feldspar that often contains spherulites. A.) Hand sample of Trc flow, showing large sanidine crystals. B.) Hand sample of green glassy rhyolite dike that is associated with Trc. Scale of A and B is inches. C.) Spherulitic Trc outcrop.

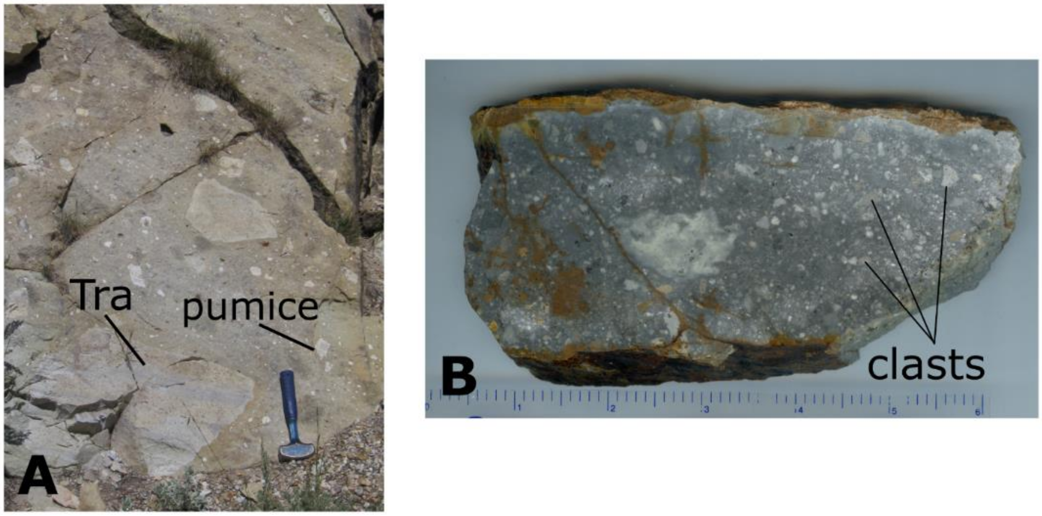

Figure 13. Unit Trt, a rhyolite tuff-breccia that is associated with rhyolite Tra. Clasts of Tra and pumice occur in a matrix of ash A.) Exposure of Trt containing large clasts of Tra and pumice. Clasts are typically less than 8 inches in width. B.) Silicified, pyrite rich hand sample of Trt. Scale is inches.

- Tbx1 is a debris flow which consists of flow-banded blocks of porphyritic flow-banded rhyolite (Trc) up to 1 m in width that are cemented by a matrix altered to quartz, alunite, and kaolinite. It commonly contains vugs up to 4 cm in width that are partially in-filled by euhedral crystals of alunite. This unit weathers to 10-20 m high knobs because of its extreme resistance to erosion. (Fig. 14)

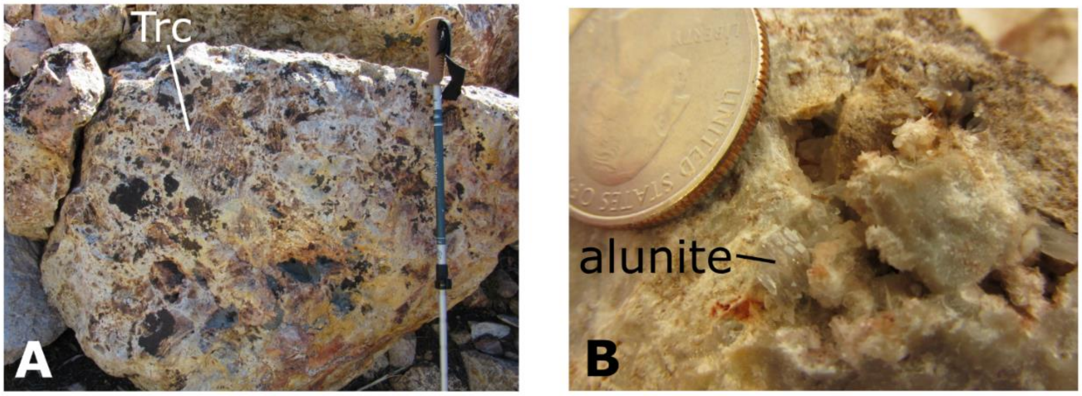

Figure 14. Unit Tbx1, a debris flow of blocks of rhyolite Trc that are cemented by quartz, alunite, and kaolinite. A.) Tbx1 contains only clasts of Trc and weathers into rounded boulders. B.) Euhedral alunite occurs in some vugs in Tbx1.

- Tri is an intrusive rhyolite which contains 2-5 mm sanidine and plagioclase phenocrysts (10-15%) in a greenish-white to white fine-grained groundmass. It occurs in small, steep sided plugs intruding porphyritic trachydacite (Td) south of Sweetwater Canyon.
- Tre is a porphyritic grey rhyolite which contains 1-2 mm hornblende (2%) and biotite (2%), and 2-3 mm plagioclase (1%) and quartz (3%) phenocrysts. The groundmass is light grey and fine-grained. This unit forms in a resistant outcrop with well-developed vertical jointing, at the head of Ferris Canyon. It is younger than units Tra and Trt, but age relationships with other units are unknown.

- Tfa is a tuff which consists of two members which inter-finger locally. A. The first member is a relatively homogenous greenish-white to white tuff containing sparse clasts of finely laminated, glassy dacite, which are partly stratified. It locally contains white lithic fragments up to 40 cm in width and sparse, angular, glassy and laminated clasts of dacite. The matrix is silt-to-sand sized white ash. B.) The second member is a layered lapilli tuff consisting of ash, sand, and small lithic fragments. It locally contains small lenses of sandstone and gravel show normal grading. Layers are either grey-white or reddish-pink. Local cross-bedding occurs in sand-rich layers.
- Tb is a vesicular basaltic andesite that occurs as a single small plug on the south side of Sweetwater Canyon. It is brown-red and largely aphanitic, with <1 mm plagioclase and quartz phenocrysts (2%). It shows characteristic iron oxide staining and auto-brecciation with clasts up to 1 m. No mafic phenocrysts are present.

Southern half of the map:

- Tac is a porphyritic hornblende trachyandesite which is composed of a dark gray-green groundmass and 10% hornblende phenocrysts up to 7 mm long that form a trachytic texture. It contains <2 mm quartz and corroded feldspar phenocrysts (≤5%), and 1-2 mm biotite phenocrysts (<2%). It often exhibits platy fracturing. It correlates with trachyandesite of Masonic (John et al., 2012) based on modal assemblage, texture, and age (Table 1; Fig. 15)

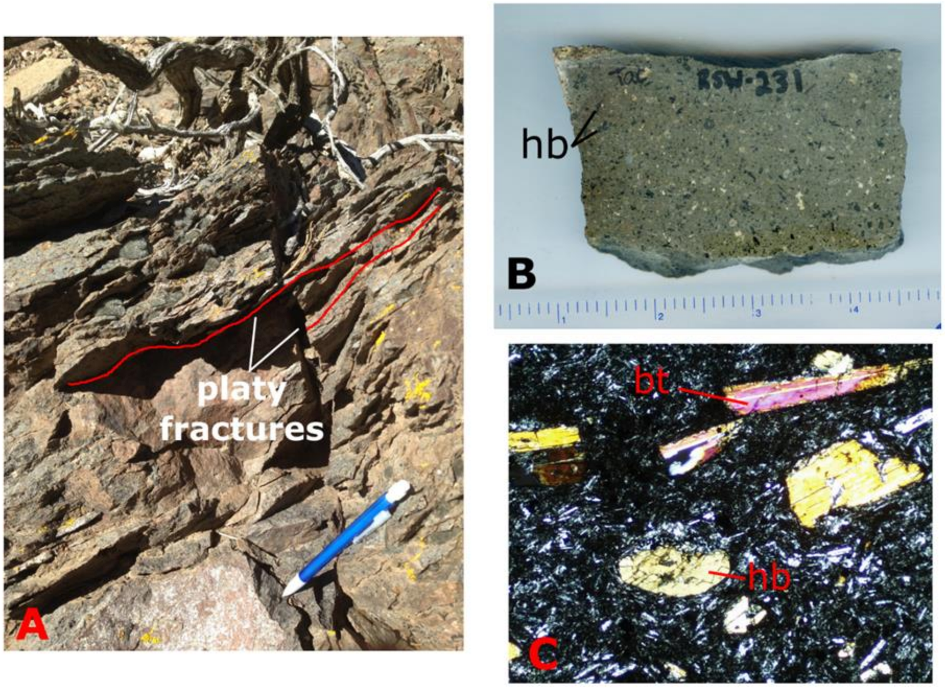

Figure 15. Unit Tac, which is a hornblende andesite interpreted to be a flow of trachyandesite of Masonic (John et al. 2012). A.) Platy fracturing in Tac. B.) Hand sample of Tac, showing unaltered hornblende (hb) phenocrysts which were dated by the $^{40}Ar/^{39}Ar$ method. Scale is inches. C.) Thin section photomicrograph in cross polarized light showing hornblende (hb) and biotite (bt) phenocrysts in a groundmass of plagioclase. Magnification is 4x.

- Td1 is a dark purple dacite which consists of <2mm biotite (3%) and feldspar (2%), and locally hornblende (2-5%) phenocrysts, in a glassy purple groundmass with poorly developed flow banding. Auto-brecciation and pumice clasts occur locally. It is older than fissile flow-banded rhyolite (Tra), rhyolite-tuff breccia (Trt), and younger than porphyritic andesites (Tab), but its age relationship to other units is unknown. (Fig. 16)

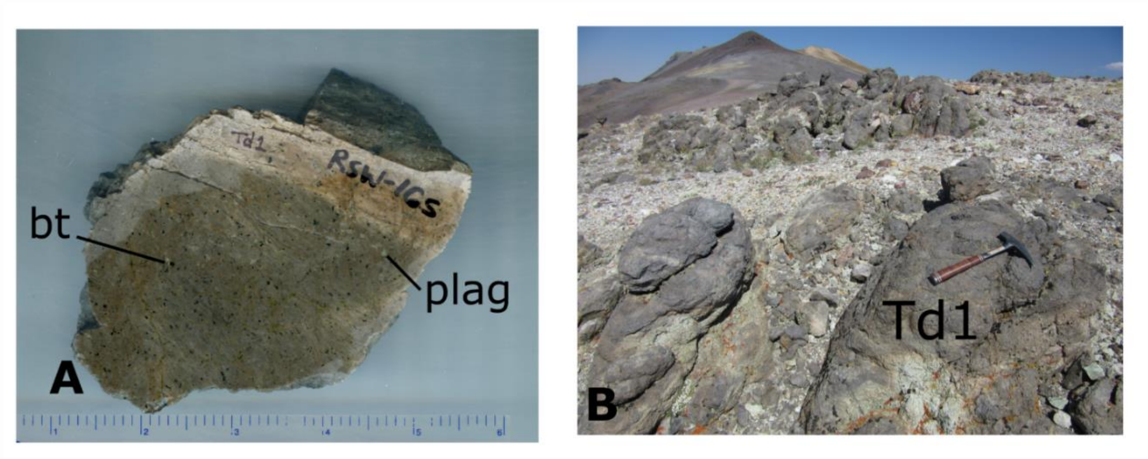

Figure 16. Unit Td1, a dark purple dacite that consists of <2mm biotite (3%), feldspar (2%) and local hornblende (2-5%) phenocrysts in a glassy purple groundmass. A.) Hand sample of Td1, which contains very small phenocrysts of plagioclase (plag) and biotite (bt). Scale is inches. B.) Exposure of Td1 as rounded outcrop near Wheeler Peak.

- Trg is a flow-banded rhyolite which contains 1-5% of 1-2 mm quartz and feldspar crystals and <1% biotite. It typically has a light purple glassy groundmass with locally abundant spherulites. This unit is found on the periphery of the Patterson mining district and is unaltered. (Fig. 17)

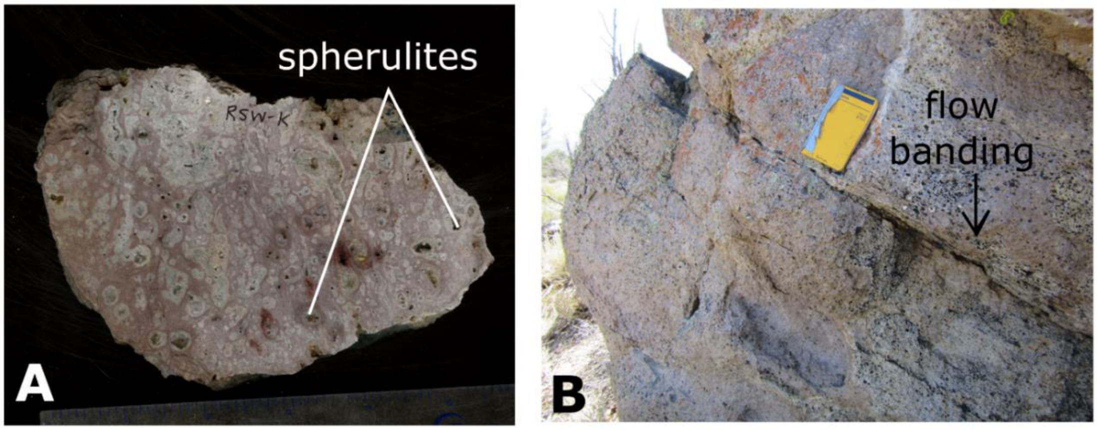

Figure 17. Unit Trg, a flow-banded rhyolite with 1-5% quartz and feldspar phenocrysts and <1% biotite in a purple glassy groundmass with locally abundant spherulites. A.) Hand sample of glassy, spherulitic Trg. Scale is inches. B.) Trg dome that exhibits steep flow banding.

- Td3 is an extremely silicified to clay altered, purple flow-banded trachydacite which consists of <2 mm quartz (2%) and 2-5 mm sanidine (3%) and 3-4 mm biotite and hornblende (4-5%) phenocrysts in a quartz and feldspar rich groundmass. It can be highly auto-brecciated.
- Tbx2 is a clast-supported volcaniclastic breccia which consists of 0.3-3 m wide blocks of altered dacite (Td3). It locally contains beds of base surge composed of laminated ash beds and beds of <5 cm wide angular clasts. This unit forms terraces at uniform elevations at the head of Fryingpan Canyon.
- Trb is a fine-grained reddish-purple rhyolite which consists of 0.5-2 mm biotite phenocrysts (3-5%), 1-3 mm plagioclase (1-2%), 2-7 mm sanidine (2-5%), and sparse 1-2 mm hornblende (<1%) phenocrysts. It shows some weak flow banding in the purple glassy groundmass.
- Tbx3 is a clast-rich tuff breccia composed of <1 cm-1.5 m wide clasts of various rhyolites and pumice, with most clasts being larger than 4 cm. It contains <30 cm thick beds of distinctive black, thinly bedded crystal tuff. It may also contain pockets of layered silica sediments that resulted from chemical precipitation in voids. These pockets of silica sediments often display syn-sedimentary folding and microfaults.
- Tbx4 represents hydrothermal matrix breccias with small to medium, subangular to subrounded clasts of quartz and country rock cemented by a matrix of quartz and iron oxides ± pyrite. Hydrothermal matrix breccias may be of various ages.
- Ts is sinter deposits, which are layered chemical sediments that formed by precipitation of silica minerals from hydrothermal fluids that flowed onto the

> surface. They mark a paleosurface and the location of hot springs. Sinter consists of fine layers of chalcedony and opal and is stained with iron oxides locally.

In addition to rhyolite porphyry (Trp) dike(s), two other families of dikes occur in the mapped area. Green, glassy, rhyolitic dikes are represented by subcrop north of Silverado Canyon (Fig. 10B). These rhyolitic dikes have in some cases been partially altered to alunite and kaolinite, and generally trend north-south. They are thought to be related to porphyritic flow-banded rhyolite (Trc) because of a close spatial relationship. Resistant, fine-grained, more mafic dikes south of Silverado Canyon appear to have been conduits for andesite flows in the southern part of the district and cross-cut both quartz monzonite and metasedimentary rocks of the roof pendent.

v. Structure

Few faults were recognized on the surface during mapping for this study; however, an earlier study that examined underground workings identified numerous series of faults (Hunter, 1976). It is likely that there are additional faults in the Patterson district, but it is difficult to locate or trace faults because of a large amount of landslide, talus, and vegetation cover. Faults were important for localizing mineralizing fluids, but field relationships indicate that these faults show little displacement. Most topographic relief in the Sweetwater Mountains is not a result of down-faulting to the east, but rather reflects a combination of uplift from tilting and possibly magmatic inflation. This interpretation is supported by the lack of faults with large offset (with the exception of the range front fault) and the absence of post-Miocene sedimentary rocks.

The earliest faulting in the district is inferred from the series of semi-parallel canyons that drain the east side of the Sweetwater Mountains at the latitude of the Patterson mining district (i.e. Sweetwater Canyon, Quaking Aspen Canyon, Cottonwood Canyon, Silverado Canyon, and Ferris Canyon) and from reports of a thick, east-west trending zone of fault gouge beneath Silverado Canyon (Hunter, 1976; Fig. 18). Later faulting consists of north-south trending fault segments known as the Belfort-Silverado fault system (Hunter, 1976; Fig. 18). Faults of this system have near vertical dips, mostly to the west. This north-south trending stage of faulting was important to formation of silver-gold deposits. A third period of faulting created the fault scarp that forms the steep eastern boundary of the Sweetwater Mountains (range front fault M, Fig. 18). One suspected fault (topographic fault N, Fig. 18), which exposes quartz monzonite and is expressed topographically by alignment of contrasting slope attitudes, appears to have caused a relatively large amount of displacement (an estimated 1,000 feet, down-to-the-east) in the study area.

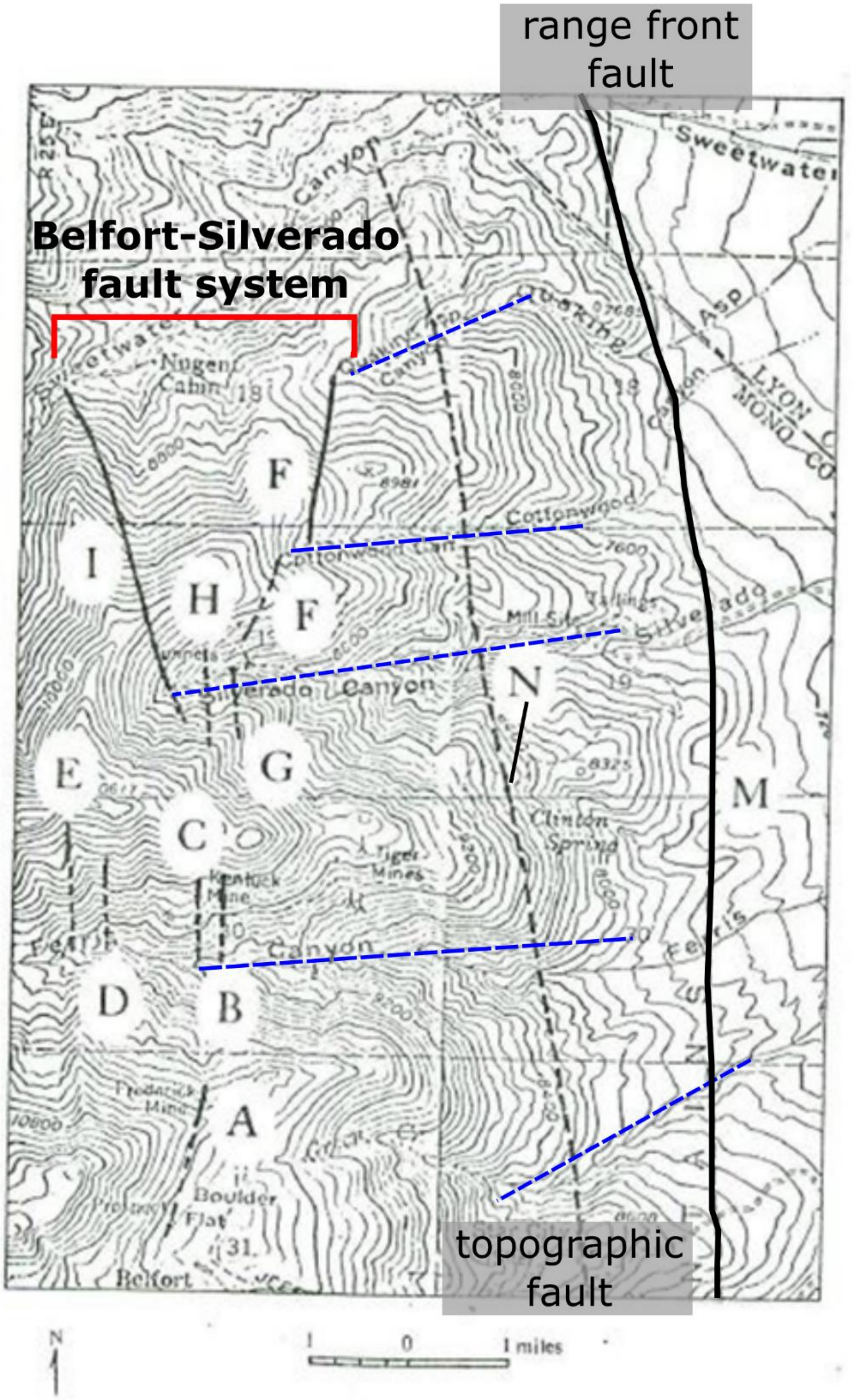

Figure 18. Series of faults in the Sweetwater Mountains, modified from Hunter, 1976. Blue dashed lines represent the earliest faults, marked by E-W semi-parallel eastward draining canyons. Black lines marked A-H are the Belfort-Silverado fault system (Hunter, 1976). Faults and veins strike 330 to 30 degrees and have near vertical dips mostly to the west, and localized mineralizing fluids. Fault N is an inferred fault from a topographic change. Fault M is the range front fault and represents the youngest stage of Basin and Range faults.

IV. Geochronology

Ages of Tertiary volcanic rocks and ages of hydrothermal alteration and silver-gold deposits in the Patterson mining district were previously unknown. In order to determine temporal relationships between volcanic rocks, silver-gold deposits, and hydrothermal alteration, minerals from seven volcanic rock units, one silver-gold deposit, and two hydrothermal alteration zones were separated for dating by the $^{40}Ar/^{39}Ar$ and U-Pb methods. Sanidine, biotite, plagioclase, hornblende, adularia, and alunite $^{40}Ar/^{39}Ar$ dates (Appendix B) were determined at the New Mexico Geochronology Research Laboratory (Socorro, NM; L. Peters, written communication, 2015), the Auburn Noble Isotope Mass Analysis Laboratory (Auburn, AL; W. Hames, written communication, 2016), and the U.S. Geological Survey (Menlo Park, CA; R. Fleck and P. Vikre, written communication, 2015, Table 1; Fig. 19). Zircon U-Pb dates (Appendix C) were determined at the U.S. Geological Survey (Denver, CO; C. Holm-Denoma, written communication, 2016, Table 1).

Based on a hornblende date, hornblende andesite (Tac; correlative with trachyandesite of Masonic, John et al., 2015) exposed in Fryingpan Canyon at relatively low elevations (<8000 feet) is 13.6 Ma and is the oldest Tertiary rock. It is likely associated with the Masonic volcanic center in the Bodie Hills, which are adjacent to the Sweetwater Mountains to the southeast (Fig. 1), based on its modal composition, location, elevation, and date. Rhyolite and dacite units (Td, Td1, Trc, Trg, Trp) of the Sweetwater volcanic field are ~6.6-5.3 Ma (zircon, biotite, plagioclase, and sanidine dates; Table 1; Fig. 19; 20), with dates of igneous minerals in dacite units older than those of rhyolite units. Dates of sanidine in rhyolite unit Trc range from ~5.7-5.3 Ma and show Ar loss, which may reflect proximity to rocks altered to quartz and alunite. A relatively young rhyolite dome in Sweetwater Flat (~5.3 Ma; sanidine) known as Round Mountain (Fig. 2), occurs ~3 km east of the Sweetwater; similar rhyolite has not been identified in the Patterson district.

Sample No.	Latitude	Longitude	Elevation (ft)	Description	Method	Mineral	Date (Ma)	Error (Ma)	Analyst
				Igneous Minerals					
RSW-260	38.449015	-119.250435	8343	Medium-grained quartz monzonite with purple orthoclase crystals collected from roadcut on the road to the Silverado mine. Unit Jqm.	U-Pb	Zircon	166.26	±0.89	C. Holm-Denoma
RSW-CB011a	38.409043	-119.229750	7488	Hornblende andesite flow with light grey matrix in Fryingpan Canyon. Unit Tac.	Ar/Ar	Hornblende	13.620	±0.02	L. Peters
RSW-165	38.415424	-119.294528	11365	Purple glassy rhyolite plug with biotite phenos west of Wheeler Peak. Unit Td1.	Ar/Ar	Plagioclase	6.56	±0.22	W. Hames
						Biotite	6.576	±0.17	W. Hames
RSW-056	38.473504	-119.253363	8302	Grey porphyritic dacite flow with sanidine, plagioclase, and biotite phenocrysts south of Sweetwater Canyon. Unit Td.	Ar/Ar	Sanidine	5.977	±0.027	W. Hames
						Plagioclase	5.980	±0.050	W. Hames
						Biotite	6.116	±0.109	W. Hames
RSW-261	38.446797	-119.266843	9248	Rhyolite porphyry dike with megacrystic sanidine in a green matrix from outcrop at the Silverado mine. Unit Trp.	U-Pb	Zircon	5.89	±0.14	C. Holm-Denoma
RSW-177	38.461215	-119.238690	7362	Pink flow banded rhyolite flow with sanidine phenocrysts north of Cottonwood Canyon. Unit Trc.	Ar/Ar	Sanidine	5.66-5.38	±0.26	W. Hames
RSW-JM004	38.517233	-119.226949	7287	Flow banded, strongly spherulitic rhyolite dome with sanidine phenocrysts in Sweetwater Flat. Unit Trg.	Ar/Ar	Sanidine	5.549	±0.005	L. Peters
RSW-CB002b	38.497422	-119.214391	6898	Grey rhyolite dome with sanidine and plagioclase phenocrysts in Sweetwater Flat. Undifferentiated rhyolite.	Ar/Ar	Sanidine	5.250	±0.005	L. Peters
				Hydrothermal Minerals					
SIL08-P1	38.452020	-119.238300	7679	Silicified breccia of clasts of rhyolite above the mill on the Silverado road, with alunite crystals in vugs. Unit Tbx1.	Ar/Ar	Alunite	5.619	±0.375	R. Fleck
SLUD08-11A	38.436860	-119.293520	11156	Rhyolite plug below Mt. Patterson altered to fine-grained alunite. Unit Tra.	Ar/Ar	Alunite	5.611	±0.034	R. Fleck
RSW-199	38.447910	-119.263841	9358	Adularia vein in mineralized rhyolite breccia from a dump at the Silverado mine. Unit Trt.	Ar/Ar	Adularia	5.127	±0.012	W. Hames

Table 1. U-Pb and ^{40}Ar/^{39}Ar dates (Ma) of igneous and hydrothermal minerals in the Sweetwater Mountains (W. Hames, written communication 2016; R. Fleck and P. Vikre, written communication 2016; C. Holm-Denoma, written communication 2016; L. Peters, written communication 2015). Locations of dated minerals are shown on Plate I.

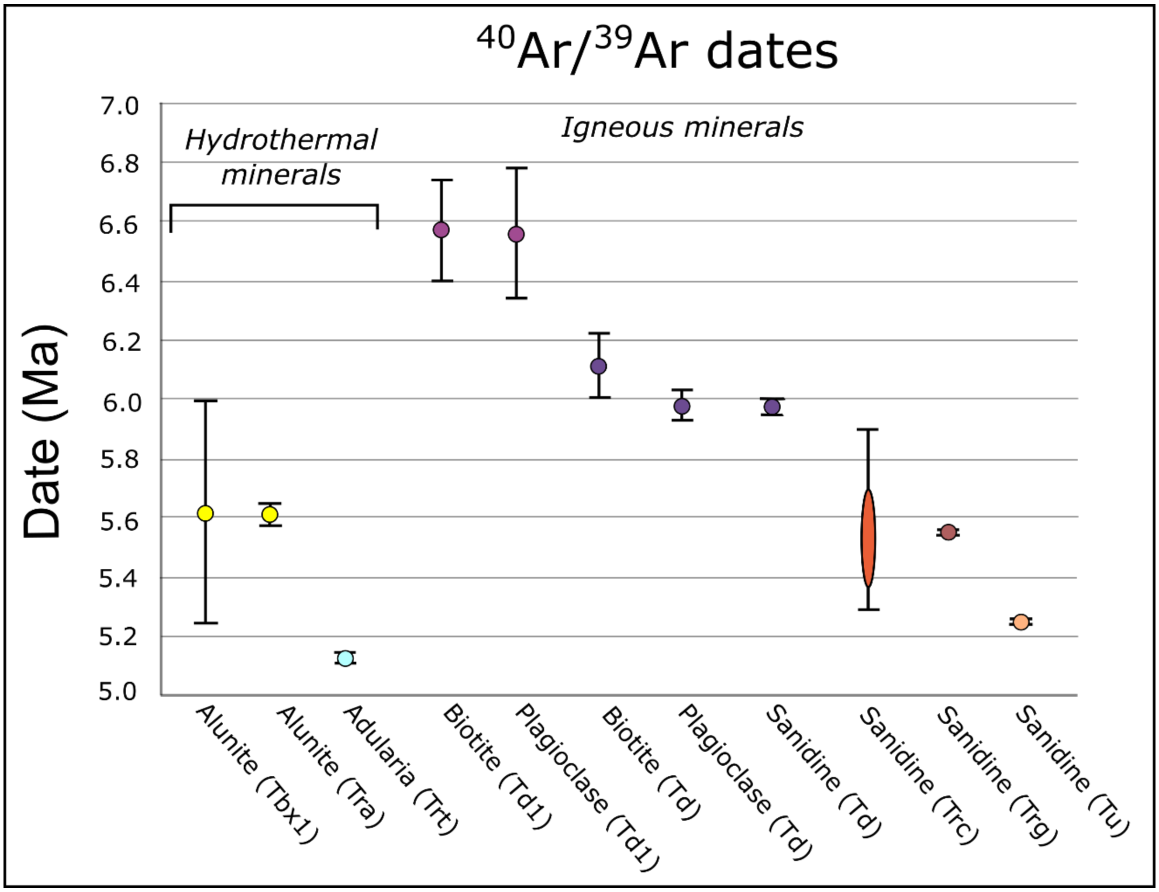

Figure 19. ^{40}Ar/^{39}Ar dates (Ma) of igneous and hydrothermal minerals in the Sweetwater Mountains. Circles are plateau or isochron dates, and vertical bars represent 2 sigma errors. The oval symbol of sanidine separated from rhyolite Trc represents a range of sanidine dates, likely because of Ar loss at or subsequent to ~5.6 Ma.

Rhyolites and breccias in alteration zones were altered to quartz, alunite, and other minerals at ~5.6 Ma, based on alunite dates. One dated alunite sample occurs in rhyolite breccia (Tbx1) at 7679 ft, and the other occurs in flow banded rhyolite (Tra) at 11,156 ft, and <1,000 feet of displacement of the altered units by faulting has been recognized. The quartz-alunite alteration event corresponds to the age of sanidine dated from unit Trc, rhyolite exposed north of Cottonwood Canyon. The occurrence of relatively coarse-grained alunite in leached voids in silicified rhyolite breccia near the

Silverado mill site, absence of sulfide minerals, and alunite sulfur isotope values (P. Vikre, written communication, 2015), support a steam-heated origin for the alunite (Rye, 2005). Adularia in silver-gold veins at the Silverado mine is ~5.1 Ma, indicating some or possibly all precious metal deposits are related to unexposed igneous rocks younger than those dated.

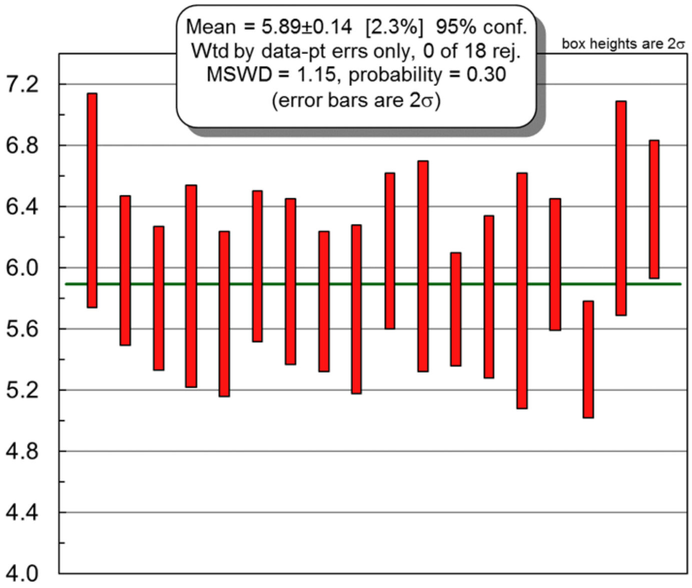

Figure 20. U-Pb dates (Ma) of zircons in sample RSWCB-261 (rhyolite porphyry dike, Trp). The red boxes include 2σ errors and the green line represents the average date of 5.89 ± 0.14 Ma.

Pre-Tertiary rocks in the Sweetwater Mountains have been assigned Mesozoic ages based on similarity and proximity to plutons of the Sierra Nevada batholith, and from K-Ar dating of biotite and hornblende (Schweikert, 1976; Brem 1984). Plutons in the Sweetwater Mountains, including Granite of Devil's Gate-Mack Canyon, Granite of Desert Creek, and Granite of Swauger Creek, are ~94-81 Ma. Quartz monzonite collected in the Patterson district (unit Jqm; Fig. geomap; unit Kef of Brem, 1984) has a U-Pb zircon age of ~166 Ma (Table 1; Fig. 21). This age is similar to the ages of many Jurassic plutons of the Sierra Nevada Batholith (Fig. 22).

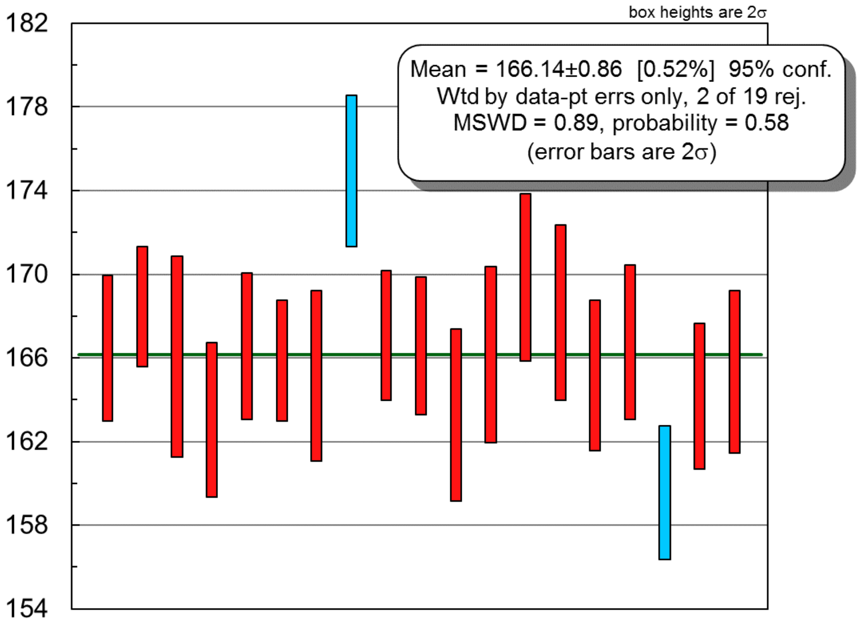

Figure 21. U-Pb dates (Ma) of zircons in sample RSWCB-261 (quartz monzonite, Jqm). The red boxes include zircon dates and 2σ error that were used to calculate an average age, and the blue boxes include zircon dates and 2σ error that were rejected when calculating the average age. The green line represents the average zircon age, 166.14 ± 0.86 Ma.

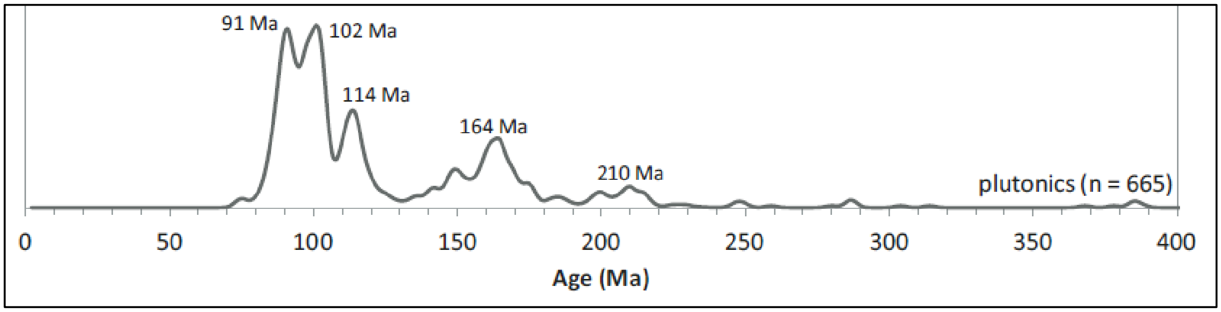

Figure 22. Age frequency (Ma) of 665 plutonic samples of the Sierra Nevada batholith. From (Paterson et al., 2014).

V. Miocene Hydrothermal Mineral Assemblages

i. Epithermal silver-gold deposits

The precious metal deposits of the Patterson mining district are epithermal deposits, which are defined as shallow depth (<1.5 km), low temperature (<300° C) deposits which form in zones of high permeability within hydrothermal systems (Simmons et al., 2005). Specifically, the deposits of the Patterson district contain quartz ± calcite ± adularia ± illite as gangue minerals, and are similar to low-sulfidation epithermal deposits (Simmons et al., 2005). Low-sulfidation epithermal deposits contain Au-Ag, Ag-Au, or Ag-Pb-Zn metallic and other hydrothermal minerals which precipitate due to boiling and fluid mixing and form veins, stockwork veins, or disseminations in altered wall rocks. A direct association with input from magmatic fluids is often unclear in these deposits and they are thought to form at significant distances from magmatic heat sources (Hedenquist and Lowenstern, 1994).

Silver-gold deposits in the Patterson mining district consist of quartz ± calcite + illite ± adularia, electrum, acanthite, chlorargyrite, base metal sulfides, and silver telluride. Vein textures include layered colloform-crustiform quartz, bladed calcite, and quartz pseudomorphs of bladed calcite (Simmons et al., 2005). Deposits occur in as veins, stockwork, or disseminated in wall rocks in three sub-parallel north-trending belts with distinct characteristics. These belts have historically been called the Cameron belt (gold-rich), Clinton belt (silver-rich), and California Comstock belt (contains both gold and silver; Irelan and Whiting, 1888, Table 1, Plate II). Differences in deposit mineralogy, textures, silver: gold, and geochemistry are not likely a result of variable timing of hydrothermal activity, but rather because of varying depths of exposure, based on the presence of sinter terraces, alteration mineral assemblages, and textural indicators for boiling. The mineral belts occur within north- to northeast-trending zones of rocks altered by hydrothermal fluids (Plate II).

ii. Hydrothermal alteration zones

Hydrothermal alteration in the Sweetwater Mountains affected an area of ~200 km^2. Alteration zones are constrained by E-W trending faults in Sheep Creek Canyon to the north and Fryingpan Canyon to the south (Fig. 18), and by the N-S trending range front fault on the east slope of the range (Fig. 23). West of the crest of the Sweetwater Mountains, alteration zones appear to end east of Lobdell Lake, based on satellite photographs (Fig. 23). The N-S linearity of altered rocks west of the crest of the range may also be indicative of a fault; however more abundant vegetation on the western slope of the Sweetwater Mountains may obscure altered rocks west of Lobdell Lake.

Alteration mineral assemblages determined by field observations, SWIR spectra analysis, and ASTER satellite imagery (Plate II) include:

- Quartz/chalcedony + minor illite ± calcite ± adularia: This mineral assemblage occurs in silver-gold mineral deposits throughout the district. Chalcedony is abundant relative to illite. Calcite, where present, is coarse grained and bladed or disseminated in the matrix. Adularia is medium- to fine-grained and has massive habit in the matrix or coats fracture surfaces as euhedral crystals.
- Quartz + alunite ± kaolinite: This mineral assemblage represents steam-heated hydrothermal alteration above the water table, based on relatively coarse-grained alunite in leached voids in silicified rhyolite breccia near the Silverado mill site, absence of sulfide minerals, and alunite sulfur isotope values (P. Vikre, written

communication, 2015). Alunite is fine-grained and replaces phenocrysts and matrices, or occurs as coarse-grained, euhedral crystals in voids of leached phenocrysts or rock fragments. Kaolinite is a minor local component and occurs as very fine-grained clay in the matrix.

- Illite ± quartz: Illite is the most widespread alteration mineral in the Patterson district. Illite alteration of both phenocrysts and matrices occurs mostly in fissile flow-banded rhyolite (Tra), rhyolite tuff-breccia (Trt), and porphyritic flow-banded rhyolite (Trc), which were relatively permeable. Rocks altered to illite ± quartz occur adjacent to mineral deposits and in rhyolite above mineral deposits in the Clinton belt.
- Illite + montmorillonite ± quartz: This assemblage consists of illite and montmorillonite with local quartz. Montmorillonite and illite are fine-grained and occur in the matrix and replacing phenocrysts. Montmorillonite abundance generally increases with distance from mineral deposits.
- Kaolinite ± quartz ± opal ± dickite: This mineral assemblage is dominated by kaolinite, and contains thin veins of cockscomb quartz and local dickite. Kaolinite mostly replaces phenocrysts but can occur in the matrix in minor amounts. Opal occurs in two localities, at the Silverado mill and at Star City.
- Montmorillonite: Large areas of montmorillonite-dominant altered rocks occur distally to silver-gold mineral deposits. Small volumes of montmorillonite-altered rocks also occur near mineral deposits. As mineral deposits are approached, distal montmorillonite-dominant altered rocks transition to illite + montmorillonite altered rocks.

- Quartz + sericite + pyrite: This mineral assemblage typically occurs in altered quartz monzonite. Quartz and sericite are medium-grained and replace the matrix. Quartz is anhedral and sericite occurs as elongated laths. Pyrite is coarse grained, it occurs in the deepest exposures of quartz monzonite in Silverado Canyon, and it could possibly be related to molybdenum mineralization of likely Mesozoic age.

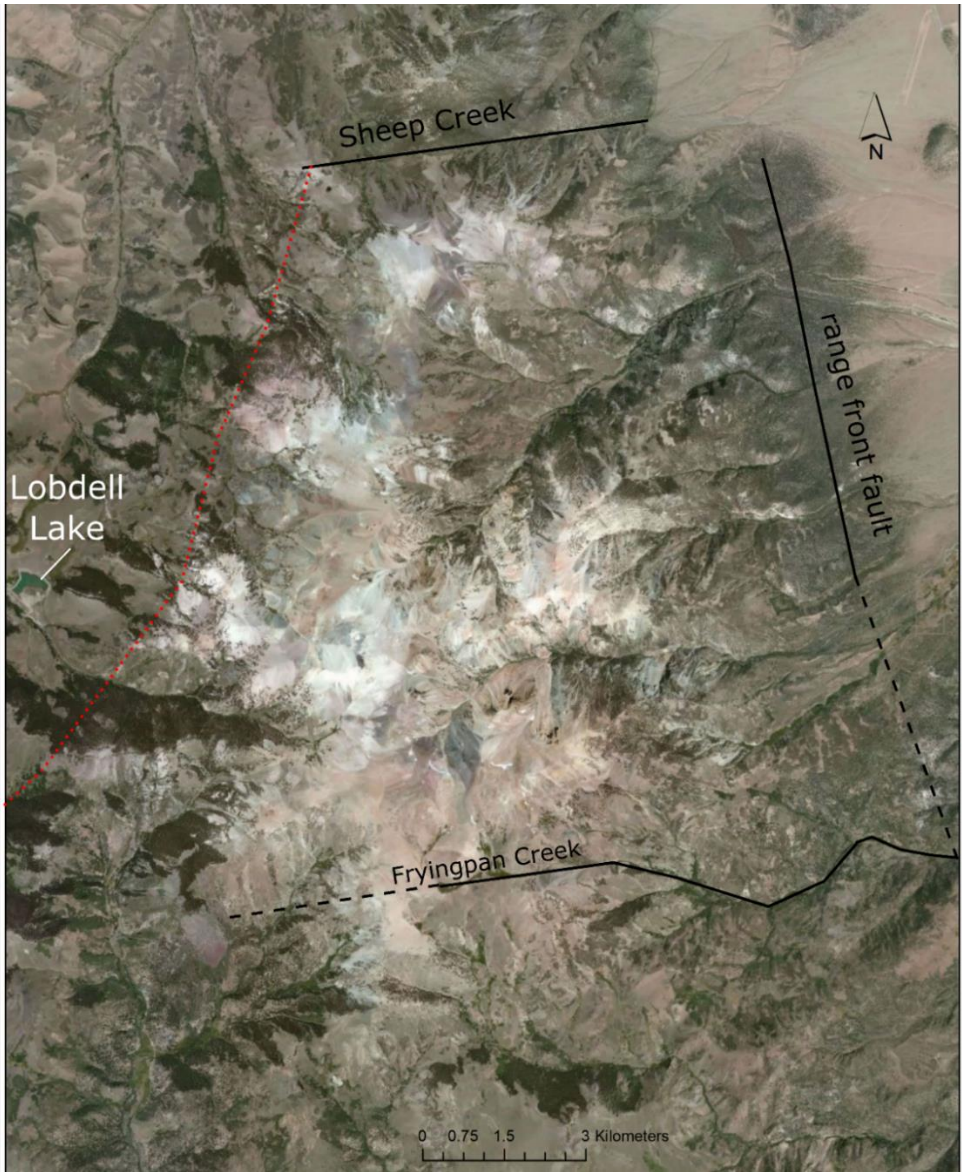

Figure 23. Satellite photograph of the Sweetwater Mountains showing faults and inferred faults that truncate hydrothermally altered rocks between through Sheep Creek and Fryingpan Creek canyons and along the range front fault to the east. Hydrothermally altered rocks appear to be truncated by an inferred fault to the west that is marked with a red dotted line.

- Propylitically altered rocks were not mapped in detail but are represented by the assemblage of albite + epidote ± chlorite in quartz monzonite and calcite + chlorite ± pyrite in andesites.

A combination of high-angle faults, stratigraphy, and permeability and modal compositions of igneous rocks appear to control alteration assemblages. High angle faults created fluid pathways through which hydrothermal fluids ascended. The alteration map (Plate II) reflects hydrothermal fluid flow in three north-to-northeast trending zones which are interpreted to be high angle faults, fault zones, or groups of faults. These fault zones correspond to the three mineral belts (Cameron, Clinton, and Comstock). High permeability of fissile flow-banded rhyolite (unit Tra) likely caused pervasive alteration of the entire unit, resulting in some east-west-trending distribution of hydrothermal minerals in rhyolites. Intense alteration is of volcanic rocks to quartz, alunite, and kaolinite occurs at the Clinton town site and near the Silverado mill. Steam-heated alteration consisting of quartz, alunite, and kaolinite overprints illite ± montmorillonite alteration adjacent to silver-gold deposits at Star City and Mt. Patterson.

Intensity of rock alteration correlates with permeability and buffering capacity of rocks. Andesites are unaltered, altered to calcite + chlorite, or have cloudy feldspars indicative of weak alteration to illite or montmorillonite. Quartz monzonite is typically propyliticly altered to epidote + albite ± chlorite, or altered to quartz-sericite-pyrite near faults or fractures. In Sweetwater Canyon and near the Frederick mine it is altered to illite + montmorillonite or montmorillonite. In contrast, rhyolite units have a low capacity to buffer hydrothermal fluids and are more pervasively altered by hydrothermal fluids, which obscures the north-trending mineral belts in the alteration map (Plate II).

Wavelengths of the 2200 nm reflectance feature in spectra of illite were determined in order to identify possible upflow zones of hydrothermal fluids. Spectra of illite and the position of the 2200 nm reflectance feature were obtained using an ASD Terraspec reflectance spectrometer. The 2200 nm reflectance feature in illite corresponds to the Al-OH bond and shifts in wavelength from ~2190 to ~2216 nm indicate increases in Fe and/or Mg content or decreases in Al content (Yang et al., 2001). Lower wavelength absorption features (~2190-2200 nm) correspond to an increase in Al content, which is the result of higher temperatures (Yang et al., 2001). A decrease in wavelength of the Al-OH bond is thought to indicate proximity to fluid upflow zones (Yang et al., 2001). An image showing wavelength of the Al-OH bond wavelengths of illite spectra was produced for the Patterson district (Fig. 24). Wavelengths were separated into quartiles between 2195 nm and 2215 nm. Progressively lower wavelengths are effective in defining gradients toward veins in the California Comstock belt and at Belfort. Only high illite Al-OH bond wavelengths occur in illite-altered rocks near the Silverado mine. This illustrates that high Al-OH bond wavelengths are not always observed in close lateral proximity to mineral deposits. However, low wavelengths occur in altered rhyolite at higher elevations above deposits. Low wavelengths measured in rocks altered to illite could indicate mineral deposits at depth in the Clinton belt. A general NE-trend of low wavelength bonds occurs in the Cameron belt, which most likely corresponds to pervasive fluid flow.

i. Cameron belt

Disseminated silver and gold deposits in the Cameron belt contain the highest gold grades in the Patterson district. Mines such as the Monte Cristo, Thoroughbrace, Star City, and “Fryingpan Canyon” produced at least 25,000 ounces of gold prior to 1915. Disseminated silver and gold occur minerals in black, pyrite-rich chalcedony in clast-rich

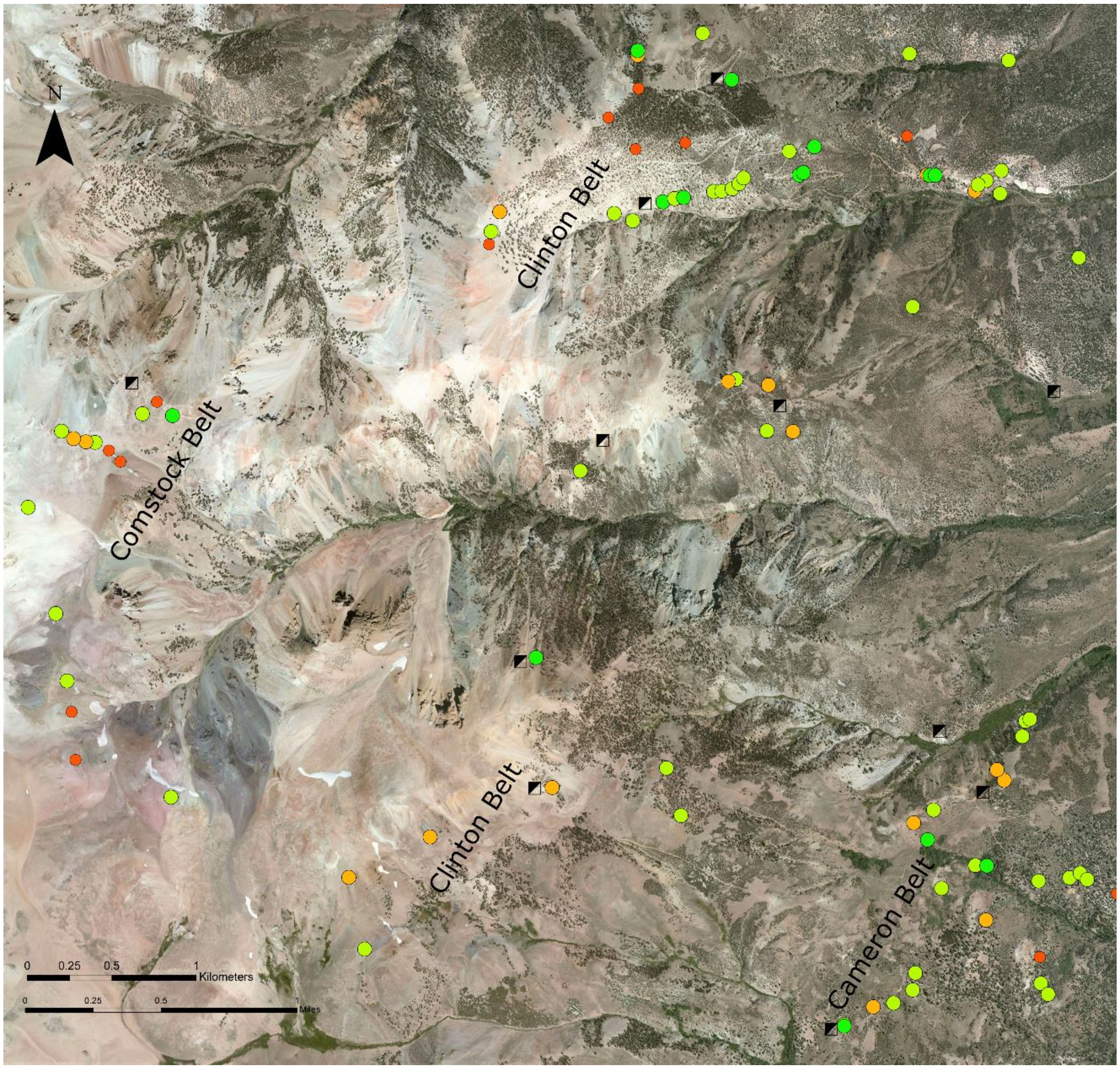

Figure 24. Map showing the position of the 2200 nm feature of illite spectra in the Patterson mining district. Red = 2195- 2201 nm, orange = 2202-2205 nm, yellow = 2206-2209 nm, green = 2210-2215 nm. Lower wavelengths of the 2200 features vector towards mineral deposits and faults.

tuff breccia (Tbx3) and in altered flow-banded trachydacite (Td3; Fig. 25). The silver to gold ratio in dump samples ranges from 1 to 275. The Cameron belt exhibits a general northeast-striking trend which likely reflects fault control.

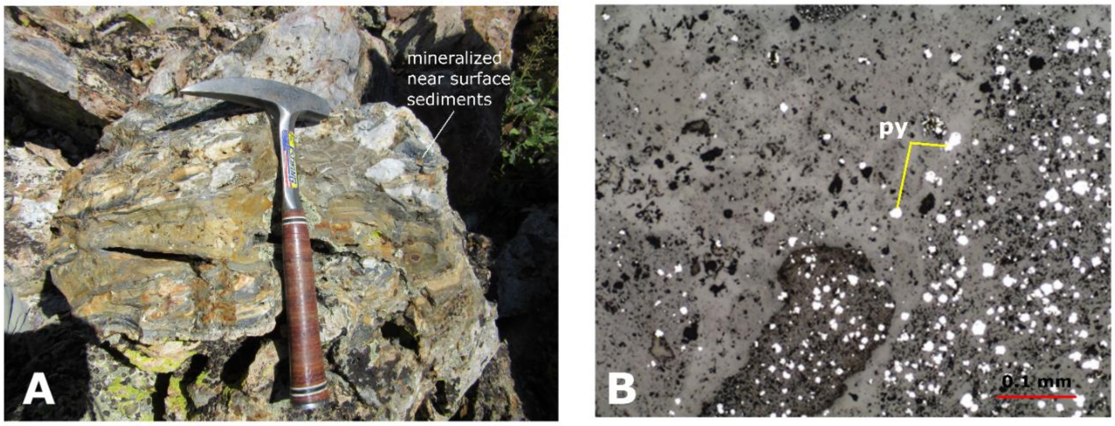

Figure 25. A. Typical appearance of gold-bearing mineralized rocks in the Cameron belt. B. Thin section photomicrograph of a mineralized rock in the Cameron belt. Disseminated pyrite occurs both in clasts and in the matrix of clast-rich tuff breccia (Tbx3).

Hypogene sulfide minerals in Cameron belt deposits are mostly pyrite, with minor acanthite, chalcopyrite, galena, molybdenite, and sphalerite. Pyrite contents vary from a few percent to ~10% of mineralized rocks. Some pyrite crystals exhibit a second stage of growth around a pre-existing euhedra, as revealed by SEM imagery (Fig. 26). Pyrite often contains micron to sub-micron scale inclusions of mostly acanthite and galena, and minor sphalerite and molybdenite (Fig. 27). Some pyrite contains up to 5 weight percent arsenic; it weathers to limonite, scorodite, and arsenolite that stain many mineralized rocks (Fig. 28). Acanthite (Ag_2S) and chalcopyrite line voids or encrust pyrite grains (Fig. 29). Acanthite can contain 4-10 wt. % Se. No gold-bearing minerals were observed in thin section, despite the higher gold grades of samples from Cameron belt deposits.

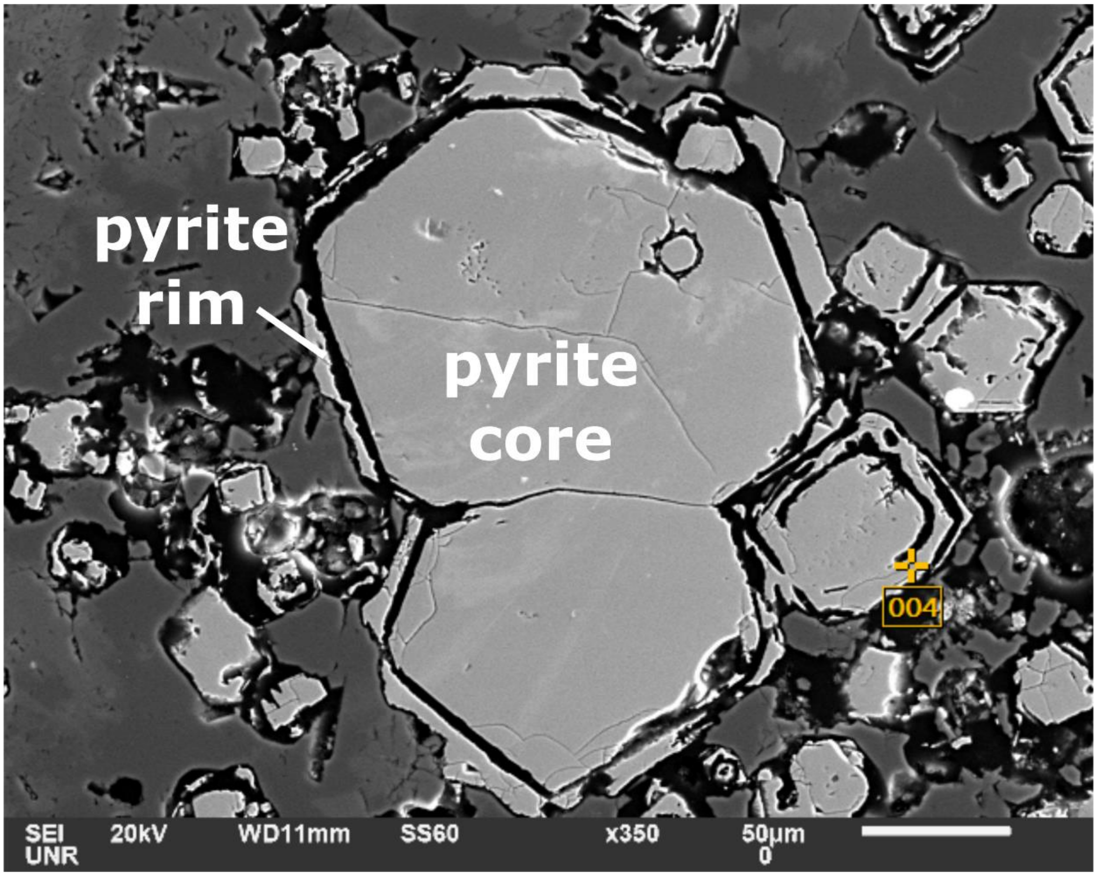

Figure 26. SEM image showing rimmed pyrite, which commonly occurs in mineralized rocks in the Cameron belt. An initial hydrothermal event deposited pyrite cores, and a subsequent hydrothermal event likely deposited pyrite rims.

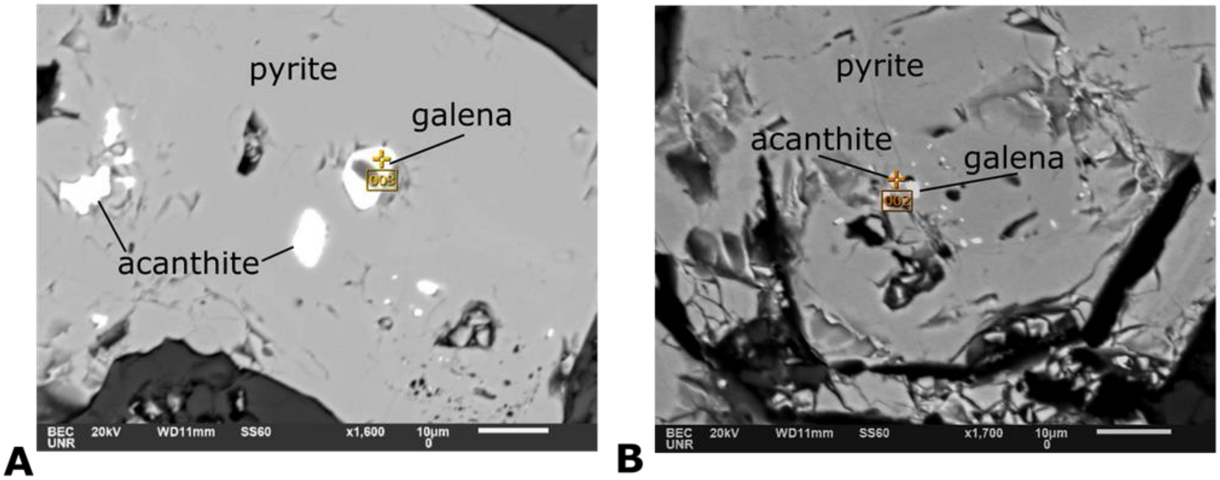

Figure 27. SEM image of acanthite and galena inclusions in pyrite in sample RSW237-2. Inclusions are typically <5 µm in width. Sphalerite and molybdenite also occur as inclusions.

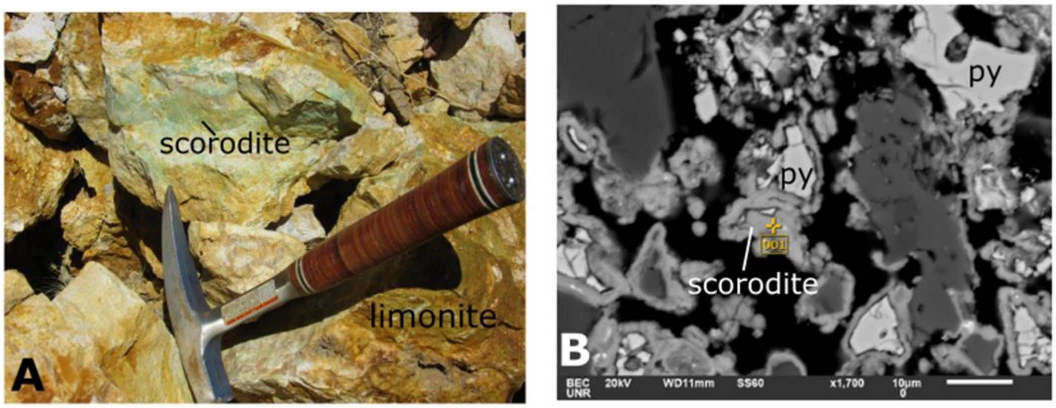

Figure 28. A.) Weathering of As-rich pyrite causes surface staining by scorodite ($Fe^{3+}(AsO_4)\bullet 2(H_2O)$) and limonite. B.) Abundant scorodite and minor arsenolite also occur with pyrite (py).

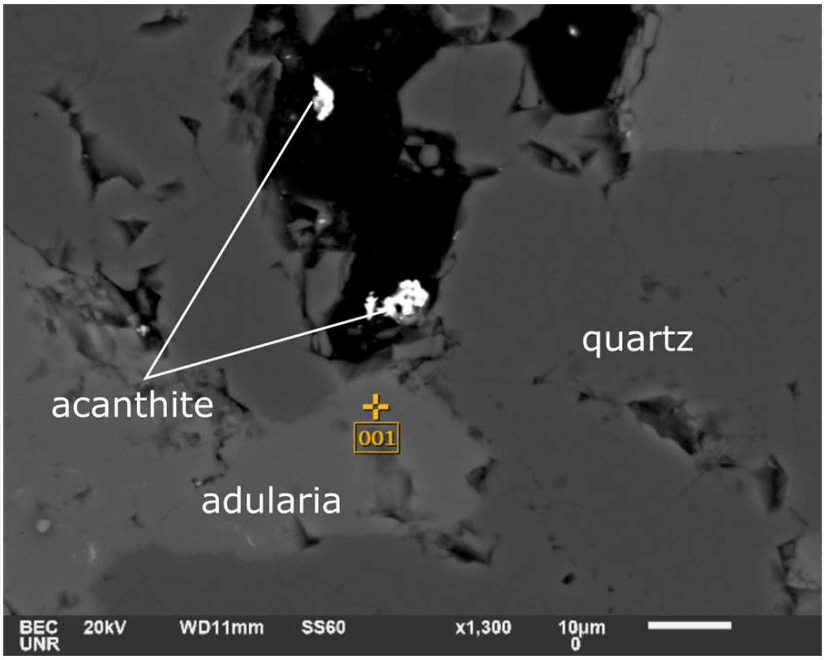

Figure 29. SEM image of acanthite with ~6 weight percent Se in a void in quartz and adularia (sample RSW237-2). Chalcopyrite and acanthite were deposited in voids and on the surface of pyrite grains. Acanthite also occurs as inclusions in pyrite.

Geochemical analyses (n=15) show that Au, Ag, As, and Sb concentrations are highly elevated in samples from the Cameron belt (Fig. 30; Appendix D). This geochemical signature is consistent with a shallow, hot spring type environment (Nelson, 1987). Gold grades range from 19 ppb -17.9 ppm, with an average of 1.8 ppm. Silver grades range from 0.3-152 ppm and average 26 ppm (Fig. 30). Arsenic concentrations are 5-776 ppm and average 256 ppm. Antimony concentrations are 5-84 ppm and Te concentrations are relatively low (<0.05-1.8 ppm). A Spearman correlation matrix for the Cameron belt (Appendix E) shows that gold has a positive correlation with Ag, Li, Mo, and V. Gold has a negative correlation with Al, K, Na, and Ti, suggesting that gold grade is correlated with removal of these elements. Silver is positively correlated with Au, Mo, and V and is negatively correlated with Ca.

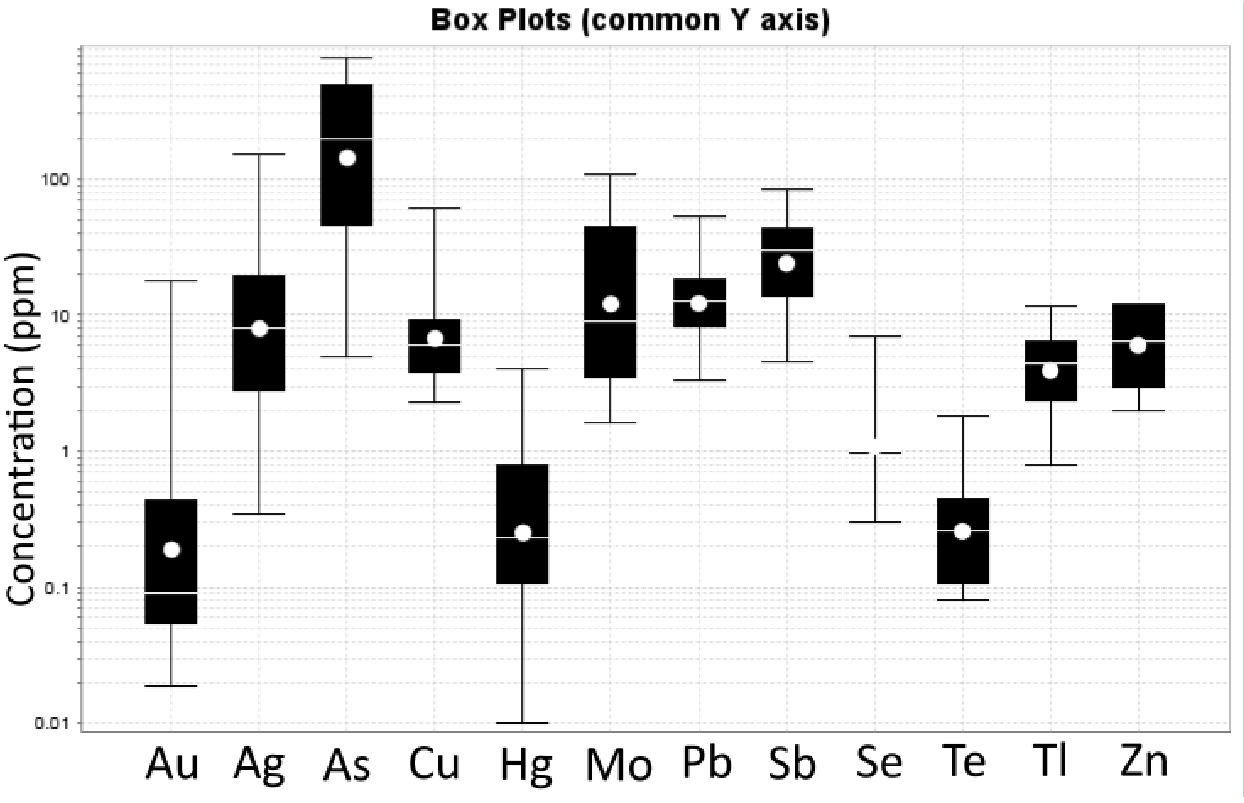

Figure 30. Box plots with a logarithmic Y axis showing concentrations of elements in mineralized samples from the Cameron belt deposits. Each box represents 50% of the concentrations of elements, from quartile 1 (the bottom 25% of the range of concentrations) at the bottom to quartile 3 (the upper 25% of the range of concentrations) at the top. The white circle within the box represents the mean value for that element. The whiskers represent 95% and 5% values. n= 16 samples.

Many lines of evidence support a near-surface origin for the deposits of the Cameron belt. Three sinter terraces, in part dismembered, occur near Star City and in upper Fryingpan Canyon (Fig. 31). There are large blocks of sinter in landslide debris north of Fryingpan Canyon, which implies that sinter terrace(s) were displaced by mass wasting or deflation. Pyrite-rich chalcedony occurs in sinter north of Fryingpan Canyon (Fig. 32). There are also chemical sediments of layered silica which show sedimentary structures and are inferred to have been deposited in near-surface pockets within clast-rich tuff-breccia (unit Tbx3). Veins of adularia and/or quartz pseudomorphs of bladed calcite measuring 1-3 cm in thickness occur <100 m in elevation below sinter terraces and support shallow boiling (Fig. 33A). A breccia in the Monte Cristo mine area consists of elongated clasts of trachydacite (Td3) and quartz within a matrix of chalcedonic quartz and pyrite, which is interpreted as a hydrothermal eruption breccia (Fig. 33B). This is

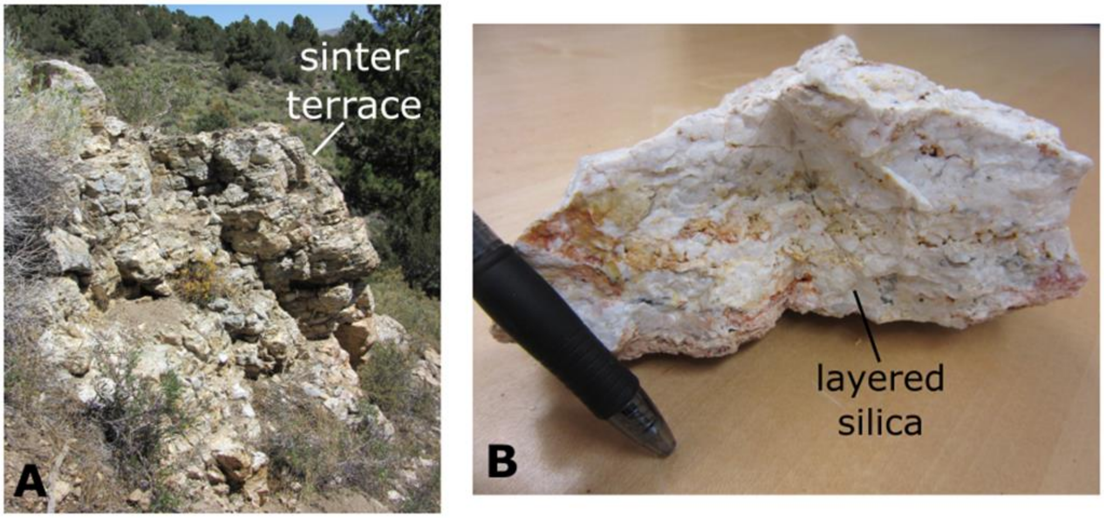

Figure 31. A.) Sinter terrace north of Fryingpan Creek which marks a paleosurface. Dip attitudes on the terrace of about 24 degrees SW is likely the result of the terrace undercutting and rotation during steepening of Fryingpan Canyon by erosion. B.) Sinter is a chemical sediment of layered silica minerals that are deposited by a hot spring.

indicative of local hydrothermal eruptions that occur when fluid pressure exceeds confining pressure (mass and tensile strength of wall rocks).

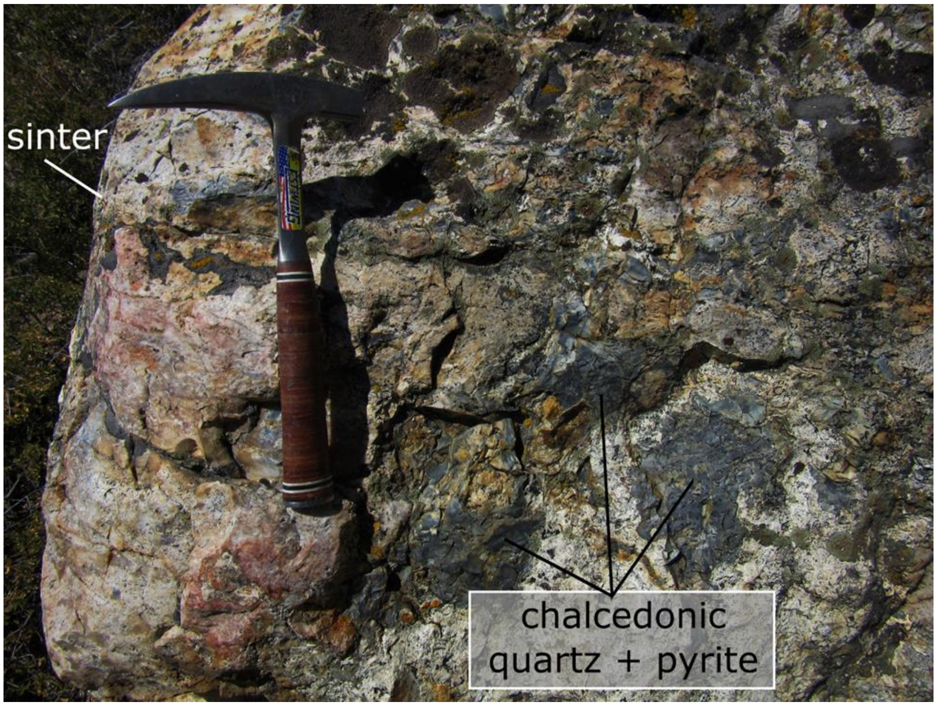

Figure 32. Chalcedonic quartz + pyrite pods within sinter north of Fryingpan Canyon.

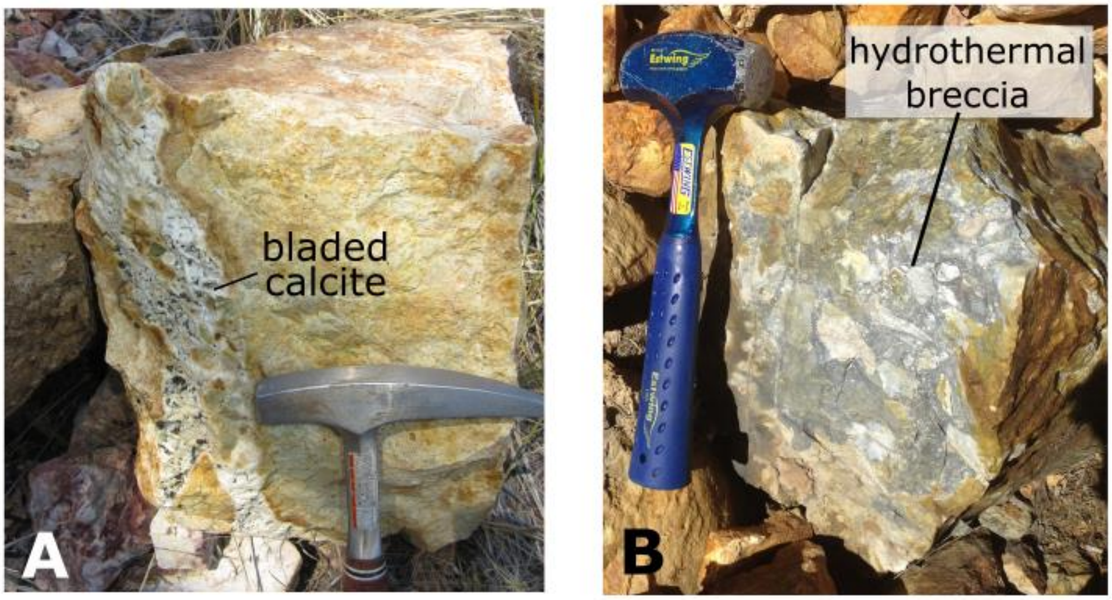

Figure 33. A.) Vein of bladed calcite at the Monte Cristo mine indicative of boiling near the paleosurface. B.) Breccia interpreted as hydrothermal in origin at the Monte Cristo mine. The clasts are aligned and elongated.

Local occurrences of vuggy silica at the Fryingpan Canyon mine (Plate II) imply near-surface condensation of low pH fluid.

Cameron belt silver-gold deposits belong to a subtype of low-sulfidation epithermal deposits known as hot spring gold deposits (Nelson, 1987) that form at or directly beneath the paleosurface. Disseminated mineralization in the Cameron belt was likely deposited by extensive hydrothermal fluid convection through porous and permeable basin-fill near the paleosurface.

Hydrothermally altered rocks in the Cameron belt consist of mostly illite and illite + montmorillonite assemblages (Plate II). Rocks altered to chalcedony ± adularia are also widespread. A few small areas of kaolinite + opal-altered rocks and one area of rocks altered to quartz + alunite at Star City likely represent local steam-heated alteration based on the fine-grained nature of alunite and local opal, and may have formed near the water table (Simmons et al., 2005). Sinter north of Fryingpan Canyon (elevation 8338 feet) indicates that the water table has been lowered approximately 250 feet since the sinter formed based on the current elevation of the water table at Fryingpan Creek (elevation 8084 feet). The sinter likely formed at ~5.6-5.1 Ma based on dates of hydrothermal minerals (Table 1, Fig. 19).

Drilling by Homestake mining company indicated a north-trending zone of mineralized rocks beneath the Monte Cristo mine, measuring 53 feet in thickness with a 21-foot-wide zone of 0.016 oz/ton gold in the hanging wall and including a 11-foot-wide zone of 0.056 oz/ton gold in the footwall, separated by a barren zone of 21 feet thickness (Bybee, 1986). The zone of mineralized rock strikes N50°E and dips 60-70° NW (Bybee, 1986), which is consistent with surface measurements of N-N35°E and dips of 50-75°

NW. The mineralized zone may extend north coincident with hydrothermally altered rocks in the Cameron belt. Quartz + alunite, illite, and kaolinite ± dickite ± opal assemblages occur between the Clinton town site and Cottonwood Canyon. These alteration assemblages are interpreted to be steam-heated in origin and controlled by a north-trending fault.

ii. Clinton belt

Mines of the Clinton belt, which include the Silverado, Kentuck, Frederick (Lady Hayes), and mines at Belfort, produced large amounts of silver from the 1880s-1940s. Silver deposits occur as stockwork vein zones of chalcedony, adularia, coxcomb quartz, and sulfide + telluride minerals in rhyolite (Trd), rhyolite tuff breccia (Trt), and a rhyolite porphyry dike (Trp). Ore with silver grades of 350-1100 opt was mined in the 1920s

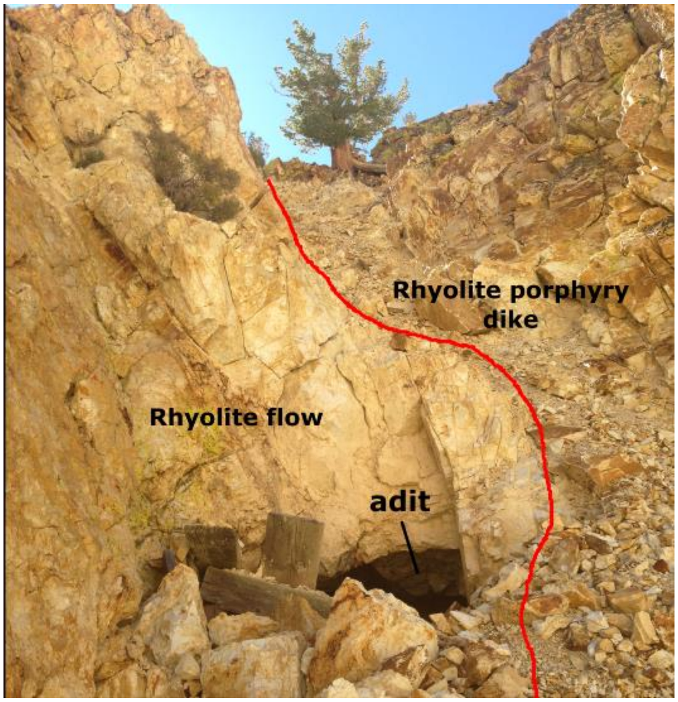

Figure 34. Stockwork veins in mines of the Clinton belt are spatially associated with a 5.9 Ma megacrystic rhyolite porphyry dike. Adits, such as the one pictured above at the Silverado mine, and other mine workings usually occur on the contact of the rhyolite porphyry dike and rhyolite flows (Trd) or tuff-breccia (Trt).

(Hamilton, 1917). Both the Silverado and Kentuck mines contained vertical extents of ~300-400 feet. The silver to gold ratio in the Clinton belt deposits ranges from ~200 to >2000. Silver deposits exhibit a close spatial relationship to a 5.9 Ma rhyolite porphyry dike (Trp) that has a minimum strike length of 3 km (Plate I). Adits and other mine workings nearly always occur at the contact of rhyolite (Trd) or rhyolite tuff-breccia (Trt) and the rhyolite porphyry dike (Trp; Fig. 34).

Typical deposits in the Clinton belt are stockwork veins consisting of thin (≤ 3 cm) closely-spaced quartz veins, some of which are banded (Fig. 35). Stockwork vein zones strike N25°W to N10°E and dip 30-55° W, but are reported to steepen at depth

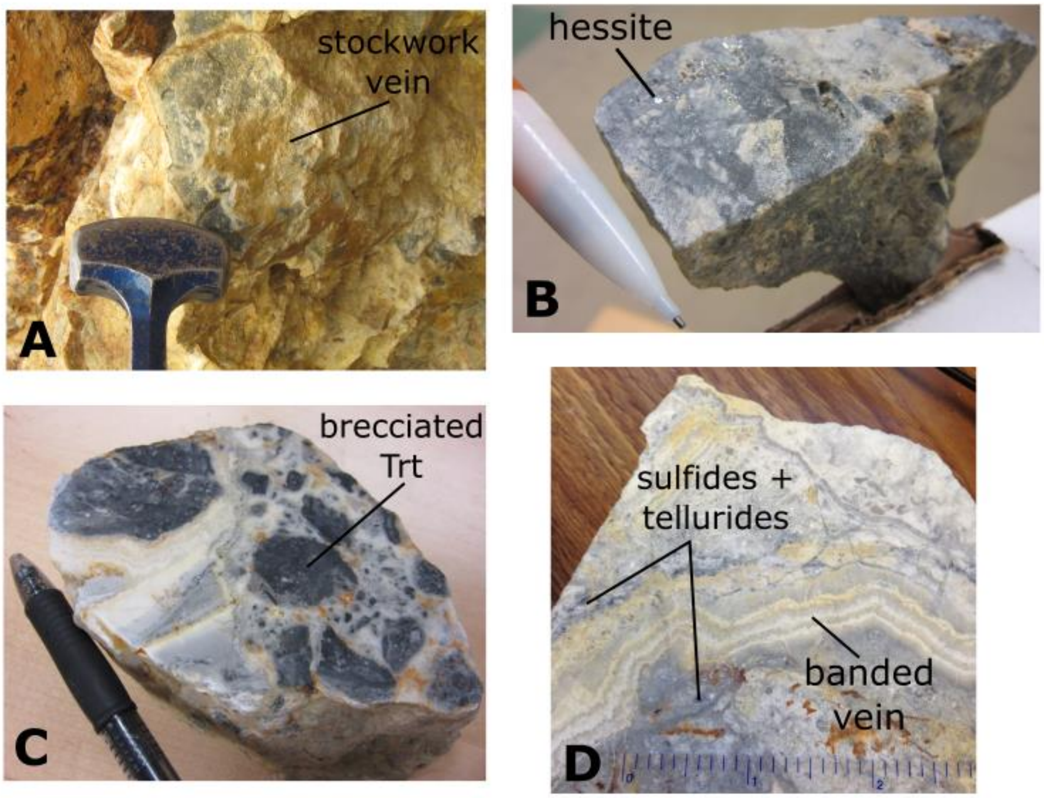

Figure 35. A.) Representative silver stockwork veins in Clinton belt mines. B) The Ag-telluride hessite (Ag_2Te) is a common metallic mineral in dump samples. It is highly reflective on cut surfaces. C.) Sample showing multiple generations of brecciation. D.) Rare layered quartz veins occur in the Clinton belt deposits. However, metallic minerals usually occur in chalcedonic quartz. Scale is inches.

(Bybee, 1986). Dump samples of Clinton belt mines contain hypogene hessite (Ag_2Te), acanthite, chalcopyrite, galena, and sphalerite. The paragenetic relationships observed include early base metal sulfides (pyrite, sphalerite, galena, and chalcopyrite), followed by hessite (Fig. 36), and lastly, a second stage of galena (Fig. 37). The highest grade samples contain abundant hessite after chalcopyrite, intergrown with fine-grained quartz. Acanthite was originally deposited as the cubic polymorph argentite, which is unstable at low temperatures (Roy et al., 1959), but acanthite often retains a cubic crystal form. Acanthite is commonly oxidized to chlorargyrite (AgCl; also known as cerargyrite or horn silver in older reports. Fig. 38). Hessite is oxidized to tellurites such as sonoraite ($Fe^{3+}(TeO_3)(OH) \cdot H_2O$) locally (Fig. 39). Additional SEM images showing these relationships are in Appendix F. The presence of abundant base metal sulfides suggests a

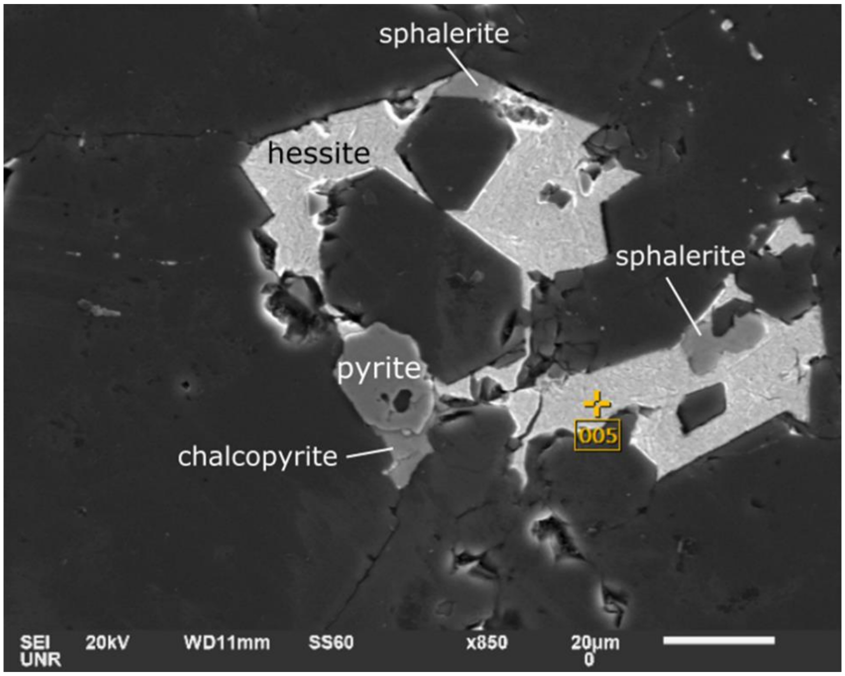

Figure 36. SEM image of sample USV-1 from the Silverado mine. Hessite (Ag_2Te) was precipitated after base metal sulfides.

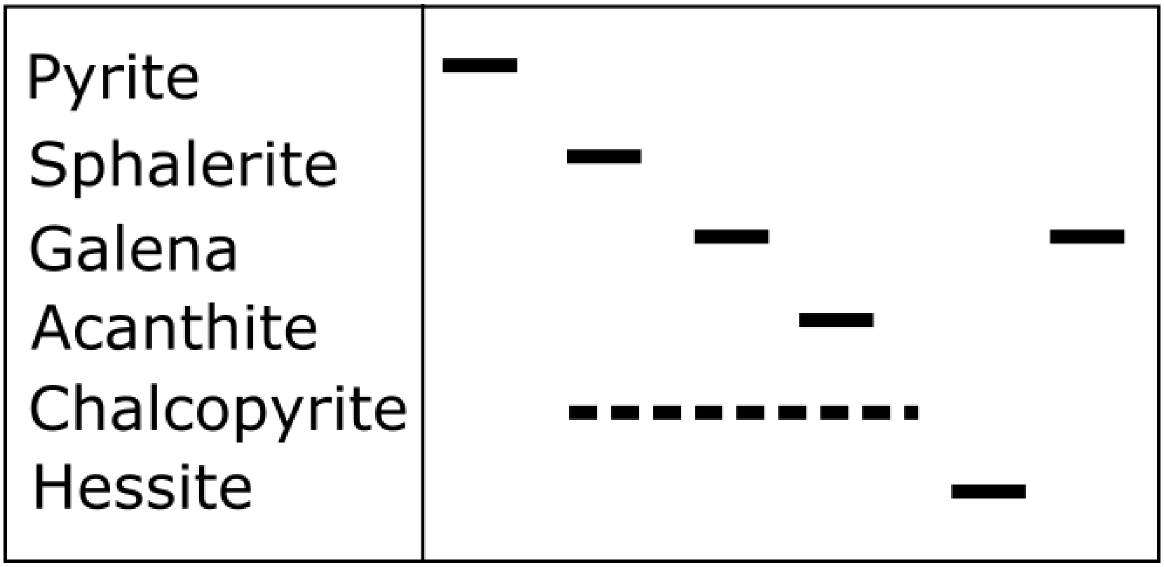

Figure 37. Paragenesis for hypogene minerals in Clinton belt deposits. Base metal sulfides were deposited before hessite, with the exception of late galena.

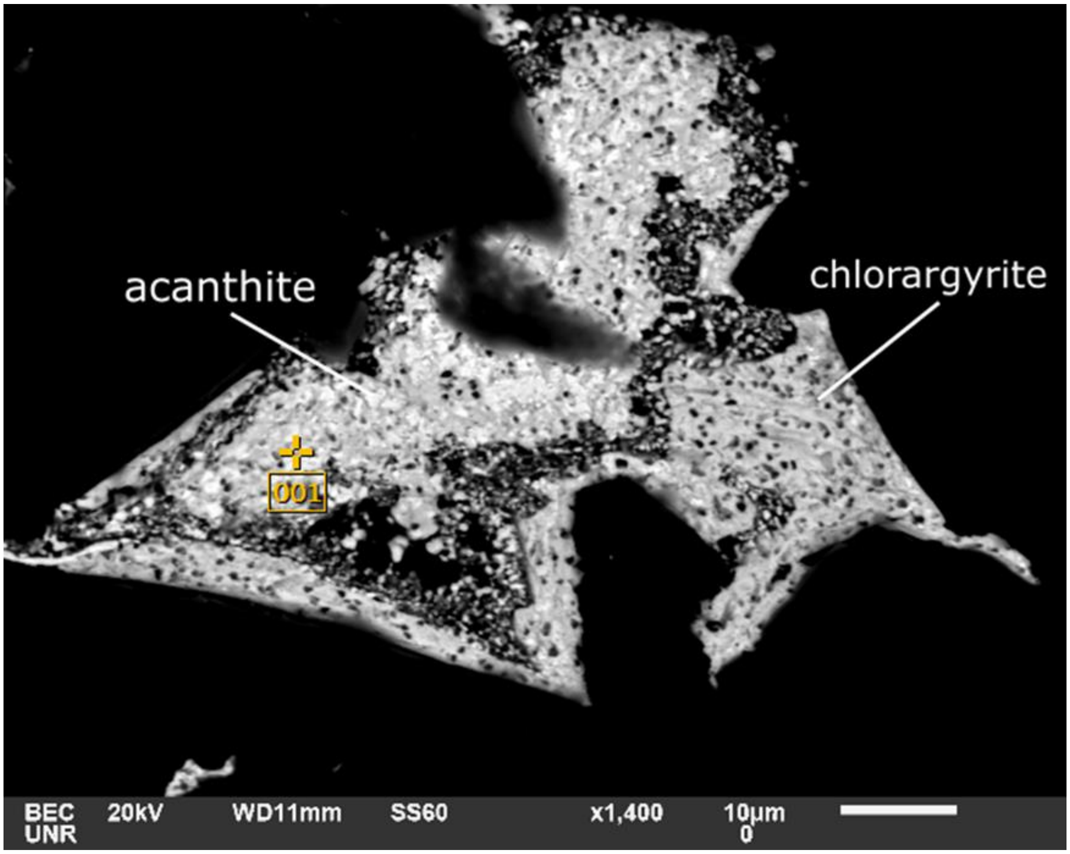

Figure 38. SEM image of sample KTK-5 from the Kentuck mine. Acanthite is commonly oxidized to chlorargyrite in samples from Clinton belt deposits.

greater depth for deposits of the Clinton belt than those of the Cameron belt (Hurtig and Williams-Jones, 2015). There is an absence of bladed calcite in most deposits, which implies that boiling did not occur at the depths these deposits were exploited at. Some samples show evidence for episodic brecciation (Fig. 35C), which along with the presence of adularia and local banded chalcedony suggest boiling occurred somewhere in the system, possibly at depths below historically exploited mineral deposits.

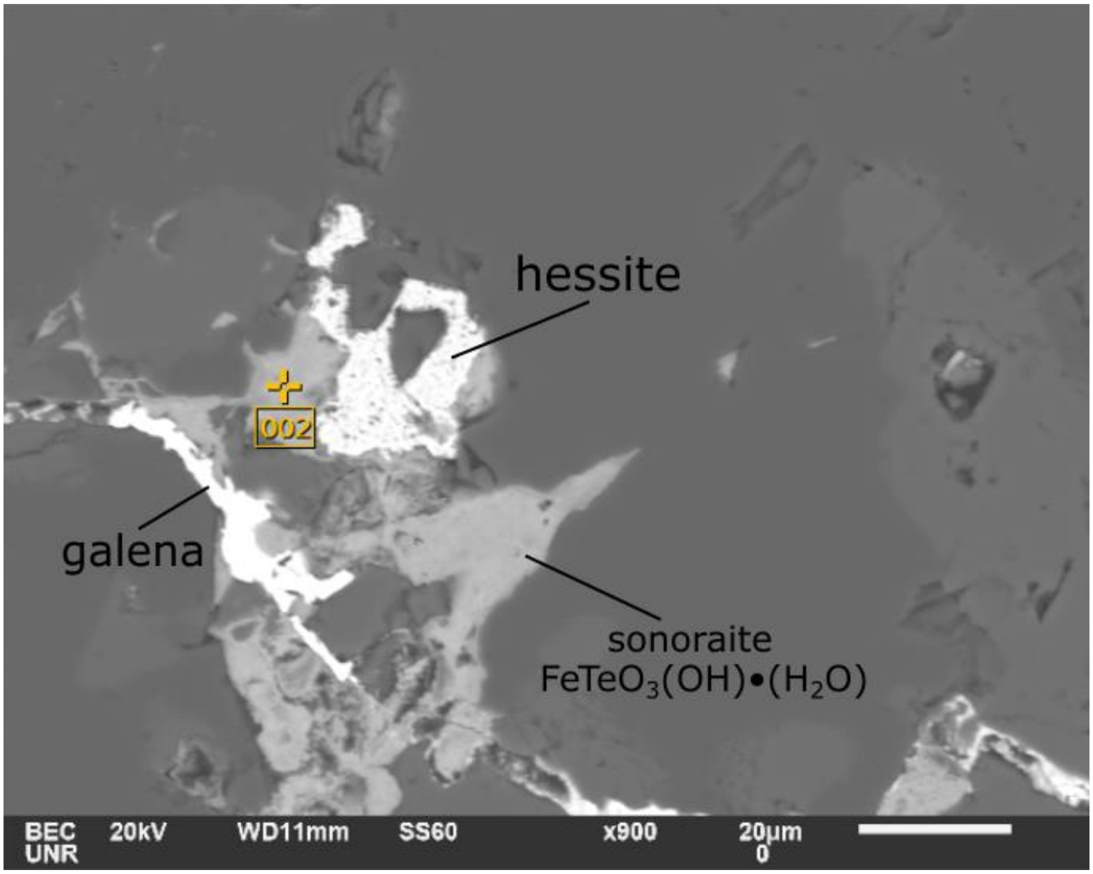

Figure 39. SEM image of sample 188-1 from a mill at the town site of Clinton. Hessite is locally oxidized to tellurites such as sonoraite. Late stage galena cross-cuts sonoraite (formerly hessite).

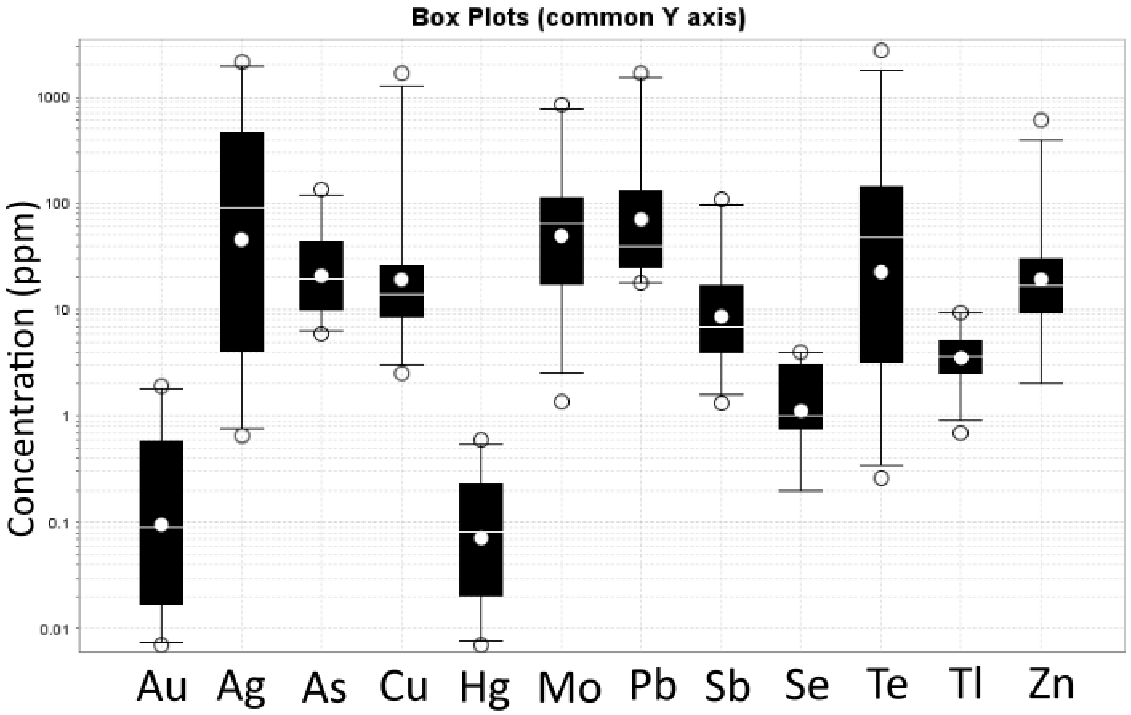

Figure 40. Box plots with a logarithmic Y axis showing concentrations of elements in mineralized samples from the Clinton belt deposits. Each box represents 50% of the concentrations of elements, from quartile 1 (the bottom 25% of the range of concentrations) at the bottom to quartile 3 (the upper 25% of the range of concentrations) at the top. The white circle within the box represents the mean value for that element. The whiskers represent 95% and 5% values. n= 25 samples.

Clinton belt deposits contain high concentrations of Ag, Mo, Pb, Te, and Zn (Fig. 40). Silver grades range from 1-2,120 ppm and average 322 ppm. Gold grades are <0.005 ppm-1.9 ppm, with a mean of 0.33 ppm. No gold minerals were observed. Copper concentrations are locally elevated (concentrations range from 5-1,666 ppm) due to high concentrations of chalcopyrite but are typically not above background concentrations for rhyolite (~60 ppm, Johnson et al., 2013). Concentrations of molybdenum are unusually high for epithermal deposits. They range from 1.4-846 ppm and average 116 ppm, possibly as a result of remobilization of Mo from a deeper porphyry molybdenum system in the Sweetwater Mountains (section VII). No molybdenum minerals were observed in thin section. Lead concentrations range from 18-1,643 ppm and average 236 ppm because of high concentrations of galena, while zinc concentrations range from 2-603 ppm and average 50 ppm because of modest occurrences of sphalerite. Concentrations of tellurium range from 0.2-2,726 ppm and average 207 ppm because of large amounts of hessite, and locally, supergene tellurites in mineralized samples. A dump sample collected at the Silverado mine assayed >27,000 ppm Ag and >12,000 ppm Te (K. Beucke, written communication, 2016). A Spearman correlation matrix (Appendix E) shows that gold is correlated with Ag, Hg, Li, Pb, Sb, Se, Te, and Tl. Silver is correlated with Au, Cd, Hg, Li, Pb, Sb, Se, Te, and Tl.

The Clinton belt includes rocks altered mostly to illite both at higher elevations than and adjacent to mineral deposits (Plate II). Small volumes of rocks altered to illite + montmorillonite also occur in Silverado Canyon and near the Frederick and Tiger mines. Silver-gold deposits include rocks altered to chalcedony + minor illite ± adularia, but are not well exposed on the surface. Along strike of the Belfort-Silverado fault system (Fig. 18) south of Sweetwater Canyon, rocks are altered to kaolinite ± dickite, and illite ± montmorillonite and montmorillonite-only assemblages.

iii. California Comstock belt

Precious metal deposits in the California Comstock belt contain low grades of both gold and silver and were only exploited at the Angelo Mission mine and Star and Great Western claims, likely because of access limited by snow cover during much of the year. Vein and stockwork vein deposits of the California Comstock belt crop out at ~11,000 feet over a strike length of >800 feet. Veins occur in a glassy dacite (Td1) while stockwork occurs in rhyolite tuff-breccia (Trt). The different styles of veining apparently reflect a rheology contrast between host rocks or different hydrothermal events. Veins that occur in dacite (Td1) are 3-9 feet in width and exhibit a branching morphology (Fig. 41). Closely spaced changes in strike of the veins and multiple fault intersections observed imply they were emplaced in a fault relay ramp, which is a favorable setting for hydrothermal fluid flow (Faulds et al., 2011). Attitudes of one vein are N30°W to N30°E with dips of 50-60° east.

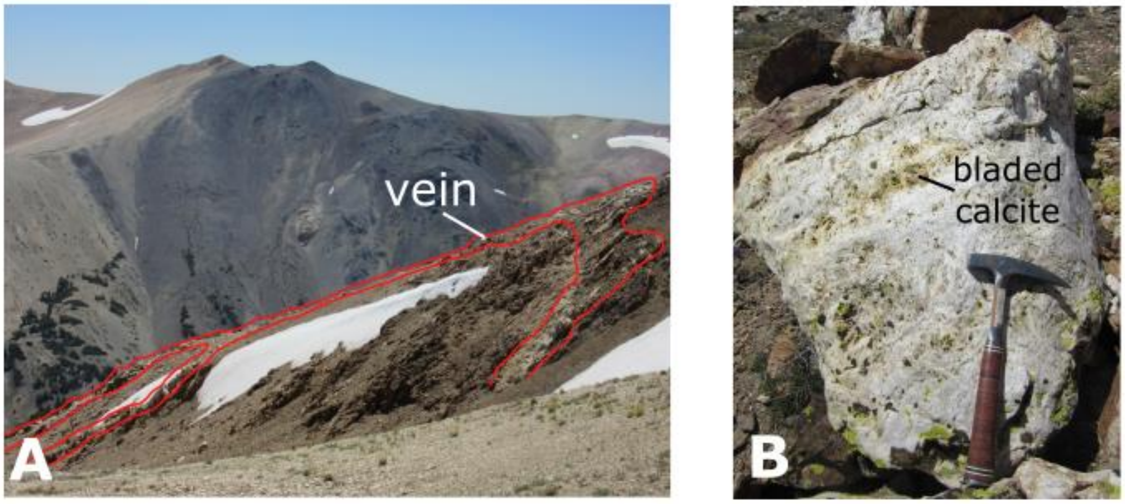

Figure 41. A.) 1-3 m thick veins dipping 50-60° east. Varying strike attitudes and patterns of fault intersections imply emplacement in a fault relay ramp. B.) Veins are composed mostly of bladed calcite, adularia, and quartz.

The veins are composed of layered quartz, massive quartz, adularia, pseudomorphs of quartz after bladed calcite, and thin grey bands of sulfide minerals and electrum (Fig. 42). The grey bands are composed of hypogene electrum, selenium-bearing acanthite, and minor hessite, chalcopyrite, and galena. There are two compositions of electrum in the veins; 28-42 weight percent gold and 58-72 weight percent silver, and 63-72 weight percent gold and 28-37 weight percent silver (Fig. 43, 44). Hessite, electrum, and galena were deposited before acanthite, but other paragenetic relationships are unclear. Acanthite was originally argentite, based on cubic crystal form,

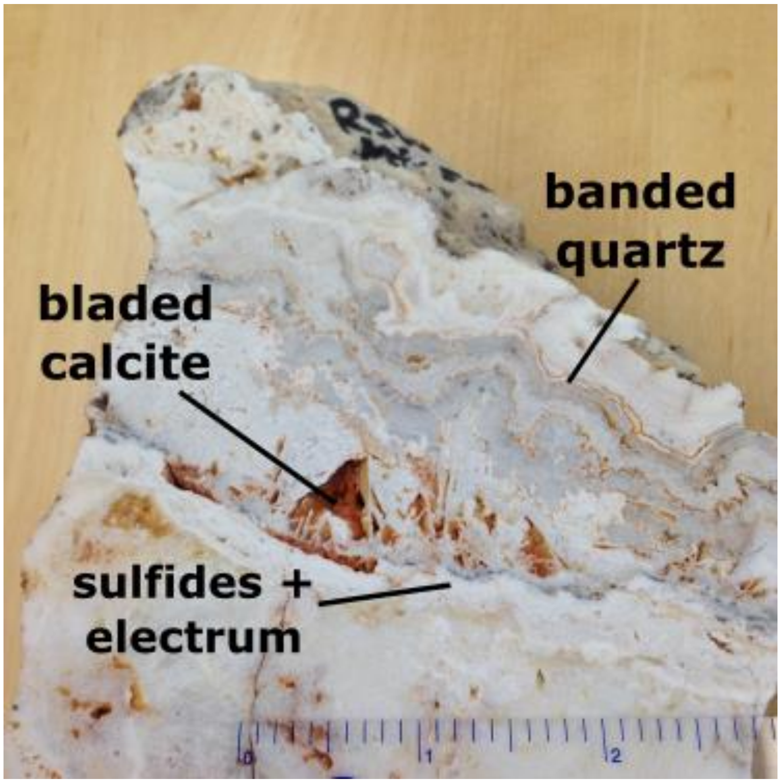

Figure 42. Thin layers of sulfides and electrum occur within layers of bladed calcite and banded quartz.

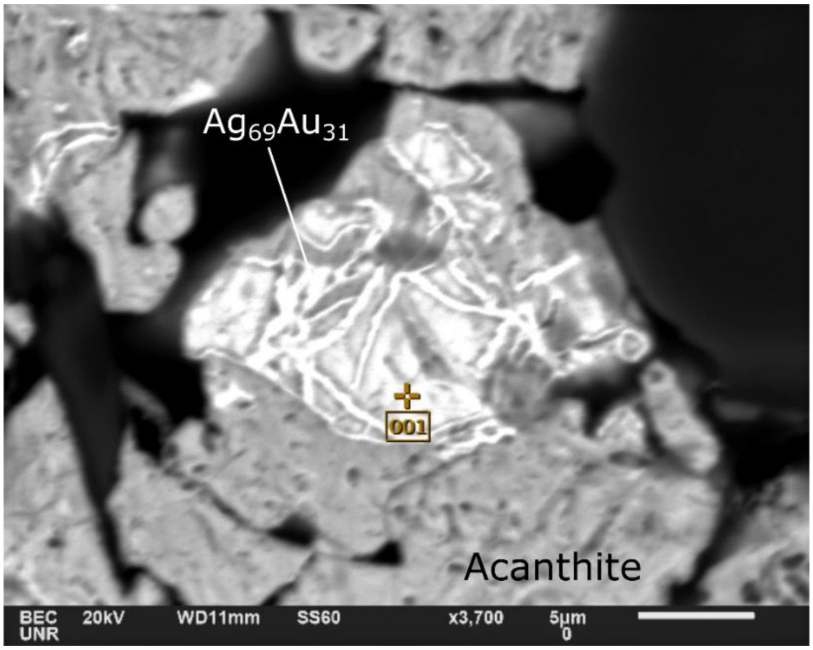

Figure 43. SEM image of electrum (weight %) and acanthite in veins of the California Comstock belt.

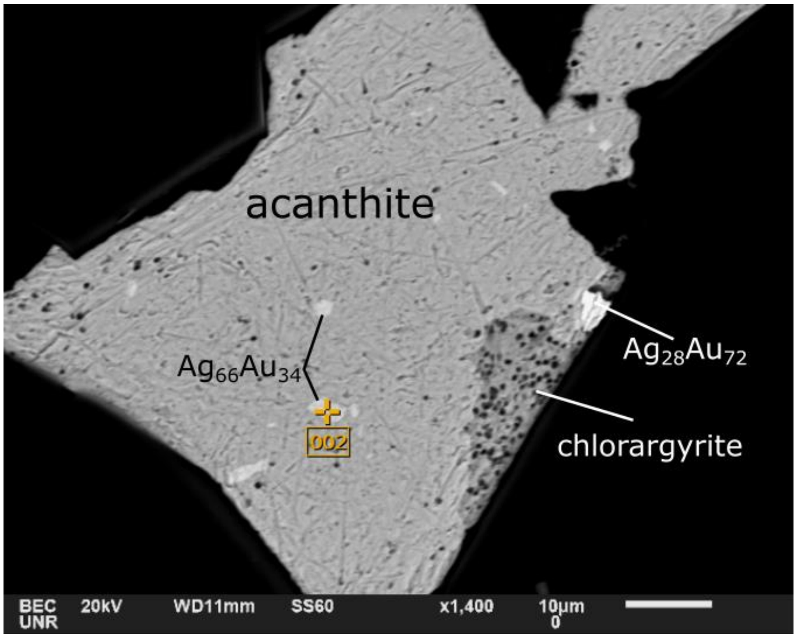

Figure 44. SEM image showing two compositions of electrum (weight %) and acanthite partly oxidized to chlorargyrite.

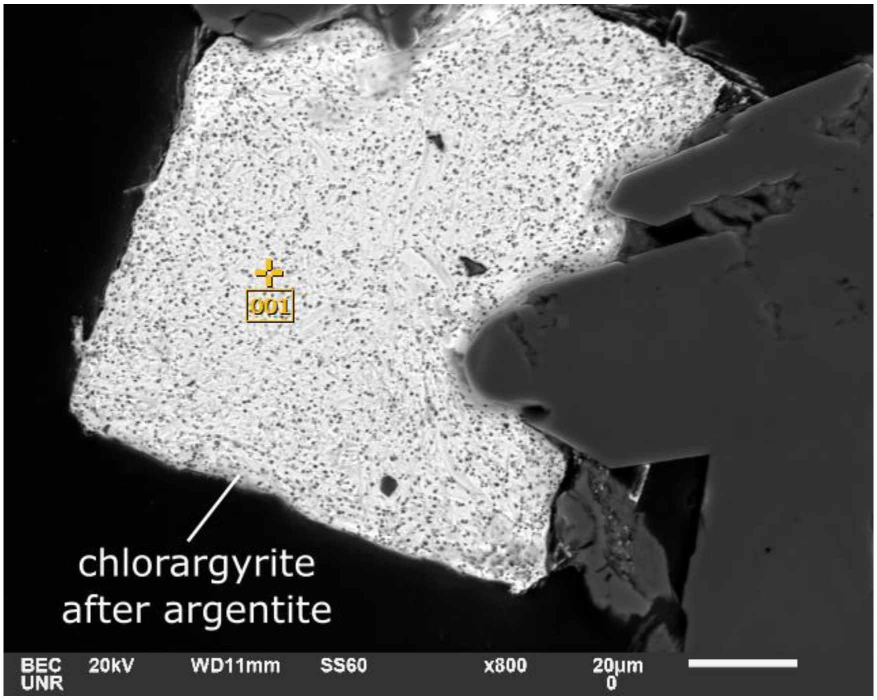

Figure 45. SEM image showing chlorargyrite replacing acanthite. Acanthite was initially deposited as argentite, based on cubic crystal form, but argentite is not stable at temperatures below 176° C.

and contains 1-4 wt. % selenium. Using bladed calcite as a boiling indicator and the minimum temperature of argentite deposition of 176°C, the boiling point-depth curve for pure water (Haas Jr., 1971) can be used to estimate a minimum depth of formation of ~75-100 m below the paleowater table for deposits of the California Comstock belt. Supergene chlorargyrite replaces acanthite (Fig. 45) and jarosite fills voids.

Few samples were analyzed for element concentrations in California Comstock belt deposits. However, there is a distinct geochemical signature of these deposits that includes high concentrations of Au, Ag, Hg, and Se and moderate concentrations of Pb. Gold grades are typically 1-1.5 ppm and silver grades are 100-400 ppm. Mercury values range from 2-42 ppm, selenium concentrations range from <1 to 10 ppm, and lead concentrations range from 30-120 ppm. This geochemical signature fits the mineralogy, with the exception of mercury.

The California Comstock belt includes rocks altered to illite or illite + montmorillonite on Mt. Patterson and near vein subcrop south of Mt. Patterson, quartz + adularia + minor illite in veins and stockwork veins, and fine grained alunite in a rhyolite plug east of the summit (Plate II). Most of Mt. Patterson consists of silicified rhyolite overlying illite-altered unconsolidated strata that may represent a debris flow. A small volume of kaolinite-altered rocks with minor alunite filling leached voids occurs at the summit of Mt. Patterson, and alunite coats fractures in the area. Alunite- and kaolinite-altered rhyolites likely represent steam-heated alteration, similar to alunite-kaolinite altered rocks near the Silverado mill.

VI. Discussion

i. Comparison of silver-gold deposits in the Patterson mining district

Felsic volcanism originating from the Sweetwater volcanic field during the late Miocene-early Pliocene was the source of heat that drove convection of hydrothermal fluids. Hydrothermal fluids rose along three sub-parallel, north-to northeast-trending fault zones, forming three sub-parallel trends of low-sulfidation silver-gold deposits. These three sub-parallel trends are the Cameron, Clinton, and California Comstock belts. The three belts exhibit different deposit forms, silver to gold ratios, mineralogy, and geochemical signatures (Fig. 46, Table 2).

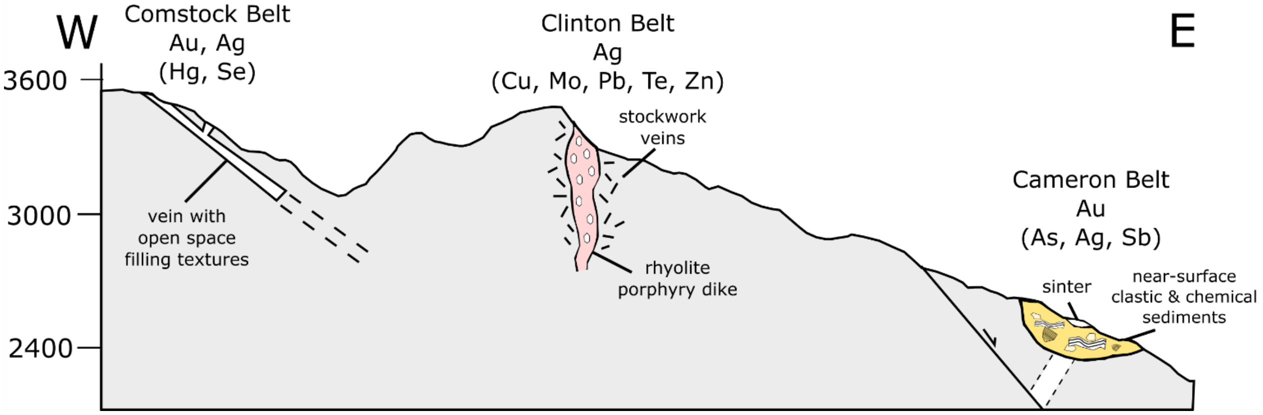

Figure 46. Schematic cross-section of the three precious metal deposit belts of the Patterson district. Belts are distinguished by the commodity that was exploited, and other elements that are anomalous are shown in parentheses. Elevation is given in meters.

	California Comstock	**Clinton**	**Cameron**
Deposit form	Stockwork veins and veins	Stockwork veins	Disseminated
Silver: Gold	100-250	~200- >2000	1-275
Associated trace elements	Hg, Se	Cu, Mo, Pb, Te, Zn	As, Sb
Mineralogy	Acanthite, electrum, chlorargyrite, galena, minor hessite	Pyrite, acanthite, hessite, chalcopyrite, sphalerite, galena, chlorargyrite	Pyrite, acanthite, galena, sphalerite, chalcopyrite
Structure	330-030°, dips 50-60° E	335-010°, dips 30-55° W	0-035°, dips 50-75° W

Table 2. Comparison of deposit form, silver to gold ratio, associated trace elements, mineralogy, and structural trends of the three belts.

Disseminated deposits of the Cameron belt composed mostly of pyrite are characterized by relatively high gold values. These deposits are hot springs type epithermal deposits which formed at and directly underneath the paleosurface as a result of hydrothermal fluid flow through permeable sediments and breccia in a depression. Multiple sinter terraces support a genetic relationship with hot springs. Elements which occur in high concentrations include Au, As, Ag, and Sb.

Zones of stockwork veins in the Clinton belt contain extremely high concentrations of silver which are spatially associated with a rhyolite porphyry dike and a north-trending fault system. There are high concentrations of Ag, Cu, Mo, Pb, Te, and Zn which correlates with high concentrations of base metal sulfides and hessite (Ag_2Te). The high concentrations of base metal sulfides and lack of boiling textures implies deeper formation of these deposits than those of the Cameron belt, or low fluid temperature. High concentrations of hessite suggest a magmatic source for tellurium and possibly other metals (Cooke and McPhail, 2001).

The California Comstock belt consists of veins formed by open space filling within an east-dipping fault zone, which possibly represents a fault relay ramp based on structural measurements. The veins display boiling textures such as quartz pseudomorphs after bladed calcite (Simmons and Christenson, 1994) and there are high concentrations of Au, Ag, Hg, and Se.

ii. Molybdenum occurrences in the Sweetwater Mountains

The occurrence of coarse molybdenite and quartz-sericite-pyrite alteration in Mesozoic intrusive rocks, as well as elevated concentrations of molybdenum, tin, and tungsten in the district, were historically interpreted as evidence for a concealed porphyry molybdenum system by mining companies such as AMAX. Advanced argillic alteration at the top of the range and the occurrence of high concentrations of silver tellurides were also cited as evidence for a possible buried Climax-type porphyry molybdenum system (F. Koutz, written communication). Observations of coarse molybdenite and minor chalcopyrite in aplite within quartz monzonite in Green Creek Canyon (Fig. 47) suggest

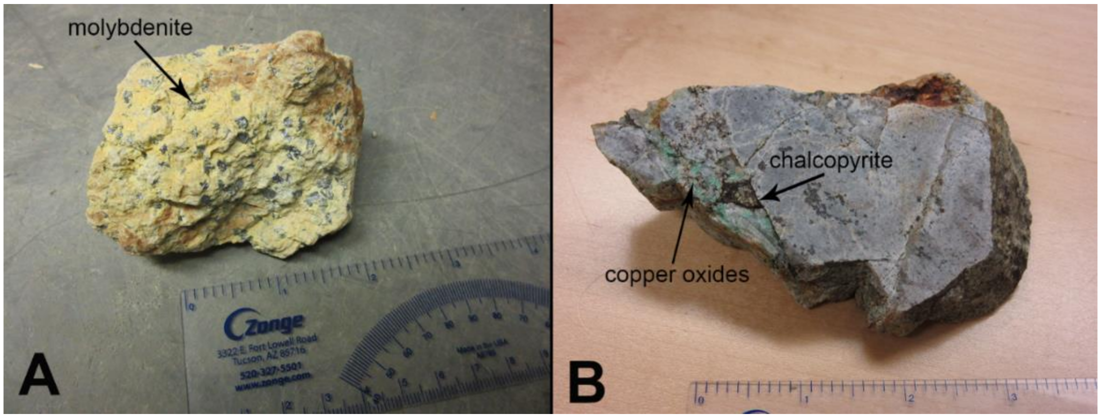

Figure 47. Examples of molybdenite and copper minerals in Mesozoic rocks from Green Creek Canyon that are hypothesized to be Mesozoic in age. A.) Coarse molybdenite and supergene Mo oxides in aplite that is associated with quartz monzonite. This sample contains >1% Mo. B.) Coarse chalcopyrite and secondary Cu oxides within a sugary quartz vein in quartz monzonite.

that some, if not all, of the molybdenum is Mesozoic in age. However, precious metal-bearing fluids that formed Miocene silver-gold deposits may have re-mobilized some molybdenum from underlying Mesozoic deposit(s), which may account for the high Mo values in the Miocene deposits (>800 ppm in Clinton belt deposits).

iii. Context of Miocene silver-gold deposits in the Sweetwater Mountains in the Walker Lane

The volcanic rocks and precious metal deposits of the Sweetwater Mountains belong to a small group of late Miocene-early Pliocene volcanic fields and silver-gold deposits in the Walker Lane. The occurrence of tellurides in precious metal deposits in the Sweetwater Mountains is uncommon among Walker Lane deposits but is not exclusive to the Patterson mining district.

Volcanic rocks of similar age:

The Tertiary volcanic rocks of the Sweetwater Mountains volcanic center represent volcanism which lagged behind the southern edge of the subducting Farallon slab (du Bray et al., 2014; Fig. 48). It has recently been recognized that epithermal and porphyry deposits can be associated with post-subduction magmatism (Richards, 2009), which may represent an underexplored terrane in the western United States. Post-subduction volcanic rocks, such as those in the Sweetwater Mountains and in the other volcanic fields in the Walker Lane have potential for epithermal and possibly porphyry deposits. Volcanic rocks of similar age to Miocene volcanic rocks in the Sweetwater Mountains (~7-5 Ma) are not uncommon in the Walker Lane (Fig. 49) and there was widespread mafic magmatism from 7-2 Ma (du Bray et al., 2014); however, rhyolites and dacites of similar age are found at <30 localities (Fig. 49; Walker et al., 2014) listed in the Western North America Volcanic and Intrusive Rock Database (NAVDAT). While NAVDAT does not represent an exhaustive list of volcanic rock ages and compositions, felsic volcanism was uncommon from 7-5 Ma, especially south of the southern edge of the subducting slab (du Bray et al., 2014, Fig. 48).

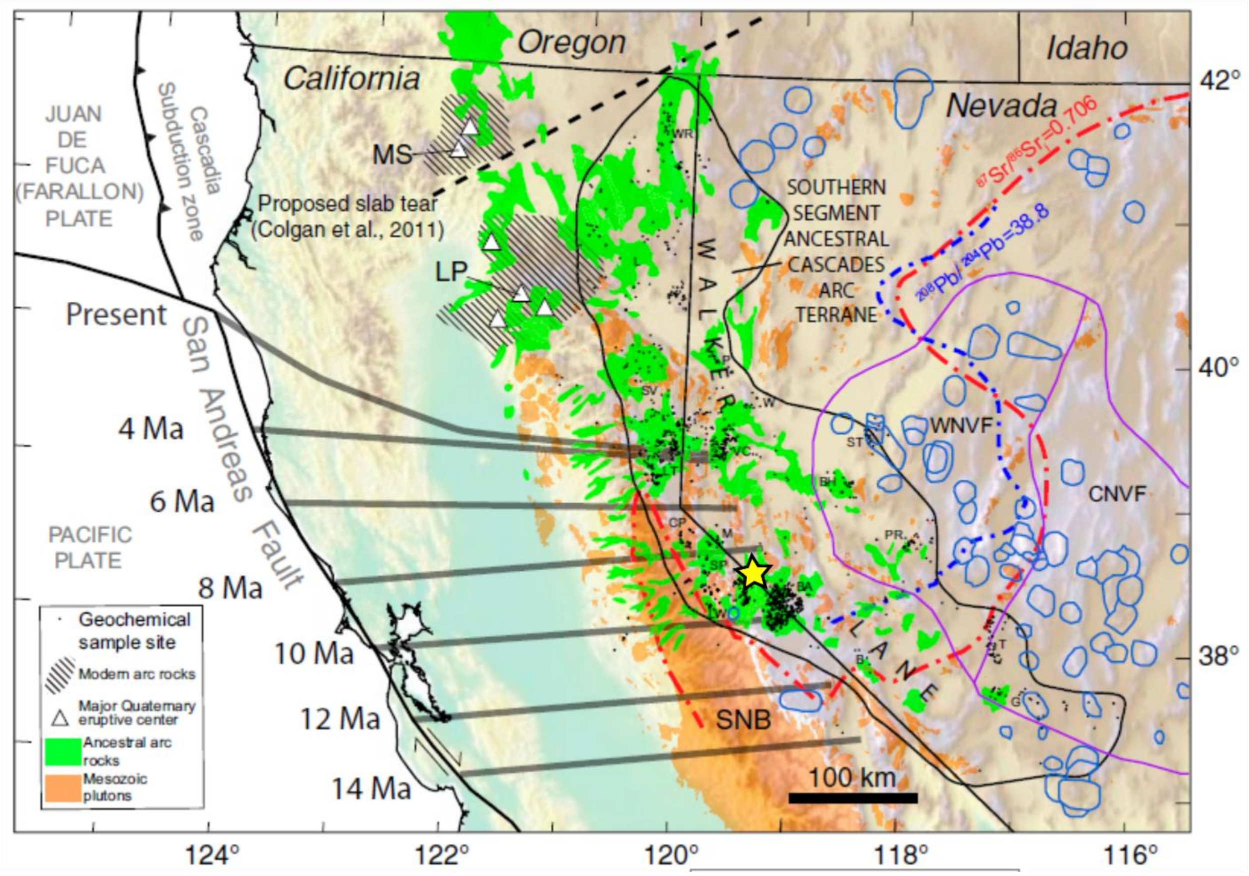

Figure 48. Map of northern California and western Nevada (du Bray et al., 2014) showing the inferred extent of ancestral (green polygons) and modern High Cascades magmatic (cross hatched polygons) arcs. Geochemical ample sites of ancestral Cascade arc rocks are from the geochemical database of du Bray et al. (2009). Subhorizontal gray lines show the southern edge of the subducting Farallon plate at the time specified. Volcanism in the Sweetwater Mountains, marked by a yellow star, was south of the southern edge of the subducting plate at 6.5-5 Ma.

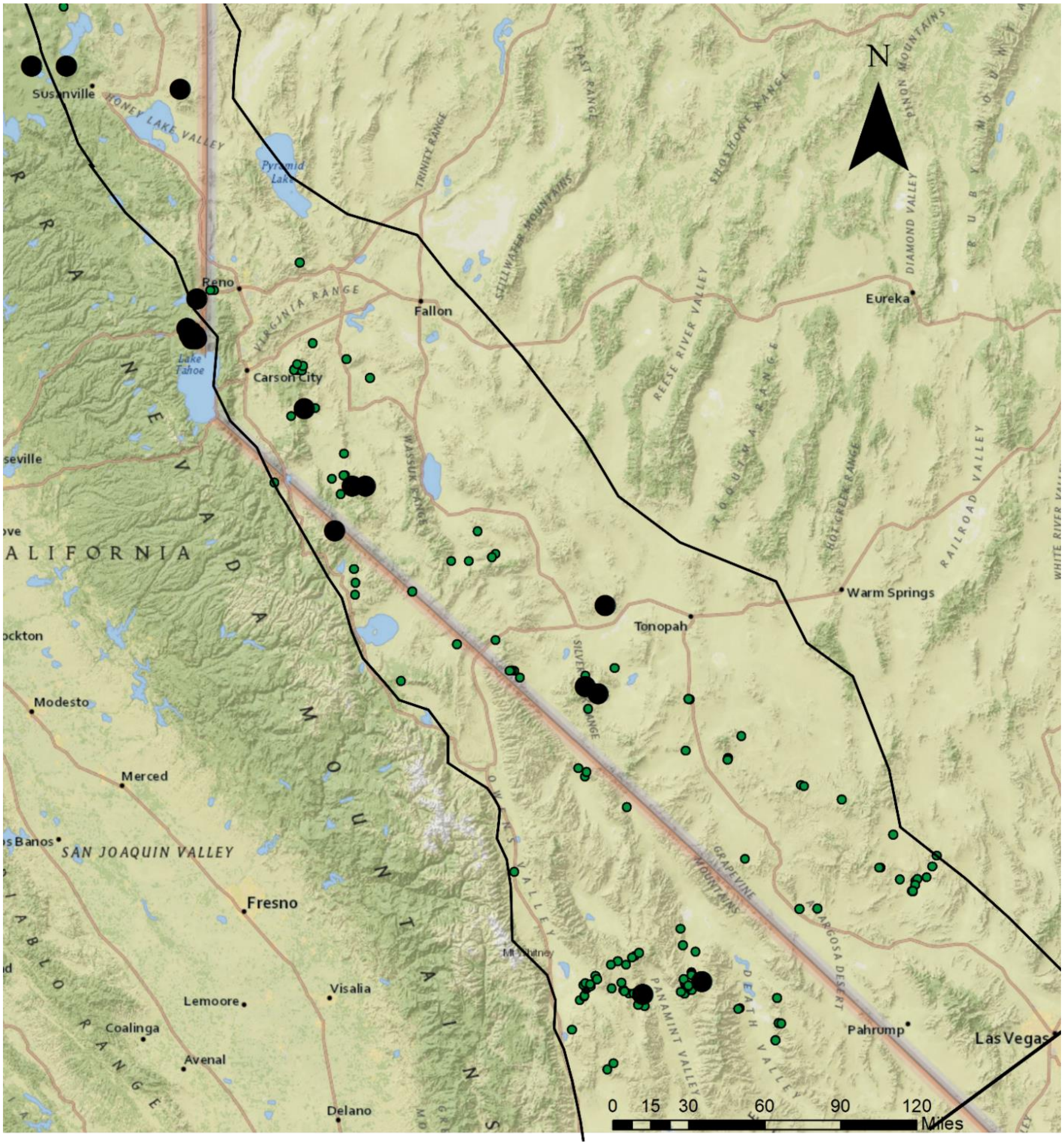

Figure 49. Data compiled from NAVDAT showing distribution of 7-5 Ma volcanic rocks in the Walker Lane (black outline), with dacites and rhyolites symbolized with black circles and volcanic rocks of more mafic composition symbolized with green circles.

There are some examples of volcanism of a similar age and composition in landforms adjacent to the Sweetwater Mountains. The Bodie Hills and Pine Grove Hills both contain rhyolite flows and domes of similar age to rhyolites in the Sweetwater Mountains. Rhyolite domes of the Bodie Hills volcanic field (Rhyolite of Big Alkali) intruded at 6.2-5.5 Ma (John et al., 2012). The domes are volumetrically minor but likely represent the same stage of volcanism observed in the Sweetwater Mountains. The Pine Grove Rhyolite in the Pine Grove Hills to the northeast of the Sweetwater Mountains is 7.6-5.8 Ma and consists of flow-banded rhyolite flows, domes, dikes, and plugs (Eng et al., 2015). Other rhyolites of similar age, such as in the Monte Cristo Range (Stewart et al., 1984) and those erupted from the Silver Peak caldera (Robinson, 1972) are situated >100 kilometers to the southeast.

Epithermal deposits of similar age:

Several mining districts in western Nevada and eastern California contain volcanic rocks and epithermal silver-gold mineral deposits of similar age (~7-5 Ma) to those in the Sweetwater Mountains. These districts include the Como, Gilbert, Pine Grove, and Silver Peak (Red Mountain) districts (Fig. 50). With the exception of the Como district, mineral deposits are associated with felsic volcanism.

The Como district in the northern Pine Nut Mountains produced $500,000 from ~100,000 tons of ore mined from gold-silver veins (Vikre and McKee, 1994). The Pine Nut Mountains, which are situated to the north of the Sweetwater Mountains, contain ~7.5-6 Ma andesites, ~6.3-6.0 Ma coarsely porphyritic dacite intrusions, and ~4.6-2.8 Ma

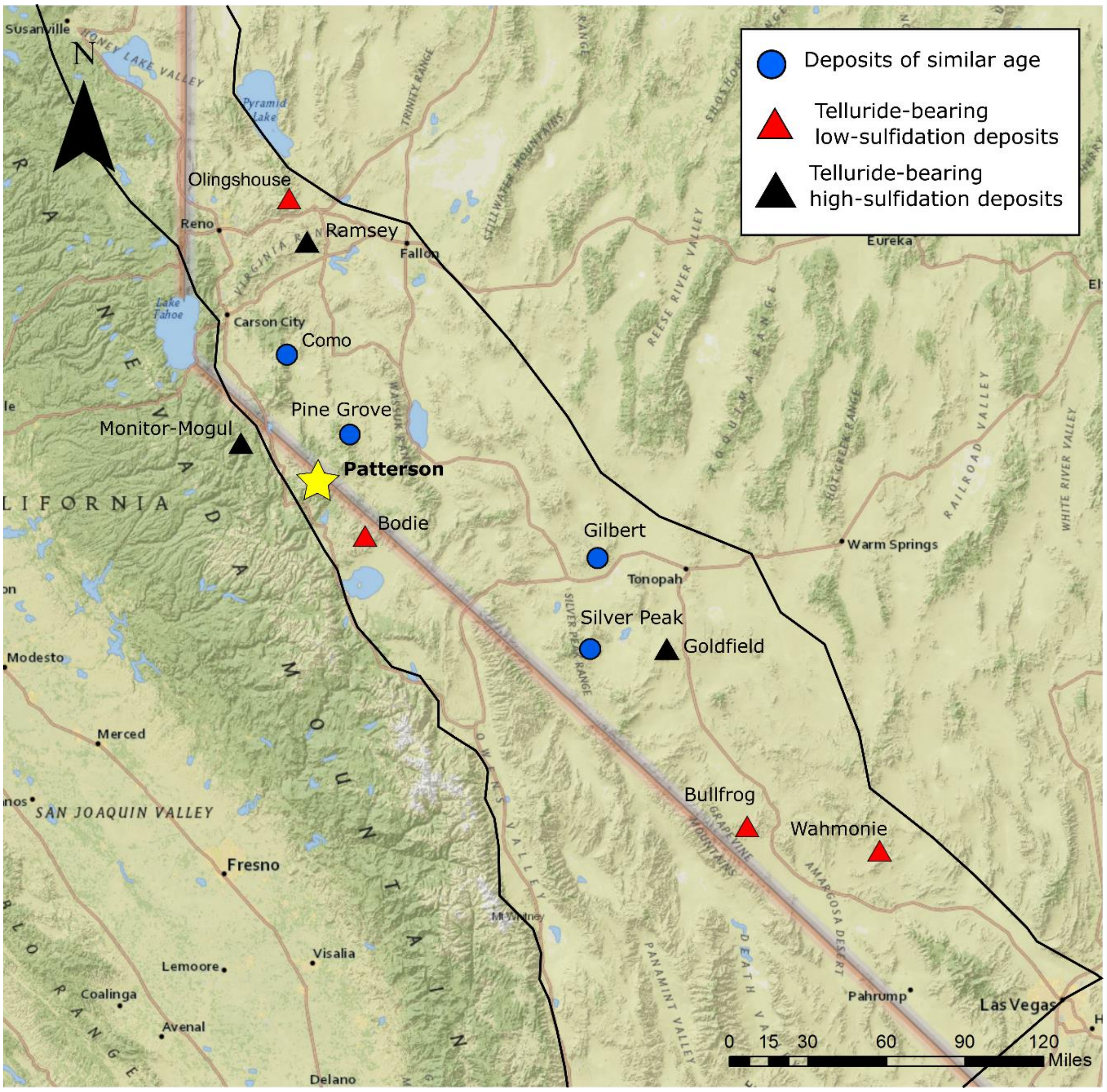

Figure 50. Locations of precious metal deposits of similar age (blue circles) to those in the Patterson district and precious metal deposits that contain tellurides (red triangles) and high-sulfidation epithermal deposits that contain tellurides (black triangles).

dacites (Vikre and McKee, 1994). There are three vein orientations; in the western half of the district veins trend N60°E ± 15° and dip steeply southeast to vertically or north-south ± 25° and dip steeply northwest to vertically. Veins in the southeastern part of the district trend N55°W and north-south ± 25° and dip moderately northeast (Vikre and McKee, 1994). Tetrahedrite, electrum, chlorargyrite pyrite, marcasite, sphalerite, stibnite, chalcopyrite, and pyrargyrite occur in veins which strike north-south (Moore and Archbold, 1969; Vikre and McKee, 1994). Vein adularia is ~7-6.6 Ma, and alunite in altered andesite is ~6 Ma (Vikre and McKee, 1994). Much like the Patterson district, hydrothermal activity occurred contemporaneous with or immediately following volcanism (Vikre and McKee, 1994).

The Gilbert district in the Monte Cristo Range near Tonopah produced 4,465 tons of gold and silver ore with a reported value of $105,000 (Carraher and Hudson, 2015). The district is dominated by caldera-related Tertiary volcanic rocks ranging in age from 24-5 Ma (Carraher and Hudson, 2015) and by rocks of the Ordovician Palmetto Formation. Volcanic rocks thought to be associated with epithermal mineral deposits are ~7.2-5 Ma and consist of basalts and rhyolites. Most veins are spatially associated with intrusive rhyolites and contain electrum, argentite, chlorargyrite, and pyrargyrite (Albers and Stewart, 1972). Gold-silver vein deposits formed in three, sub-parallel, northeast-trending fault zones (Carraher and Hudson, 2015), much like in the Patterson district. Vein adularia is 8.1 Ma (Stewart et al., 1984).

The Rockland mine in the Pine Grove district situated to the northeast of the Sweetwater Mountains produced 50,000 ounces of gold from NNE- to NE- trending veins formed in steeply dipping faults (Eng et al. 2015). The northern Pine Grove Hills contain much of the same Mesozoic and Tertiary volcanic stratigraphy as the Sweetwater Mountains, and gold-silver deposits are associated with a ~7.6-5.8 Ma rhyolite dome field (Eng et al., 2015). There are at least two zones of epithermal quartz veining which strike N10-60° E, one which dips steeply east (Rockland Mine) and another which dips steeply west (Eastside Corridor). Gold at the Rockland mine occurs in crustiform-banded veins, vein breccias, and stockwork zones associated with a NNE-trending, steeply east-dipping rhyolite dike (Eng et al., 2015), similar to deposits in the Clinton belt in the Patterson district. Sulfide and ore minerals in the mine include electrum, pyrite, pyrargyrite, and argentite, with minor stephanite and covellite. High concentrations of Mo (100-150 ppm) occur in drill holes (Eng et al., 2015). The rhyolite domes and epithermal deposits in the Rockland mine area are shallowly eroded, much like those in the Sweetwater Mountains. The Pine Grove Hills contain a Mesozoic porphyry Cu deposit associated with the Jurassic Lobdell Summit Pluton (Princehouse and Dilles, 1996), similar to the possible porphyry Mo deposit associated with Mesozoic plutons in the Patterson district.

The Silver Peak (Red Mountain) district produced between $2 million and $3 million from the Nivloc mine from ore averaging 11 ounces/ton silver, 0.05 ounces/ton gold and 106,400 tons from the Mohawk mine from ore averaging 18 ounces/ton silver, and the Sixteen-to-One mine produced >5 million ounces silver and 11,000 ounces gold (Cline, 1986). Silver-gold deposits occur in Miocene volcanic rocks, breccias, tuffs, and sedimentary rocks associated with the Silver Peak caldera (Keith, 1977; Robinson, 1972). The ~6.1-4.8 Ma Silver Peak caldera consists of rocks which range in composition from trachybasalt to rhyolite, with latite being the most voluminous rock type (Robinson, 1972). High angle faults generally strike N 20-40° E in the district (Keith, 1977). Silver-rich epithermal deposits consist mainly of quartz, calcite, and acanthite with minor galena, sphalerite, and chalcopyrite, and are latest Miocene or early Pliocene in age (Keith, 1977). Adularia adjacent to the Sixteen-to-One vein is 5.0 Ma (Cline, 1986).

Other sulfide and ore minerals in veins are native silver, pyrargyrite, polybasite, stephanite, tetrahedrite, stromeyerite, marcasite, and covellite (Cline, 1986).

Several quartz-alunite alteration cells in the ancestral Cascades arc are <10 Ma (Vikre and Henry, 2010) Those most similar in age to hydrothermal activity in the Sweetwater Mountains are located north of Lake Tahoe, and include Golden Dome (~7 Ma), Sardine Peak and Bear Valley Campground (6.4 Ma) and Brockway Summit (4.7 Ma). Ages of alteration cells and volcanic host rocks are similar, which supports a genetic link between magmatism and alteration (Vikre and Henry, 2010), similar to the age correlation observed between magmatism and alteration in many quartz-adularia deposits in the Ancestral Cascades.

Epithermal precious metal deposits with similar mineralogy:

Hypogene minerals in silver-gold deposits in the Patterson district include electrum, acanthite, pyrite, chalcopyrite, galena, sphalerite, molybdenite, and hessite. These metallic minerals are common in epithermal deposits in the Walker Lane, with the exception of molybdenite and hessite, which occur only in a minority of deposits.

Low sulfidation epithermal deposits which contain tellurides in the Walker Lane are found in the Bodie, Bullfrog, Olingshouse, and Wahmonie districts, as well as in the Patterson district (Fig. 50). High sulfidation deposits such as those in the Goldfield, Ramsay, and Monitor-Mogul districts also contain telluride minerals. While the precious metal deposits associated with the Bodie Hills volcanic field (~13-8 Ma) are older than those in the Sweetwater Mountains, there is a notable similarity in the occurrence of tellurium. The Silver Hill series veins in the Bodie district strikes N- N20°E, dips 50°E, and vein adularia is 8.9-8.5 Ma (Vikre et al., 2015). Silver Hill series veins have the highest Ag:Au in the Bodie district and contain hessite and Au-Ag-Te phases, as well as electrum, acanthite, galena, sphalerite, pyrite, chalcopyrite, bornite, and tetrahedrite (Vikre et al., 2015). Tellurium concentrations in some dump and archival samples exceed 500 ppm, illustrating that Te-rich epithermal veins are not limited to the Patterson district.

Most other epithermal precious metal deposits that contain hessite and other tellurium minerals in the Walker Lane are associated with the southwestern Nevada volcanic field, which formed from 15-7 Ma (Castor and Weiss, 1992). The Bullfrog mine contains silver-gold tellurides, altaite (PbTe), and hessite in ~10 Ma veins (Castor and Ferdock, 2004; Eng et al., 1996). The Wahmonie district, which is within the Nevada Test Site, was mined for silver-rich veins associated with intermediate to felsic volcanic rocks and subvolcanic intrusions (Castor and Weiss, 1992). Northeast-trending veins contain electrum, acanthite, chlorargyrite, hessite and iron tellurites, and are ~12.9-12.6 Ma based on adularia dates (Castor and Weiss, 1992). Telluride minerals, including petzite (Ag_3AuTe_2) and hessite are also reported from the Olingshouse district 44 km northeast of Reno.

Hessite occurs with other tellurides such as petzite and sylvanite in the Goldfield district (Castor and Ferdock, 2004); however, Goldfield is an example of a high-sulfidation epithermal deposit, in which telluride minerals are much more common than in low-sulfidation epithermal deposits. Other high sulfidation epithermal deposits in the Walker Lane such as in the Ramsey and Monitor-Mogul districts also contain telluride minerals (Vikre and Henry, 2010).

VII. Conclusions

Tertiary volcanic rocks in the Patterson mining district are high K calc-alkaline to shoshonite series andesites, dacites, and rhyolites that make up the Sweetwater volcanic field, a late Miocene to early Pliocene felsic eruptive center. Andesites are small volume and pre-date more voluminous dacitic and rhyolitic volcanism of the volcanic field. Dacites erupted from ~6.6-6.0 Ma and rhyolites erupted from ~5.9-5.3 Ma. At least four dacite units and seven rhyolite units occur in the mapped area, based on geochemistry (Appendix A), mineralogy, and texture. Volcanic rocks range in thickness from <10 to ~200 m in thickness and consist of flows and domes.

Silver-gold deposits of the Patterson mining district are classified as low-sulfidation epithermal deposits, on the basis of mineralogy, which includes quartz + illite ± calcite ± adularia, electrum, acanthite, and hessite and textures, which include banded colloform-crustiform quartz and quartz pseudomorphs of bladed calcite. These deposits are closely related with Miocene-Pliocene felsic volcanic rocks spatially and are contemporaneous with or post-date rhyolitic volcanism based on adularia and alunite dates of ~5.6-5.1 Ma.

More than 180 km^2 of altered rocks are exposed in the Sweetwater Mountains. Rocks were altered by hydrothermal fluid flow through permeable volcanic rocks and three north- to northeast-trending faults, fault zones, or systems of faults. Fluid flow through these faults produced three north- to northeast trends of silver-gold deposits simultaneously with alteration: the Cameron belt, the Clinton belt, and the California Comstock belt. The Cameron belt deposits contain the highest gold grades in the district.

Gold and silver minerals are disseminated in northeast-trending, west-dipping zones consisting mostly of chalcedonic quartz, pyrite, and minor silver and base metal sulfides in voids and as <10 µm inclusions in pyrite. Multiple sinter terraces, which are in part eroded, support a near-surface, hot-spring type environment of formation. The Clinton belt deposits contain high concentrations of silver in stockwork quartz veins that are spatially associated with a rhyolite porphyry dike (Trp). Veins consitst of quartz, adularia, illite, acanthite, hessite (Ag_2Te), and base metal sulfides. The California Comstock belt deposits occur as stockwork veins and 1-3 m wide quartz veins which contain abundant quartz pseudomorphs of bladed calcite. Other vein minerals are electrum, acanthite, and minor hessite. Weathering of deposits in the Clinton and California Comstock belts commonly oxidized acanthite to chlorargyrite. Molybdenum occurrences in the district are unrelated to Miocene volcanic rocks and silver-gold deposits and are thought to be Mesozoic.

Volcanic rocks and silver-gold deposits of the Patterson district belong to a small group of ~7-5 Ma volcanic fields and low-sulfidation epithermal deposits in the Walker Lane. Felsic volcanism occurring at 7-5 Ma is uncommon in the Walker Lane; most 7-5 Ma volcanic rocks are mafic to intermediate in composition. Volcanism that formed the Sweetwater volcanic field occurred south of the southern edge of the subducting Farallon plate. Low-sulfidation silver-gold deposits of similar age are found in the Como, Gilbert, Pine Nut, and Silver Peak mining districts. With the exception of Como, these deposits are spatially and temporally associated with felsic volcanism. Other deposits that contain telluride minerals in the Walker Lane include the Silver Hill series veins in the Bodie district and deposits associated with the southwestern Nevada volcanic field in the

Bullfrog and Wahmonie districts. These deposits vary in age from the middle to late Miocene (13-8 Ma).

Recommendations for future work in the Patterson district include more detailed structural mapping, $^{40}Ar/^{39}Ar$ dates on adularia from deposits of the Cameron and California Comstock belts, Re-Os dating of molybdenite from the proposed underlying porphyry Mo system, identification of gold minerals in the Cameron belt, and determination of oxygen and hydrogen isotopes of gangue minerals in the Clinton belt deposits. Detailed structural mapping would determine if the mineral belts formed in a km-scale fault relay ramp and if there are fault intersections which have potential for high grade mineral deposits. While any adularia dates will likely be ~6-5 Ma, obtaining dates of adularia from the Cameron and California Comstock belt deposits would determine the relative ages of the three mineral belts. Re-Os dating of coarse molybdenite would determine the age relationship between epithermal deposits and molybdenum deposits. Understanding of hot springs-related deposits of the Cameron belt could be aided by determination of the mineralogy of gold in higher grade samples than those analyzed in this study. It is unknown if the gold is in solid solution in pyrite, or if it occurs as disseminated native gold or electrum. Telluride-bearing precious metal deposits are thought to be the result of a larger magmatic input into hydrothermal systems (Cooke and McPhail, 2001), and δD and $\delta^{18}O$ isotope values would test this hypothesis for hessite-bearing deposits of the Clinton belt.

Future work in the Walker Lane could include a more thorough investigation of low-sulfidation epithermal deposits which contain telluride minerals, including their age and geochemistry. It is especially important to determine if these deposits are commonly associated with post-subduction volcanic rocks, since deposits that contain tellurides often form after a change in tectonic environment (Ciobanu et al., 2009). Identifying the tectonic controls on telluride-bearing precious metal deposits in the Walker Lane could help understanding of Au-Ag-Te deposits worldwide. Identification and characterization of precious metal deposits that contain high concentrations of Mo in the Walker Lane could also increase understanding of the genesis of these deposits. It has been suggested that precious metal deposits which contain high Mo in the Walker Lane could be linked to underlying porphyry systems (Castor and Weiss, 1992), but this claim has not been proved through drilling or dating.

References

Albers, J.P., Stewart, J.H., 1972, Geology and Mineral Deposits of Esmeralda County, Nevada. Nevada Bureau of Mines and Geology Bulletin, v. 78, p. 64–72.

Barton, M.D., Young, S., 2002, Non-pegmatitic Deposits of Beryllium: Mineralogy, Geology, Phase Equilibria and Origin, Reviews in Mineralogy and Geochemistry, v. 50, p. 591–691.

Bateman, P., 1992, Plutonism in the Central Part of the Sierra Nevada Batholith, California, US Geological Survey Professional Paper 1483.

Brem, G.F., 1984, Geologic Map of the Sweetwater Roadless Area, Mono County, California and Douglas and Lyon Counties, Nevada (Map), USGS MF-1535-B.

Brem, G.F., 1983, Mineral Resource Potential of the Sweetwater Roadless Area, Mono County, California and Lyon and Douglas Counties, Nevada, USGS MF-1535-A.

Bybee, R., 1986, Summary Report fot the Star City Prospect, Mono County, California, unpublished report, Homestake mining, 114 p.

Cannulli, M., 2003, Wheeler Peak/Star City Project, Mono County, California, unpublished report, 20 p.

Carraher, R.A., Hudson, D.M., 2015, Geology and Mineralization of the McLean Lode, Monte Cristo Property, Esmeralda County, Nevada, in: New Concepts and Discoveries: GSN 2015 Symposium Proceedings. p. 789–802.

Castor, S.B., Ferdock, G.C., 2004, Minerals of Nevada. Nevada Bureau of Mines and Geology, University of Nevada Press, Reno, Las Vegas, 519 p.

Castor, S.B., Weiss, S.I., 1992, Contrasting styles of epithermal precious-metal mineralization in the southwestern Nevada volcanic field, USA. Ore Geology Reviews, v. 7, p. 193–223.

Chaffee, M., Sutley, S., Brem, G., Fey, D., Hill, R., 1986, Chemical Analyses and Statistical Summaries for Samples of Rock, Minus-60-Mesh (0.25-mm) Stream Sediment, and Nonmagnetic Heavy-Mineral Concentrate, Sweetwater Roadless Area, Mono County, California, and Lyon and Douglas Counties, Nevada, USGS MF-1535-C.

Chen, J.H., Moore, J.G., 1982, Uranium-lead isotopic ages from the Sierra Nevada Batholith, California, Journal of Geophysical Research: Solid Earth, v. 87, p. 4761–4784.

Ciobanu, C.L., Spry, P.G., Voudouris, P., 2009, Understanding gold-(silver)-telluride-(selenide) mineral deposits, Episodes, v. 32, p. 249–263.

Cline, J., 1986, The Sixteen-to-One epithermal silver-gold deposit, Esmeralda County, Nevada: a wall rock alteration and fluid inclusion study: University of Arizona, M.S. thesis, 113 p.

Cooke, D.R., McPhail, D.C., 2001, Epithermal Au-Ag-Te Mineralization, Acupan, Baguio District, Philippines: Numerical Simulations of Mineral Deposition, Economic Geology, v. 96, p. 109–131.

Dickinson, W.R., 2006, Geotectonic evolution of the Great Basin, Geosphere, v. 2, p. 353–368.

du Bray, E.A., John, D.A., Cousens, B.L., 2014, Petrologic, tectonic, and metallogenic evolution of the southern segment of the ancestral Cascades magmatic arc, California and Nevada, Geosphere, v. 10, p. 1–39.

Eng, T., Boden, D.R., Reischman, M.R., Biggs, J.O., 1996, Geology and mineralization of the Bullfrog Mine and vicinity, Nye County, Nevada, in: Geology and Ore Deposits of the American Cordillera, GSN Symposium Proceedings. p. 353–402.

Eng, T., Thomas, R.D., Taylor, D.T., Robbins, C., 2015, Geology of the Rockland Mine Area, Western Nevada: Au-Ag Mineralization Associated with Late Miocene Rhyolite Domes, in: New Concepts and Discoveries: GSN 2015 Symposium Proceedings.

Faulds, J.E., Hinz, N.H., Coolbaugh, M.F., Cashman, P.H., Kratt, C., Dering, G., Edwards, J., Mayhew, B., Mclachlan, H., 2011, Assessment of Favorable Structural Settings of Geothermal Systems in the Great Basin, Western USA, Geothermal Resources Council Transactions, v. 35, p. 777–783.

Fleck, R.J., Sutter, J.F., Elliot, D.H., 1977, Interpretation of discordant 40Ar/39Ar age-spectra of Mesozoic tholeiites from Antarctica. Geochimica et Cosmochimica Acta, v. 41, p. 15–32.

Gehrels, G.E., Valencia, V.A., Ruiz, J., 2008, Enhanced precision, accuracy, efficiency, and spatial resolution of U-Pb ages by laser ablation-multicollector-inductively coupled plasma-mass spectrometry. Geochemistry, Geophysics, Geosystems, v. 9, p. 1–13.

Haas Jr., J.L., 1971, The effect of salinity on the maximun thermal gradient of a hydrothermal system at hydrostatic pressure, Economic Geology, v. 66, p. 940–946.

Halsey, J.H., 1953, Geology of parts of the Bridgeport, California and Wellington, Nevada quadrangles: University of California, Berkeley, Ph.D. dissertation, 506 p.

Hedenquist, J.W., Lowenstern, J.., 1994, The role of magmas in the formation of hydrothermal ore deposits, Nature, v. 370, p. 519–527.

Hunter, R.D., 1976, Volcanic stratigraphy and structural control of mineralization in the northeastern portion of the Patterson mining district, Mono County, California: University of California, Riverside, M.S. thesis, 142 p.

Hurtig, N.C., Williams-Jones, A.E., 2015, Porphyry-epithermal Au-Ag-Mo ore formation by vapor-like fluids: New insights from geochemical modeling, Geology, v. 43, p. 587–590.

Irelan, W., Whiting, H.A., 1888, Eighth Report of the State Mineralogist, California Journal of Mines and Geology, v. 8, p. 357–363.

John, D.A., 2001, Miocene and Early Pliocene Epithermal Gold-Silver Deposits in the Northern Great Basin, Western United States: Characteristics, Distribution, and Relationship to Magmatism, Economic Geology, v. 96, p. 1827–1853.

John, D.A., Bray, E.A., Blakely, R.J., Fleck, R.J., Vikre, P.G., Box, S.E., Moring, B.C., 2012, Miocene magmatism in the Bodie Hills volcanic field, California and Nevada: A long-lived eruptive center in the southern segment of the ancestral Cascades arc, Geosphere, v. 8, p. 44–97.

John, D.A., du Bray, E.A., Box, S.E., Vikre, P.G., Rytuba, J.J., Fleck, R.J., Moring, B.C., 2015, Geologic Map of the Bodie Hills, California and Nevada: USGS Scientific Investigations Map 3318, 64 p.

Johnson, E.R., Kamenetsky, V.S., McPhie, J., 2013, The Behavior of Metals (Pb, Zn, As, Mo, Cu) During Crystallization and Degassing of Rhyolites from the Okataina

Volcanic Center, Taupo Volcanic Zone, New Zealand. Journal of Petrology, v. 54, p. 1641–1659.

Keith, W., 1977, Geology of the Red Mountain Mining District, Esmeralda County, Nevada, Geological Survey Bulletin 1423, 54 p.

Kowall, C., 1996, The Golden Star Prospect 1995 Highlights, Sweetwater Mountains, Mono County, California, unpublished report, Stuart Resources, 22 p.

Lambeth, R.H., Campbell, H.W., Scott, D.F., 1983, Mineral Investigation of the Sweetwater RARE II Area Mono County California and Lyon and Douglas Counties, Nevada, US Bureau of Mines Open-File Report MLA 69-83, 34 p.

Le Maitre, R.W.B., Dudek, P., Keller, A., Lameyre, J., Le Bas, J., Sabine, M.J., Schmid, P.A., Sorensen, R., Streckeisen, H., Woolley, A., Zanettin, A.R., 1989, A classification of igneous rocks and glossary of terms: Recommendations of the International Union of Geological Sciences, Subcommission on the Systematics of Igneous Rocks, No. 552.3, ed. International Union of Geological Sciences.

Manuszak, J.D., Satterfield, J.I., Gehrels, G.E., 2000, Detrital zircon geochronology of Upper Triassic strata in western Nevada, in: Gehrels, G.E., Soreghan, M.J. (Eds.), Paleozoic and Triassic Paleogeography and Tectonics of Western Nevada and Northern California, Geological Society of America, p. 109–118.

McDougall, I., Harrison, M., 1999, Geochronology and Thermochronology by the ^{40}Ar/^{39}Ar Method: Oxford, Oxford University Press, 269 p.

Moore, J.G., Archbold, N.L., 1969, Geology and Mineral Deposits of Lyon, Douglas, and Ormsby Counties, Nevada, Nevada Bureau of Mines and Geology Bulletin, v. 75, 44 p.

Nelson, C.E., 1987, Gold Deposits in the Hot Spring Environment, in: Vikre, P.G., Schafer, R.W., Cooper, J.W. (Eds.), Bulk Mineable Precious Metal Deposits of the Western United States: Reno, Geological Society of Nevada, p. 417–431.

Princehouse, D.S., Dilles, J.H., 1996, Mesozoic porphyry gold-copper mineralization at the Wheeler Mine, Pine Grove District, Nevada, in: Geology and Ore Deposits of the American Cordillera, Geological Society of Nevada Symposium Proceedings, p. 1533–1556.

Renne, P.R., Deino, A.L., Hames, W.E., Heizler, M.T., Hemming, S.R., Hodges, K. V., Koppers, A.A.P., Mark, D.F., Morgan, L.E., Phillips, D., Singer, B.S., Turrin, B.D., Villa, I.M., Villeneuve, M., Wijbrans, J.R., 2009, Data reporting norms for ^{40}Ar/^{39}Ar geochronology, Quaternary Geochronology, v. 4, p. 346–352.

Richards, J.P., 2009, Postsubduction porphyry Cu-Au and epithermal Au deposits: Products of remelting of subduction-modified lithosphere, Geology, v. 37, p. 247–250.

Rickwood, P.C., 1989, Boundary lines within petrologic diagrams which use oxides of major and minor elements, Lithos, v. 22, p. 247–263.

Robinson, P.T., 1972, Petrology of the Potassic Silver Peak Volcanic Center, Western Nevada, Geological Society of America Bulletin, v. 83, p. 1693–1708.

Roelofs, A.A., Glazner, F., Farmer, G.L., 2004, Tertiary volcanic activity at Sonora Pass, CA: Arc and non-arc magmatism in the central Sierra Nevada, in: AGU Fall Meeting Abstracts.

Roy, R., Majumdar, A.J., Hulbe, C.W., 1959, The Ag_2S and Ag_2Se Transitions as

Geologic Thermometers, Economic Geology, v. 54, p. 1278–1280.

Rye, R.O., 2005, A review of the stable-isotope geochemistry of sulfate minerals in selected igneous environments and related hydrothermal systems, Chemical Geology, v. 215, p. 5–36.

Schweickert, R.A., 1976, Early Mesozoic rifting and fragmentation of the Cordilleran orogen in the western USA, Nature, v. 260, p. 586–591.

Simmons, S.F., Christenson, B.W., 1994, Origins of Calcite in a Boiling Geothermal System, American Journal of Science, v. 294, p. 361–400.

Simmons, S.F., White, N.C., John, D.A., 2005, Geological characteristics of epithermal precious and base metal deposits, in: Hedenquist, J.W., Thompson, J.F.H., Goldfarb, R.J., Richards, J.P. (Eds.), Economic Geology One Hundredth Anniversary Volume: 1905-2005: Society of Economic Geologists, p. 485–522.

Stewart, B.J.H., Kelleher, P.C., Zorich, E.A., 1984, Geologic Map of the Monte Cristo Range Area, Esmeralda and Mineral Counties, Nevada, USGS MF-2260, 16 p.

Vikre, P.G., Henry, C.D., 2010, Quartz-alunite alteration cells in the southern segment of the Ancestral Cascades Magmatic Arc, in: Great Basin Evolution and Metallogeny: 2010 Symposium Proceedings, p. 701–745.

Vikre, P.G., John, D.A., Du Bray, E.A., Fleck, R.J., 2015, Gold-Silver Mining Districts, Alteration Zones, and Paleolandforms in the Miocene Bodie Hills Volcanic Field, California and Nevada: USGS Scientific Investigations Report 2015–5012, 160 p.

Vikre, P.G., McKee, E.H., 1994, Geology, Alteration, and Geochronology of the Como District, Lyon County, Nevada, Economic Geology, v. 89, p. 639–646.

Walker, J.D., Glazner, A.F., Farmer, G.L., Carlson, R.W., Ferrari, L., 2014, The Western North American Volcanic and Intrusive Database.

Winter, J.D., 2009, Principles of Igneous and Metamorphic Petrology, 2nd ed.: Pearson.

Yang, K., Yang, K., Huntington, J.F., Boardman, J.W., Mason, P., 2001, Mapping hydrothermal alteration in the Comstock mining district, Nevada, using simulated satellite borne hyperspectral data mapping, Australian Journal of Earth Science, v. 46, p. 915–922.

Appendix A- Whole rock geochemistry of unaltered rocks

Sample	RSW002A	RSW003	RSW020	RSW026	RSW027	RSW032	RSW061	RSW065	RSW066	RSW076
Unit	Tu dome	Trg	Jqm	Tra	Td	Td	Tab	Tab	Tab	Td2
Easting (NAD83)	306892	305845	303324	303255	304346	302501	298947	299933	300008	302731
Northing (NAD83)	4263331	4265581	4258351	4260963	4261430	4259531	4255416	4254542	4254628	4258633
Al2O3 (%)	12.95	12.7	14.95	12.82	16.27	15.6	17.54	16.42	18.08	15.03
BaO (%)	0.02	0.02	0.12	0.02	0.15	0.15	0.17	0.12	0.24	0.11
CaO (%)	0.59	0.45	2.59	0.38	1.94	1.72	5.28	5.88	7.13	3.03
Cr2O3 (%)	<0.01	<0.01	<0.01	<0.01	<0.01	<0.01	0.01	0.01	0.01	0.01
Fe2O3 (%)	1.06	1.01	3.85	0.74	2.96	2.36	6.82	6.97	6.3	4.45
K2O (%)	4.57	4.66	4.44	4.75	4.11	5.38	2.77	1.44	2.93	3.95
MgO (%)	0.11	0.05	1.34	0.09	0.53	0.5	1.12	3.13	2.45	1.74
MnO (%)	0.06	0.04	0.08	0.03	0.04	0.09	0.08	0.17	0.14	0.09
Na2O (%)	4.06	4.05	3.3	3.51	3.83	3.24	3.46	4.24	3.52	3.67
P2O5 (%)	0.02	0.01	0.16	0.01	0.2	0.19	0.32	0.35	0.53	0.39
SiO2 (%)	73	75.8	67.5	76.52	67.48	68.42	57.58	55.91	52.53	64.94
SrO (%)	0.01	0.01	0.04	0.02	0.06	0.04	0.09	0.11	0.14	0.07
TiO2 (%)	0.13	0.11	0.46	0.13	0.49	0.36	1.04	0.91	0.85	0.88
LOI (%)	2.16	0.2	0.61	0.57	1.09	1.44	3.95	4.49	4.35	1.13
Ba(ppm)	90.6	65	1025	34.5	1360	1370	1495	1060	2220	900
Ce(ppm)	56.9	50.5	47.3	62.6	84.6	85	59.2	71.4	88.3	81.5
Cr(ppm)	10	10	30	<10	10	10	20	80	20	30
Cs(ppm)	7.09	7.09	4.33	4.45	3.38	5.12	2.35	3.09	13	2.29
Dy(ppm)	0.81	0.66	3.03	1	3	2.55	3.18	4.77	3.54	2.91
Er(ppm)	0.62	0.62	1.92	0.88	1.6	1.63	1.54	2.6	1.87	1.55
Eu(ppm)	0.17	0.12	0.8	0.15	1.33	1.04	1.31	2.05	1.94	1.19
Ga(ppm)	17	17.4	14.4	17.2	19.1	19.2	20.1	19.6	21.5	17.4
Gd(ppm)	0.87	0.57	3.36	0.83	3.84	3.58	4.36	6.68	5.51	3.71
Ge(ppm)	-	-	-	<5	<5	<5	<5	<5	<5	<5
Hf(ppm)	5	4.3	5.9	4.7	6	6.6	4.5	5.6	5.1	5.1
Ho(ppm)	0.18	0.17	0.66	0.26	0.59	0.54	0.6	1.03	0.71	0.55
La(ppm)	44.3	39.5	24.5	43.5	46.5	49	30.6	40.1	43.6	46.1
Lu(ppm)	0.17	0.19	0.32	0.24	0.31	0.28	0.23	0.35	0.27	0.24
Nb(ppm)	22.7	27.3	9.2	28.2	17.6	19.1	7.6	8.6	8.7	25.3
Nd(ppm)	9.9	8	19.5	11.2	32.6	30.3	30.5	42.8	41.8	30.9
Pr(ppm)	4.17	3.53	5.22	4.74	9.37	8.94	7.72	10.2	10.65	8.79
Rb(ppm)	173	197.5	161.5	200	124	164	59.5	34.2	97.3	112
Sm(ppm)	1.13	0.89	3.79	1.12	5.69	5.01	5.79	7.97	7.61	4.84
Sn(ppm)	1	2	1	2	1	2	1	1	1	1
Sr(ppm)	45.8	31.8	343	18	439	361	667	990	1210	502
Ta(ppm)	1.4	1.8	0.8	1.9	1.1	1.4	0.5	0.5	0.5	1.7
Tb(ppm)	0.12	0.09	0.5	0.16	0.52	0.51	0.56	0.88	0.69	0.53
Th(ppm)	23.7	26.9	20.7	25.5	13.05	17.15	6.72	8.89	8.49	14.35
Tm(ppm)	0.11	0.12	0.3	0.18	0.29	0.22	0.23	0.38	0.27	0.23
U(ppm)	7.78	8.1	4.72	7.14	4.72	4.89	2.44	2.95	3.07	4.18
V(ppm)	6	<5	68	<5	50	28	176	149	170	67
W(ppm)	3	3	2	92	43	4	28	2	9	7
Y(ppm)	6.2	5.9	17.2	8.6	15.7	15.6	15.7	26.4	17.4	15
Yb(ppm)	0.88	1.03	1.77	1.49	1.81	1.67	1.51	2.22	1.58	1.71
Zr(ppm)	152	117	228	112	232	251	167	205	208	205
Ag(ppm)	<0.5	<0.5	<0.5	<0.5	1.2	<0.5	<0.5	<0.5	<0.5	<0.5

Table A1. Multi-element geochemistry of unaltered and least altered rocks. See text for unit descriptions. Coordinates are given in NAD 83, Zone 11N.

Sample	RSW161	RSW163	RSW165	RSW178	RSW218	RSW238-6	RSW260	RSW-SC-10	RSWJM006	RSWTri
Unit	Tab	Tre	Td1	Trc	Td3	Trb	Jqm	Trb	Tac	Tri
Easting (NAD83)	298909	299136	299676	304382	304791	303936	303624	304402	300715	302225
Northing (NAD83)	4255473	4254661	4254402	4259269	4253943	4253295	4258059	4254511	4271808	4259702
Al2O3 (%)	18.26	14.25	13.59	12.3	14.95	14.16	15.12	14.48	17.9	12.68
BaO (%)	0.16	0.18	0.23	0.02	0.2	0.16	0.12	0.17	0.2	0.13
CaO (%)	5.88	0.95	2.38	0.17	0.09	0.82	2.63	1.01	6.07	0.44
Cr2O3 (%)	0.01	<0.01	<0.01	<0.01	<0.01	<0.01	<0.01	<0.01	<0.01	<0.01
Fe2O3 (%)	5.93	1.41	1.15	0.38	2.19	1.72	3.91	2.04	6.34	1.36
K2O (%)	2.81	5.12	4.92	3.64	9.7	5.09	4.51	4.62	3.65	4.2
MgO (%)	1.48	0.27	0.25	0.04	0.26	0.26	1.41	0.32	2.33	0.35
MnO (%)	0.08	0.05	0.04	0.01	0.01	0.03	0.09	0.08	0.12	0.01
Na2O (%)	4.45	4.1	0.98	2.06	0.65	3.46	3.39	3.71	4.08	1.38
P2O5 (%)	0.35	0.05	0.03	0.03	0.1	0.02	0.16	0.03	0.33	0.04
SiO2 (%)	58.4	72.36	70.81	79.08	68.44	73.42	67.52	72.1	57.4	76.63
SrO (%)	0.12	0.04	0.11	0.01	0.02	0.02	0.04	0.04	0.13	0.02
TiO2 (%)	0.88	0.23	0.18	0.12	0.8	0.26	0.48	0.3	0.92	0.29
LOI (%)	1.21	0.21	5.1	2.12	1.59	0.73	0.71	0.83	0.45	1.92
Ba(ppm)	1440	1575	2170	54.7	1800	1395	1030	1490	1710	1115
Ce(ppm)	53.8	76.1	56.4	45	72	78.2	53.5	62.8	92.1	67
Cr(ppm)	10	<10	<10	<10	10	10	30	<10	10	<10
Cs(ppm)	1.73	2.14	153	3.88	13.65	8.94	4.78	4.09	1.2	5.01
Dy(ppm)	2.83	2.41	1.71	0.53	2.07	2.3	3.4	2.13	4.37	1.79
Er(ppm)	1.38	1.44	0.9	0.39	1.33	1.38	2.07	1.28	2.47	1.11
Eu(ppm)	1.35	0.78	0.61	0.15	1.37	0.87	0.92	0.78	1.74	0.73
Ga(ppm)	21.4	16.7	15.7	17	19.6	17	16.2	17.4	19.5	14
Gd(ppm)	3.88	2.81	2.18	0.7	2.42	2.94	3.94	2.67	5.84	2.22
Ge(ppm)	<5	<5	<5	<5	<5	<5	<5	<5	-	<5
Hf(ppm)	4.2	5.1	4.2	4.5	9.8	5.8	5.9	6	7.3	5.7
Ho(ppm)	0.56	0.52	0.32	0.1	0.44	0.47	0.74	0.42	0.87	0.37
La(ppm)	27.4	42.1	32.6	39.1	37.1	46.3	27.7	37	43.9	41.3
Lu(ppm)	0.2	0.26	0.16	0.15	0.25	0.24	0.35	0.21	0.34	0.22
Nb(ppm)	6.9	16.8	11.4	29.4	18	14.7	9.9	14	16.3	15.3
Nd(ppm)	26.8	26.6	20.4	6.5	26.6	29.7	23.4	25.5	42	24.3
Pr(ppm)	6.68	8.08	5.96	3	7.64	8.65	6.23	7.21	10.95	7.24
Rb(ppm)	60.2	141.5	386	161.5	637	143.5	176	128.5	54.8	123.5
Sm(ppm)	5.36	4.01	3.04	0.77	4.43	4.44	4.76	4.03	7.43	3.56
Sn(ppm)	1	1	1	1	2	1	2	1	1	1
Sr(ppm)	941	230	1000	23.9	169	204	337	320	1060	162.5
Ta(ppm)	0.4	1.2	0.9	1.6	1.1	1.1	0.8	1.1	1.1	1.2
Tb(ppm)	0.54	0.46	0.31	0.1	0.35	0.42	0.6	0.38	0.8	0.34
Th(ppm)	5.48	14.3	14.4	25.2	27.3	14.1	22.4	14.9	6.41	13.75
Tm(ppm)	0.22	0.24	0.16	0.1	0.21	0.21	0.31	0.19	0.35	0.17
U(ppm)	1.8	4.39	4.45	4.99	9.51	4.3	4.75	4.2	2.04	4.32
V(ppm)	163	12	11	<5	67	14	70	19	164	19
W(ppm)	5	5	2	1	21	4	2	7	1	4
Y(ppm)	14.3	13.7	9.9	4.1	11.7	13.4	21.4	12.4	21.8	10.9
Yb(ppm)	1.37	1.65	1	0.73	1.5	1.35	2.17	1.32	2.21	1.35
Zr(ppm)	157	186	139	107	376	208	216	215	328	213
Ag(ppm)	<0.5	<0.5	<0.5	<0.5	<0.5	<0.5	<0.5	1.4	<0.5	<0.5

Table A1 continued. Multi-element geochemistry of unaltered and least altered rocks. See text for unit descriptions. Coordinates are given in NAD 83, Zone 11N.

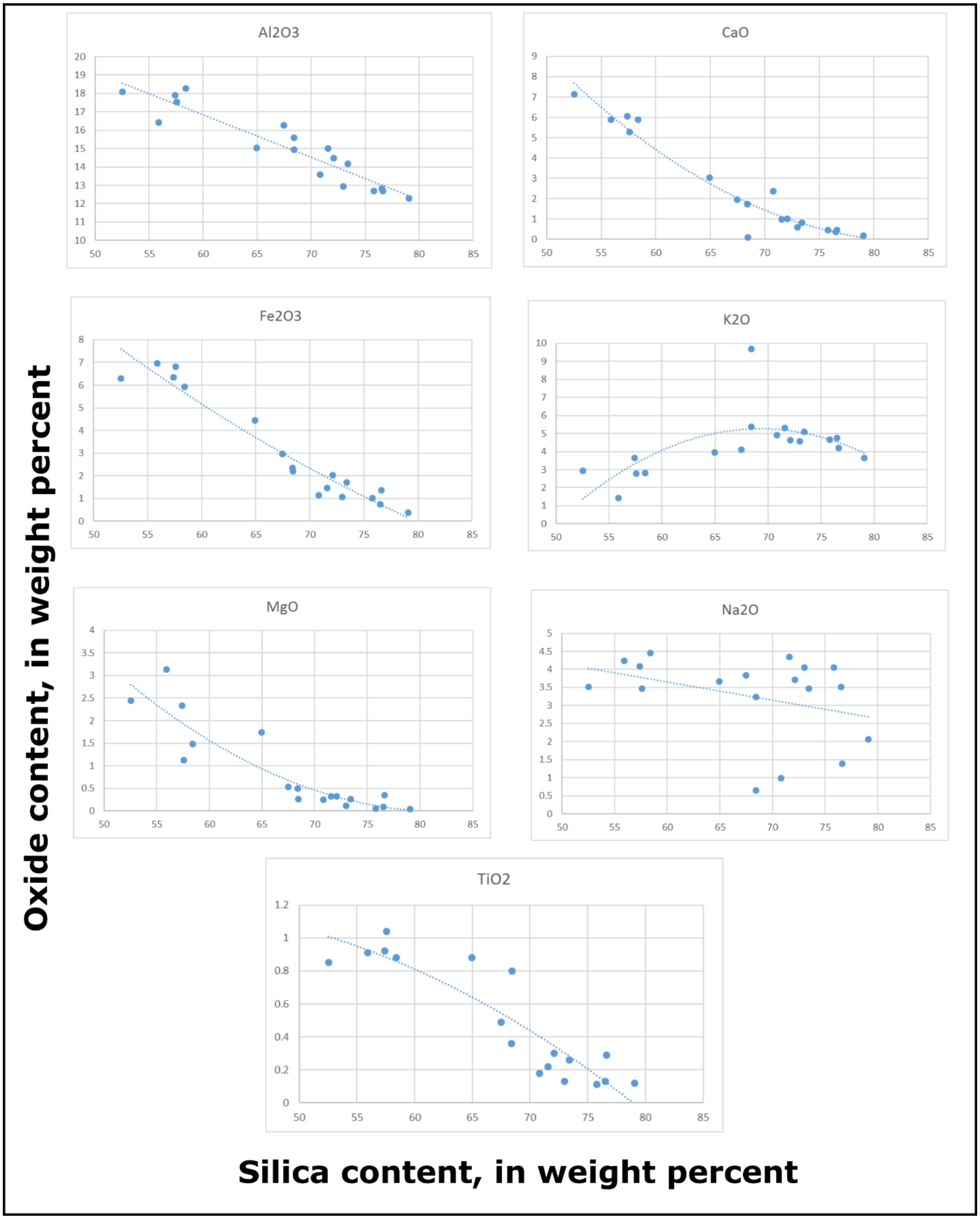

Figure A1. Harker diagrams showing oxide contents vs. silica contents for unaltered and least altered volcanic rocks. Some volcanic rocks show a loss in Na and others show a loss in K.

Appendix B. $^{40}Ar/^{39}Ar$ dating diagrams

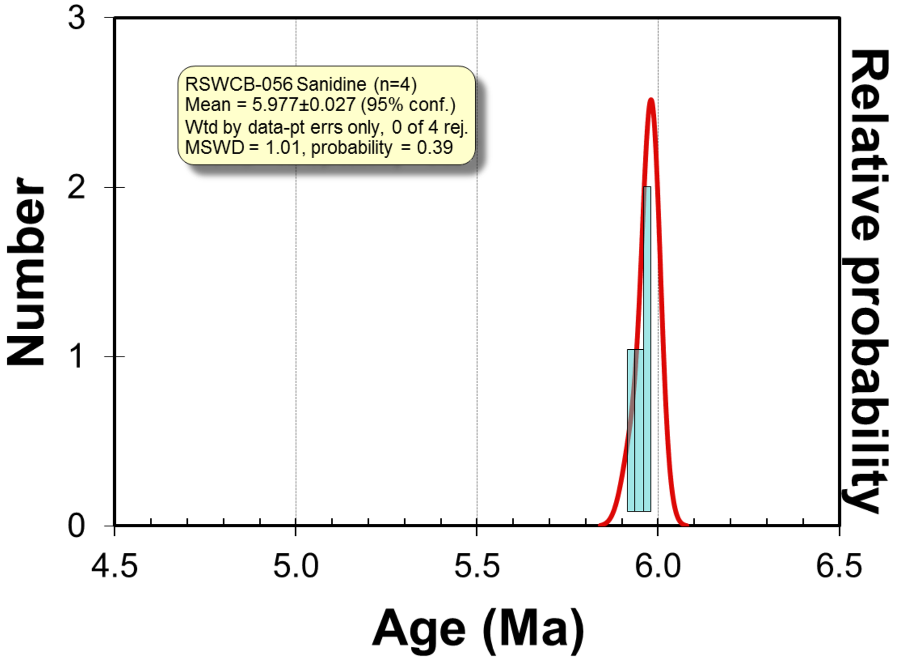

Figure B-1. Relative probability age (5.98 ± 0.03 Ma) for single crystal total fusion dates of sanidine separated from sample RSWCB-056 (porphyritic trachydacite, unit Td).

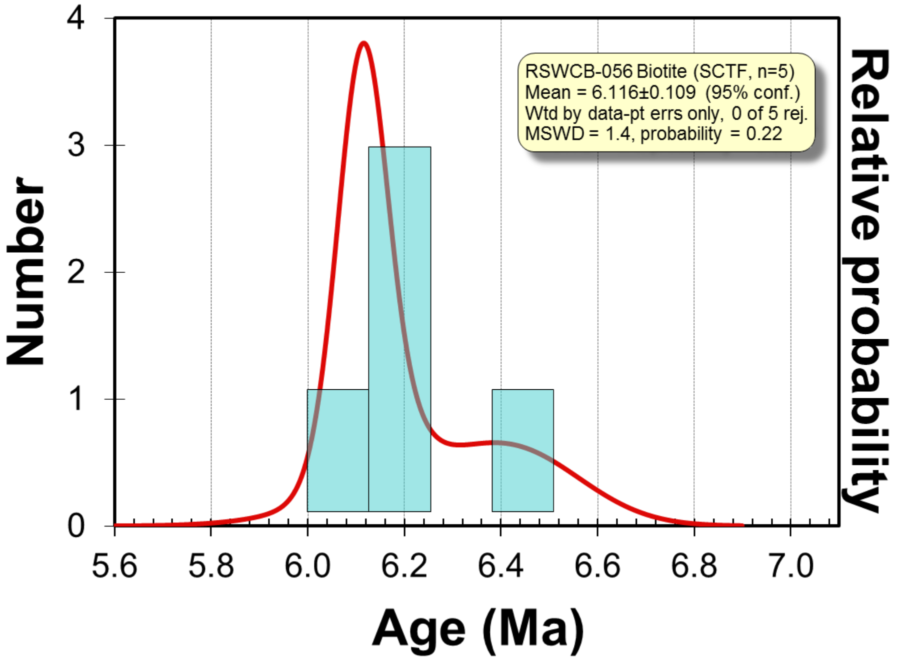

Figure B-2. Relative probability age (6.12 ± 0.11 Ma) for single crystal total fusion dates of biotite separated from sample RSWCB-056 (porphyritic trachydacite, unit Td).

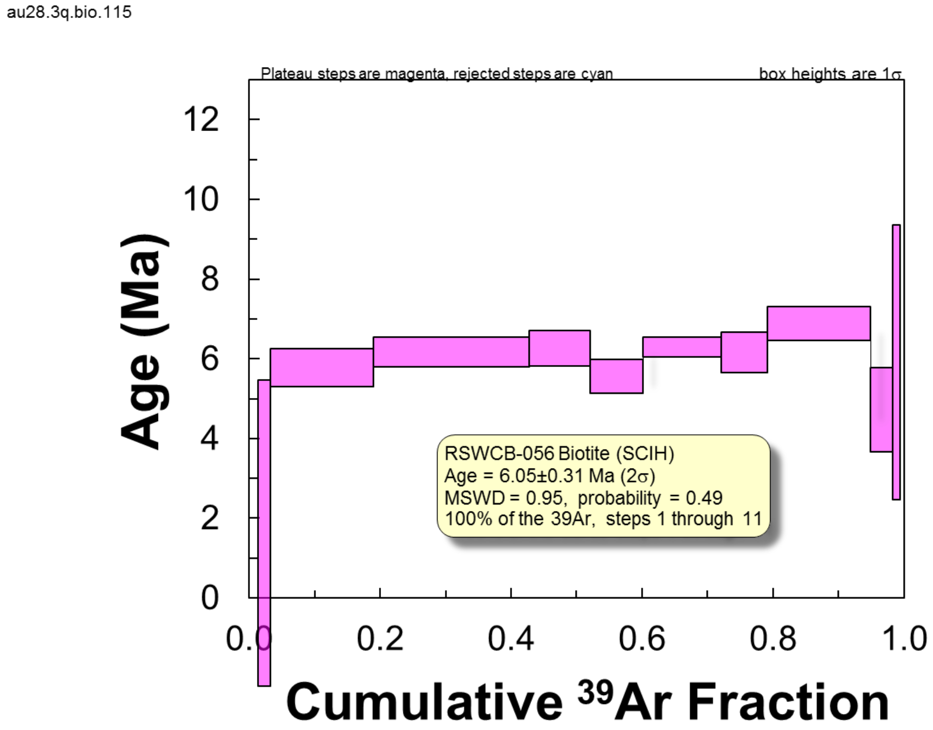

Figure B-3. Plateau age (6.05 ± 0.31 Ma) for single crystal incremental heating of biotite separated from sample RSWCB-056 (porphyritic trachydacite, unit Td).

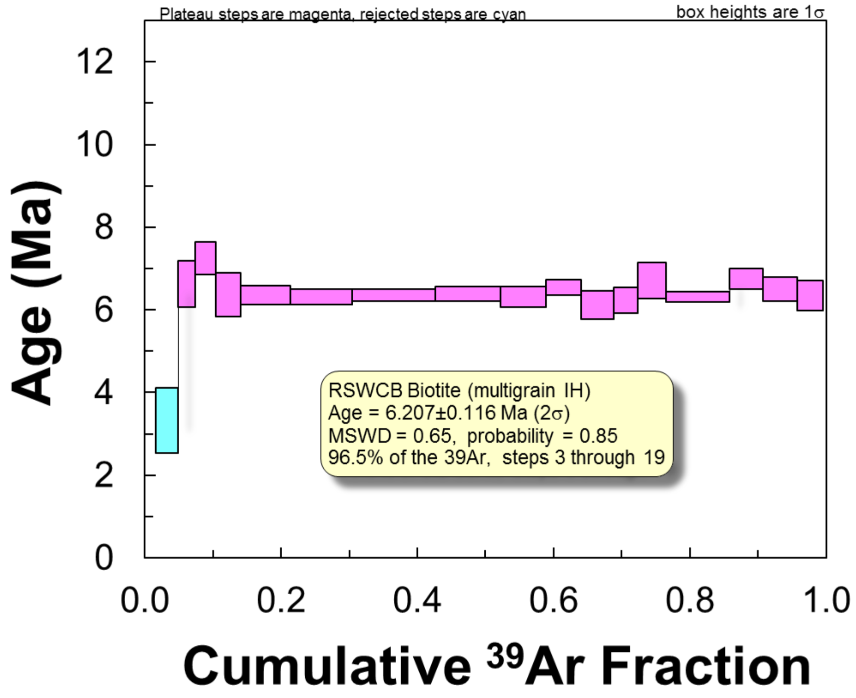

Figure B-4. Plateau age (6.21 ± 0.12 Ma) for multigrain incremental heating of biotite separated from sample RSWCB-056 (porphyritic trachydacite, unit Td). Rejected step for age calculation is shown in cyan.

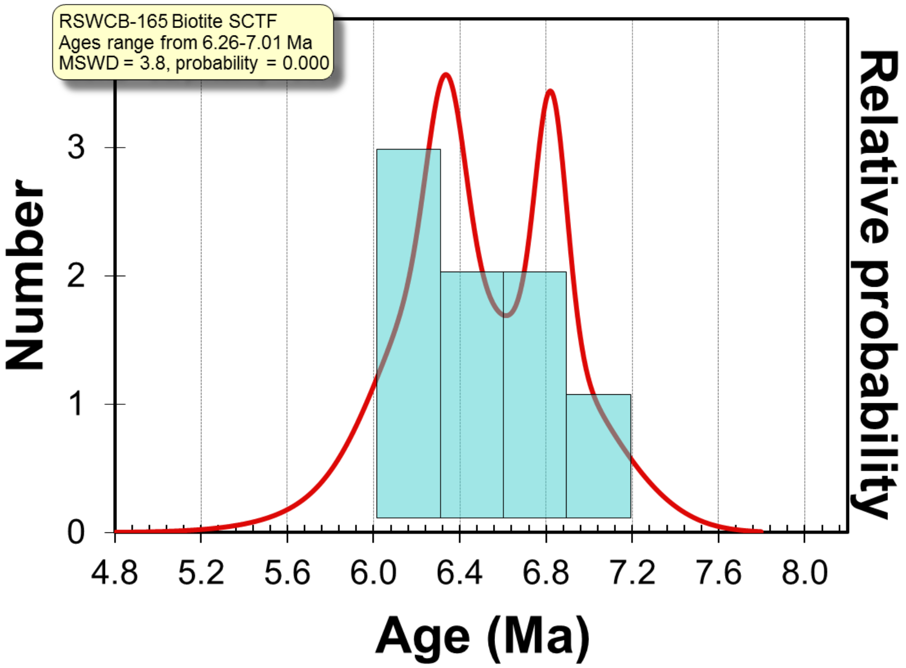

Figure B-5. Relative probability age (ranging from 6.26-7.01 Ma) for single crystal total fusion dates of biotite separated from sample RSWCB-165 (glassy dacite, unit Td1).

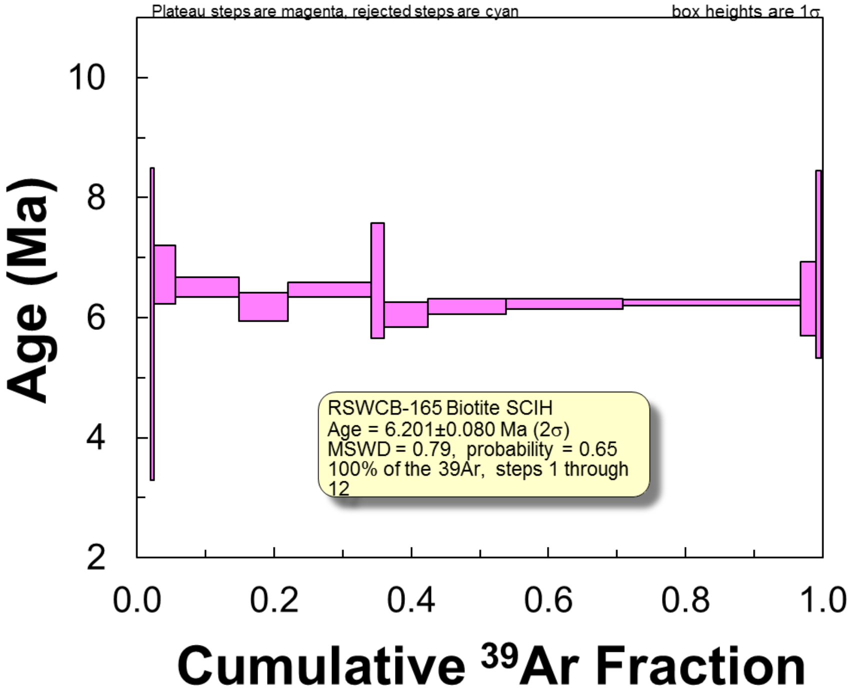

Figure B-6. Plateau age (6.20 ± 0.80 Ma) for single crystal incremental heating of biotite separated from sample RSWCB-165 (glassy dacite, unit Td1).

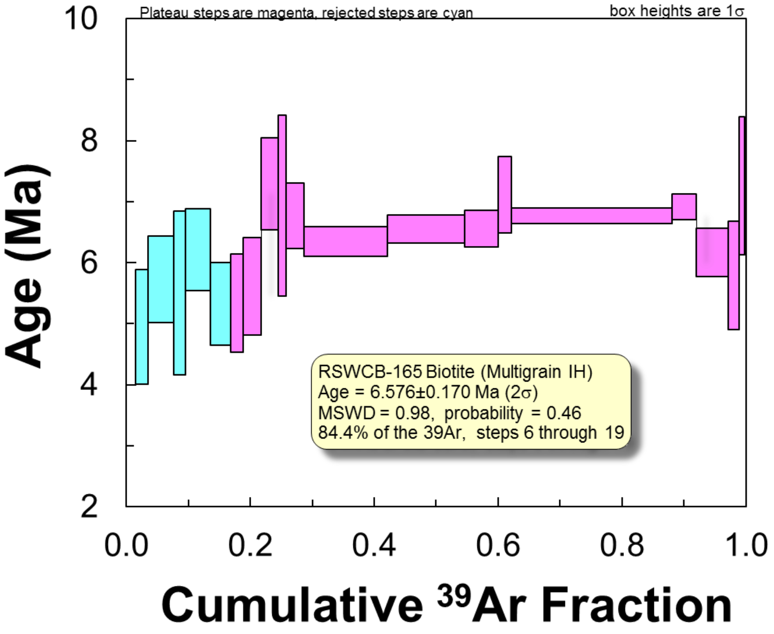

Figure B-7. Plateau age (6.58 ± 0.17 Ma) for multigrain incremental heating of biotite separated from sample RSWCB-165 (glassy dacite, unit Td1). Rejected steps for age calculation are shown in cyan.

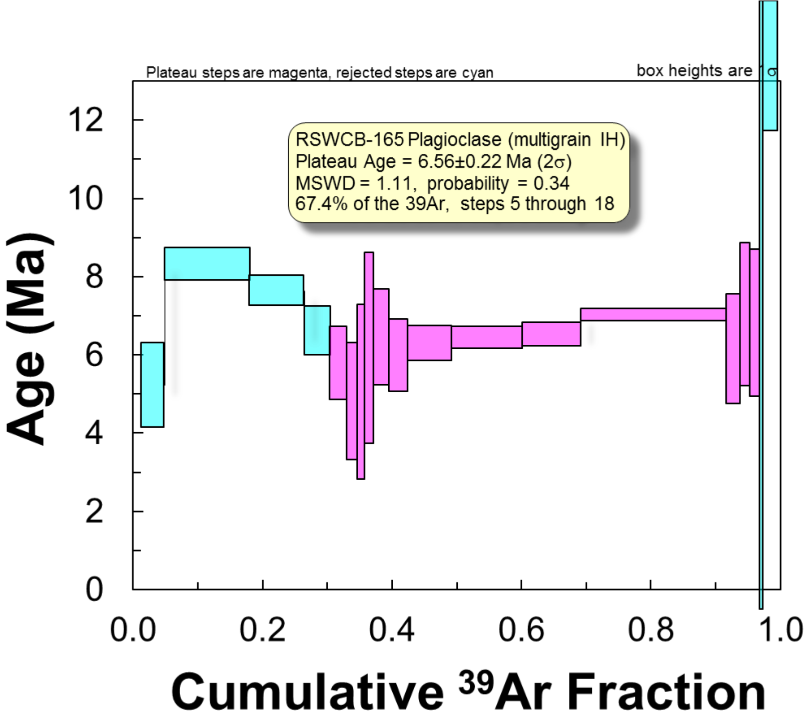

Figure B-8. Plateau age (6.56 ± 0.22 Ma) for multigrain incremental heating of plagioclase separated from sample RSWCB-165 (glassy dacite, unit Td1). Rejected steps for age calculation are shown in cyan.

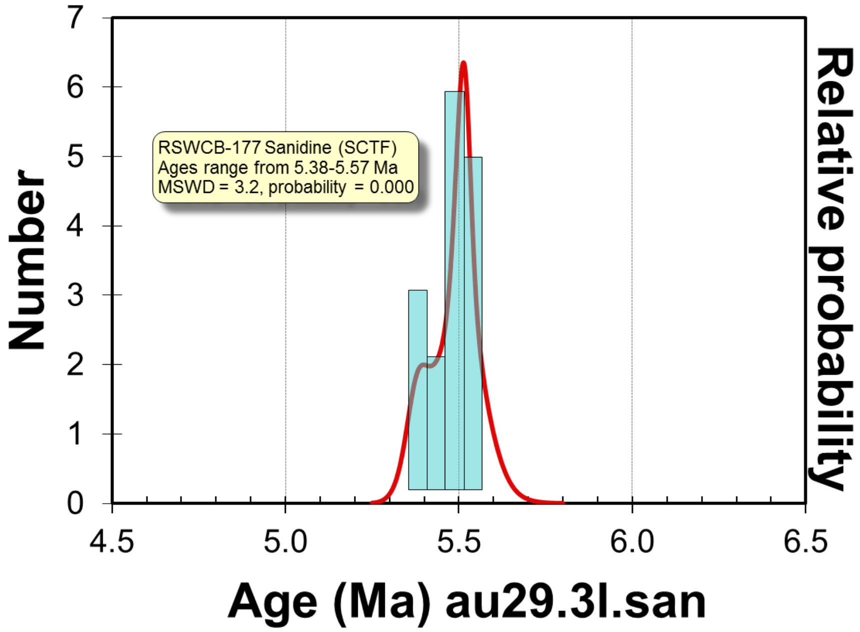

Figure B-9. Relative probability ages (5.38-5.57 Ma) for single crystal total fusion dates of sanidine separated from sample RSWCB-177 (flow-banded porphyritic rhyolite, unit Trc).

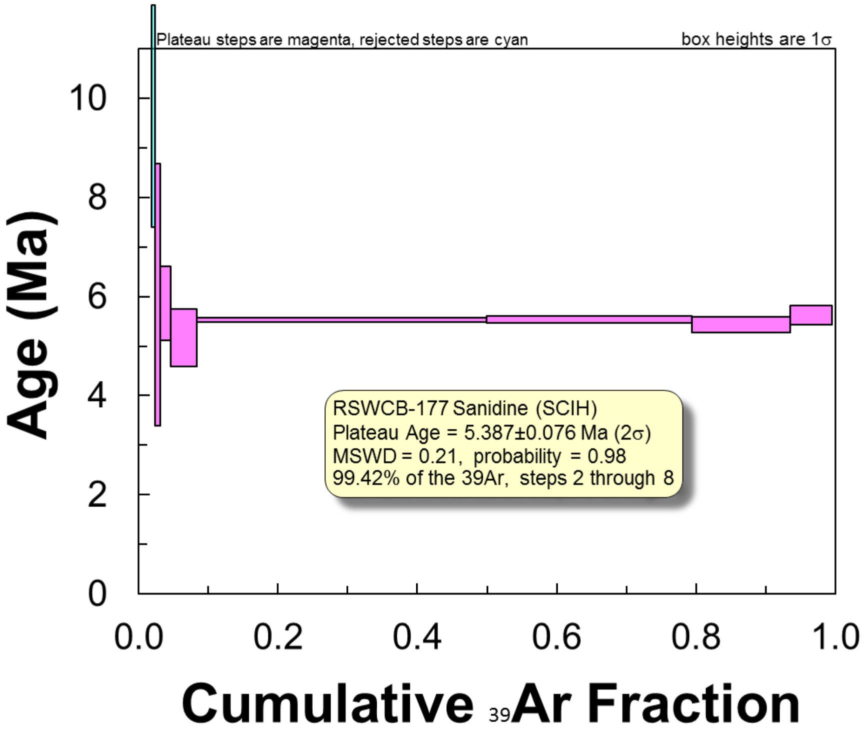

Figure B-10. Plateau age (5.39 ± 0.08 Ma) for single crystal incremental heating of sanidine separated from sample RSWCB-177 (flow-banded porphyritic rhyolite, unit Trc). Rejected step for age calculation is shown in cyan.

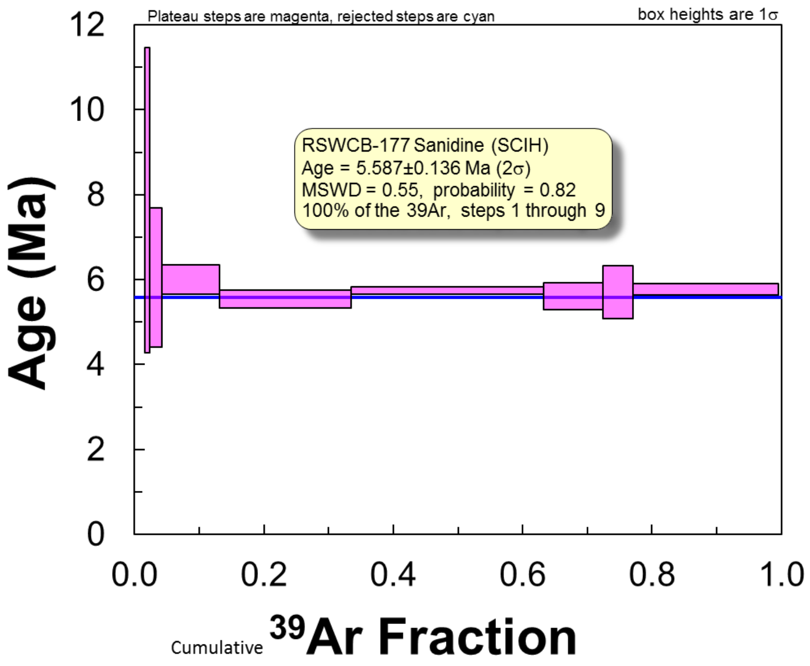

Figure B-11. Plateau age (5.59 ± 0.14 Ma) for single crystal incremental heating of sanidine separated from sample RSWCB-177 (flow-banded porphyritic rhyolite, unit Trc).

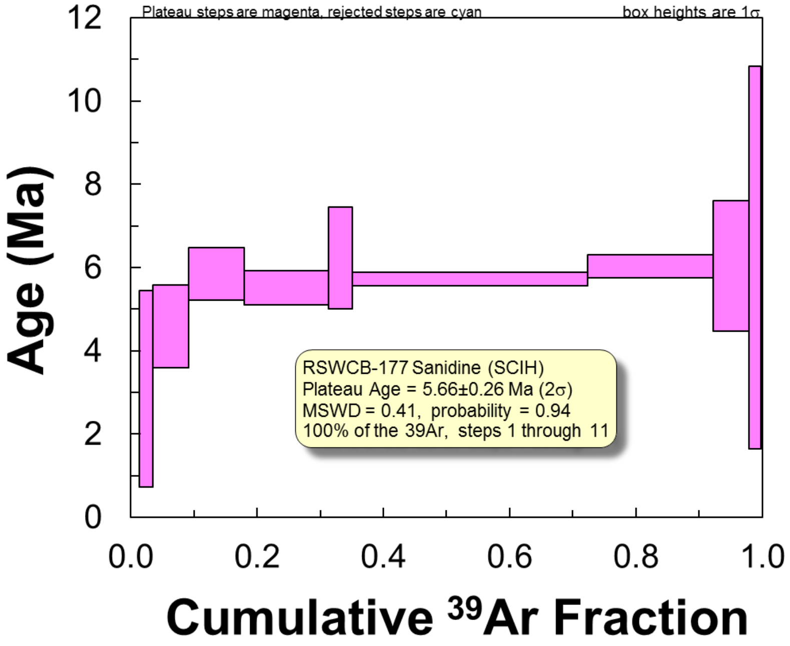

Figure B-12. Plateau age (5.66 ± 0.26 Ma) for single crystal incremental heating of sanidine separated from sample RSWCB-177 (flow-banded porphyritic rhyolite, unit Trc).

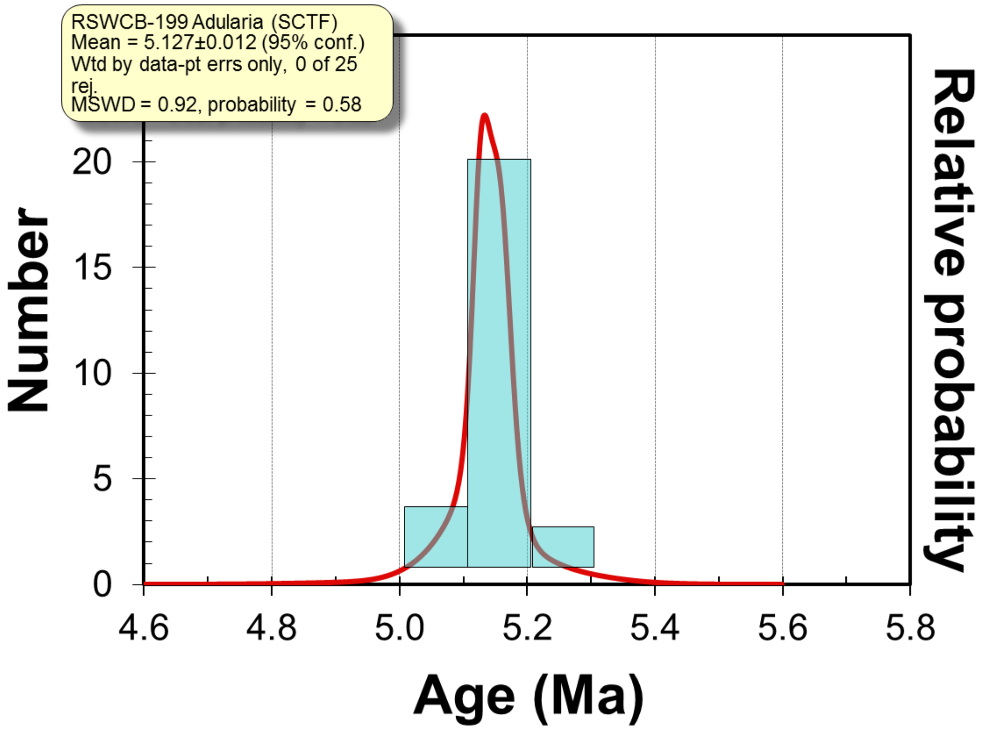

Figure B-13. Relative probability age (5.13 ± 0.01 Ma) for single crystal total fusion dates of adularia separated from sample RSWCB-199 (dump sample from the Silverado mine).

Appendix C. U-Pb zircon analyses

RSW-260	ISOTOPE RATIOS (All values are internal and standard error propagated at 2 se)									
Analysis #	207/235	2se	206/238	2se	ErrorCorrel_6_38vs7_35	238/206	2se	207/206	2se	ErrorCorrel_38_6vs7_6
Output_1_1	0.1766	0.008	0.02615	0.00056	0.14129	38.24092	0.818926	0.049	0.002	0.33119
Output_1_2	0.1823	0.0068	0.02647	0.00046	0.42131	37.77862	0.656523	0.05018	0.0014	0.14427
Output_1_3	0.1963	0.0086	0.02608	0.00077	0.001	38.34356	1.132076	0.0549	0.0029	0.56114
Output_1_4	0.1999	0.0079	0.02561	0.00058	0.3612	39.04725	0.8843188	0.0564	0.0017	0.20274
Output_1_5	0.1753	0.0077	0.02617	0.00056	0.001	38.21169	0.8176747	0.0482	0.0024	0.85605
Output_1_6	0.1789	0.009	0.02606	0.00047	0.001	38.37299	0.6920684	0.0495	0.0023	0.31726
Output_1_7	0.187	0.0092	0.02595	0.00065	0.69468	38.53565	0.9652474	0.0526	0.0022	-0.32241
Output_1_8	0.181	0.0081	0.0275	0.00057	0.05189	36.36364	0.753719	0.0483	0.002	0.4397
Output_1_9	0.1791	0.0066	0.02625	0.0005	0.16088	38.09524	0.7256236	0.0495	0.0017	0.58688
Output_1_10	0.1842	0.0093	0.02616	0.00053	0.3186	38.2263	0.7744625	0.0518	0.0022	0.11729
Output_1_11	0.1749	0.0095	0.02564	0.00065	0.25595	39.00156	0.9887291	0.0499	0.0024	0.16435
Output_1_12	0.1796	0.0084	0.02611	0.00067	0.1399	38.2995	0.9827907	0.0507	0.002	0.43719
Output_1_13	0.1808	0.0098	0.02669	0.00064	0.68345	37.46722	0.8984271	0.05	0.0019	-0.025813
Output_1_14	0.1773	0.0088	0.02642	0.00067	0.16255	37.85011	0.9598628	0.0498	0.0022	0.33077
Output_1_15	0.1763	0.0088	0.02595	0.00057	0.36357	38.53565	0.8464477	0.0502	0.0024	0.070612
Output_1_16	0.1799	0.0079	0.02619	0.00058	0.40316	38.18251	0.8455845	0.0497	0.0017	0.1229
Output_1_17	0.176	0.011	0.02505	0.00052	0.24262	39.92016	0.828682	0.0505	0.003	0.20536
Output_1_18	0.1747	0.0092	0.02578	0.00056	0.001	38.78976	0.8426014	0.0491	0.0027	0.6025
Output_1_19	0.1766	0.0084	0.02598	0.00062	0.14084	38.49115	0.9185724	0.0493	0.0025	0.38536

RSW-260	AGE (in Ma) internal and standard propagated						Approximate Elemental Concentrations							
Analysis #	207/235 Age	2se	206/238 Age	2se	207/206 Age	2se	Approx_U_PPM	2se	Approx_Th_PPM	2se	Approx_Pb_PPM	2se	FInal_U_Th_Ratio	2se
Output_1_1	165	6.9	166.4	3.5	165	88	953	22	393	11	5.33	0.19	2.464	0.029
Output_1_2	170	5.8	168.4	2.9	201	66	1040	25	546	16	7.89	0.25	1.918	0.036
Output_1_3	183.6	8.5	166	4.8	390	120	413.7	9.2	203	5.6	2.86	0.14	2.057	0.033
Output_1_4	185	6.7	163	3.7	467	67	910	60	428	17	6.35	0.38	2.118	0.069
Output_1_5	164	6.7	166.5	3.5	113	110	1668	68	1100	68	15	1.1	1.519	0.048
Output_1_6	167.1	7.8	165.8	2.9	167	100	791	24	418	12	5.77	0.3	1.901	0.027
Output_1_7	174	7.8	165.1	4.1	301	98	938	57	521	36	7.75	0.37	1.82	0.03
Output_1_8	168.9	7	174.9	3.6	118	90	1223	88	444	37	6.4	0.46	2.755	0.039
Output_1_9	167.3	5.7	167	3.1	170	81	1240	62	527	26	7.63	0.42	2.355	0.024
Output_1_10	171.6	8	166.5	3.3	266	96	592	30	256	11	3.7	0.16	2.25	0.054
Output_1_11	163.6	8.2	163.2	4.1	187	110	512	16	167.7	5.5	2.44	0.11	2.995	0.046
Output_1_12	167.6	7.2	166.1	4.2	221	91	875	23	341	12	5.02	0.21	2.495	0.045
Output_1_13	168.6	8.4	169.8	4	194	86	1415	55	563	20	8.42	0.29	2.438	0.052
Output_1_14	165.7	7.6	168.1	4.2	179	97	762	37	305	14	4.52	0.25	2.428	0.037
Output_1_15	164.8	7.6	165.1	3.6	197	100	979	36	421	16	6.16	0.28	2.273	0.039
Output_1_16	167.9	6.8	166.7	3.7	179	79	1047	28	436	11	6.27	0.16	2.329	0.036
Output_1_17	164.4	9.8	159.5	3.2	210	130	380	13	133.1	3	2.03	0.12	2.742	0.063
Output_1_18	163.4	7.9	164.1	3.5	150	120	1370	150	698	89	9.7	1.3	1.946	0.046
Output_1_19	165	7.3	165.3	3.9	158	110	709	45	287	21	4.25	0.33	2.414	0.044

Table C-1. Data from U-Pb dating of zircons in sample RSW-260 (quartz monzonite).

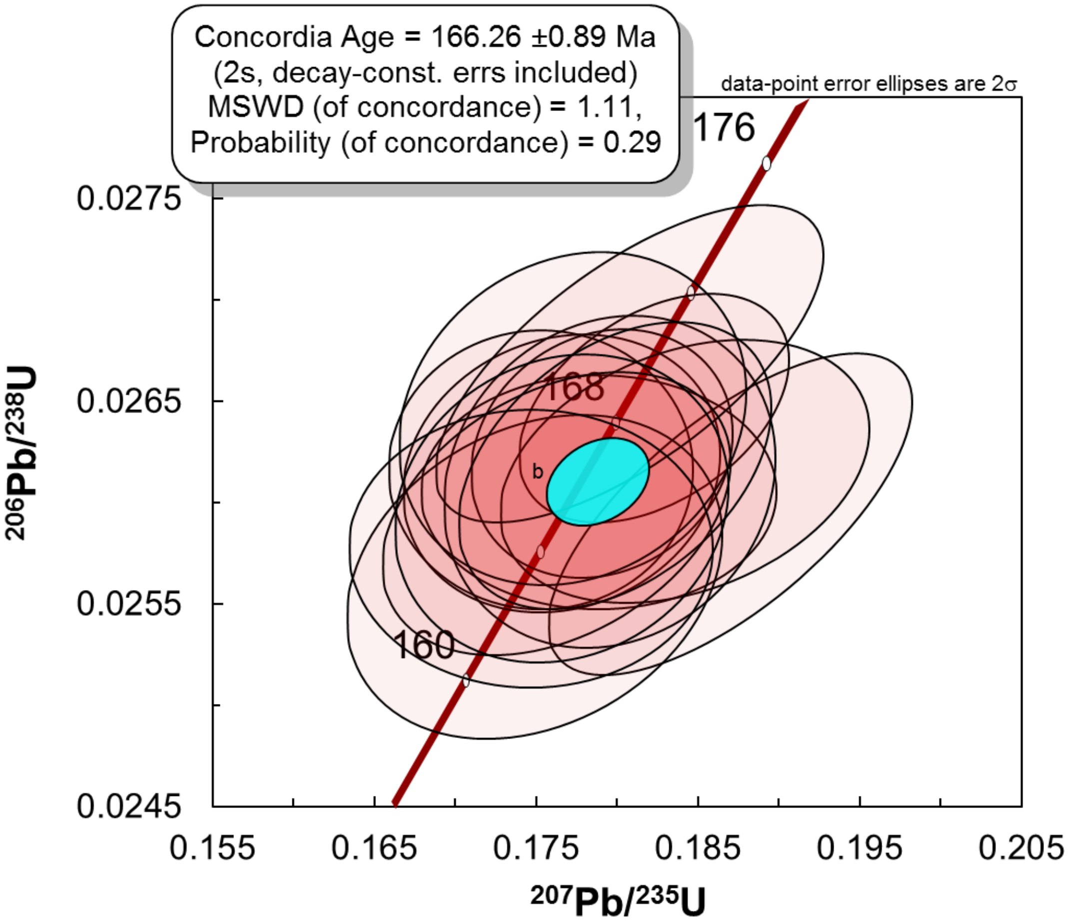

Figure C-1. Concordia diagram ^{206}Pb/^{238}U- ^{207}Pb/^{235}U for zircons in sample RSW-260 (quartz monzonite). The Concordia age is 166.26 ± 0.89 Ma.

RSWCB-261	ISOTOPE RATIOS (All values are internal and standard error propagated at 2 se)									
Analysis #	207/235	2se	206/238	2se	ErrorCorrel_6_38vs7_35	238/206	2se	207/206	2se	ErrorCorrel_38_6vs7_6
Output_1_1	0.0087	0.0053	0.001	0.00011	0.050658	1000	110	0.066	0.043	-0.13813
Output_1_2	0.0103	0.0035	0.000928	0.000076	0.01861	1077.586	88.25059	0.091	0.033	0.2748
Output_1_3	0.0061	0.0036	0.000899	0.000073	0.001	1112.347	90.32407	0.055	0.034	0.28228
Output_1_4	0.0043	0.0084	0.00075	0.00011	0.01009	1333.333	195.5556	0.037	0.072	-0.16612
Output_1_5	0.0056	0.0045	0.00091	0.0001	0.001	1098.901	120.7584	0.062	0.043	0.18824
Output_1_6	0.0103	0.0053	0.000884	0.000085	0.001	1131.222	108.7713	0.068	0.047	0.48009
Output_1_7	0.0309	0.0091	0.00096	0.00015	0.001	1041.667	162.7604	0.21	0.11	0.52976
Output_1_8	0.0085	0.0038	0.000933	0.000076	0.001	1071.811	87.30725	0.079	0.037	0.29436
Output_1_9	0.0041	0.0054	0.000918	0.000083	0.026794	1089.325	98.49013	0.044	0.041	0.080819
Output_1_10	0.007	0.0091	0.00097	0.00017	0.001	1030.928	180.6781	0.08	0.13	0.9986
Output_1_11	0.0098	0.0029	0.000897	0.000071	0.001	1114.827	88.24162	0.082	0.029	0.59112
Output_1_12	0.0175	0.0077	0.001046	0.00006	0.29376	956.0229	54.83879	0.11	0.053	0.21993
Output_1_13	0.0138	0.0093	0.00092	0.00016	0.0049976	1086.957	189.0359	0.11	0.14	0.95931
Output_1_14	0.062	0.037	0.00131	0.00029	0.96474	763.3588	168.9878	0.26	0.11	-0.59375
Output_1_15	0.0045	0.0043	0.00089	0.000085	0.058305	1123.596	107.3097	0.048	0.041	0.022086
Output_1_16	0.0047	0.0031	0.000948	0.000079	0.2327	1054.852	87.90436	0.039	0.022	-0.16332
Output_1_17	0.0042	0.0051	0.00093	0.00011	0.11086	1075.269	127.1823	0.036	0.053	0.064262
Output_1_18	0.0033	0.0052	0.000889	0.000057	0.001	1124.859	72.12259	0.038	0.04	0.26305
Output_1_19	0.0026	0.0058	0.000902	0.000082	0.056537	1108.647	100.7861	0.02	0.049	0.071063
Output_1_20	-0.0035	0.0062	0.00098	0.00014	0.001	1020.408	145.7726	-0.044	0.064	0.38086
Output_1_21	0.0052	0.0075	0.00091	0.00012	0.055614	1098.901	144.91	0.046	0.073	-0.022755
Output_1_22	0.0036	0.0046	0.000935	0.000067	0.10613	1069.519	76.63931	0.026	0.036	-0.18809
Output_1_23	0.0008	0.0084	0.000929	0.000093	0.27543	1076.426	107.7585	-0.024	0.069	-0.25553
Output_1_24	0.0014	0.0046	0.000839	0.000058	0.001	1191.895	82.39561	0.004	0.04	0.19953
Output_1_25	0.0048	0.0057	0.00099	0.00011	0.15354	1010.101	112.2334	0.012	0.046	0.1005
Output_1_26	-0.003	0.025	0.00083	0.00031	0.13197	1204.819	449.9927	0.13	0.66	-0.93361
Output_1_27	-0.003	0.014	0.00095	0.00015	0.001	1052.632	166.205	0.04	0.14	-0.17531
Output_1_28	0.0034	0.005	0.000989	0.00007	0.001	1011.122	71.56579	0.028	0.04	0.24086
Output_1_29	-0.004	0.017	0.00109	0.0002	0.001	917.4312	168.336	-0.02	0.12	0.51041
Output_1_30	0.024	0.016	0.0032	0.0016	0.74478	312.5	156.25	0.056	0.025	-0.054916

Table C-2. Data from U-Pb dating of zircons in sample RSW-261 (rhyolite porphyry dike).

RSWCB-261	AGE (in Ma) internal and standard propagated						Approximate Elemental Concentrations							
Analysis #	207/235 Age	2se	206/238 Age	2se	207/206 Age	2se	Approx_U_PPM	2se	Approx_Th_PPM	2se	Approx_Pb_PPM	2se	FInal_U_Th_Ratio	2se
Output_1_1	8.7	5.3	6.44	0.7	300	1100	506	24	451	72	0.11	0.12	1.13	0.11
Output_1_2	10.4	3.5	5.98	0.49	1010	750	521	15	437	10	0.06	0.11	1.163	0.011
Output_1_3	6.1	3.7	5.8	0.47	0	1000	723	24	702	30	0.302	0.099	1.003	0.011
Output_1_4	4.2	8.4	4.8	0.68	-1.40E+03	2.10E+03	380	15	277	13	0.091	0.097	1.325	0.016
Output_1_5	5.6	4.6	5.88	0.66	-200	1100	448	14	335.2	9.7	0.175	0.098	1.294	0.015
Output_1_6	10.3	5.3	5.7	0.54	800	980	484	15	374	11	0.222	0.09	1.235	0.011
Output_1_7	30.6	9	6.17	0.95	2.10E+03	1.40E+03	346	17	285	16	0.28	0.074	1.143	0.021
Output_1_8	8.6	3.8	6.01	0.49	650	920	485	12	529	11	0.18	0.11	0.8826	0.0085
Output_1_9	6.7	5.5	5.91	0.54	-500	1200	491	11	430.5	7.6	0.133	0.06	1.094	0.012
Output_1_10	6.8	9.2	6.2	1.1	-1.90E+03	2.60E+03	262	30	160	20	0.101	0.078	1.576	0.029
Output_1_11	9.9	2.9	5.78	0.46	960	730	708	17	803	17	0.391	0.088	0.823	0.0098
Output_1_12	17.5	7.7	6.74	0.39	1650	880	418	11	342.5	7.5	0.27	0.13	1.152	0.015
Output_1_13	13.7	9.3	5.9	1	100	2900	248.2	5.9	228.7	8.3	0.17	0.12	1.017	0.029
Output_1_14	58	33	8.5	1.8	2800	720	458	35	416	48	0.76	0.37	1.037	0.04
Output_1_15	4.5	4.3	5.73	0.55	-600	1300	535	16	508	13	0.3	0.1	0.991	0.012
Output_1_16	4.7	3.1	6.11	0.51	-340	800	564	11	935	32	0.491	0.095	0.554	0.013
Output_1_17	4.2	5.1	6.01	0.69	-700	1400	441	14	303.3	9.4	0.254	0.092	1.342	0.015
Output_1_18	3.3	5.3	5.73	0.37	-700	1300	591	16	541	14	0.23	0.078	1.001	0.013
Output_1_19	2.5	5.9	5.81	0.53	-1.50E+03	1.50E+03	457	16	373	11	0.181	0.088	1.114	0.019
Output_1_20	-3.7	6.3	6.29	0.93	-1.80E+03	1.60E+03	299	10	214.1	7.7	0.165	0.081	1.272	0.018
Output_1_21	5.1	7.6	5.85	0.77	-1.40E+03	1.80E+03	354	12	228.7	7.6	0.132	0.08	1.418	0.022
Output_1_22	3.6	4.6	6.02	0.43	-900	1100	552	17	540	17	0.307	0.094	0.9383	0.0091
Output_1_23	0.6	8.5	5.99	0.6	-2.40E+03	1.80E+03	415	11	338	6.9	0.008	0.094	1.14	0.01
Output_1_24	1.3	4.7	5.4	0.38	-1.70E+03	1.30E+03	671	21	768	31	0.37	0.1	0.8092	0.0088
Output_1_25	4.8	5.8	6.39	0.7	-1000	1300	448	15	349	11	0.142	0.07	1.185	0.012
Output_1_26	1	27	5.3	2	-1.40E+04	1.90E+04	115.4	3.5	147.3	3.9	0.03	0.072	0.752	0.012
Output_1_27	-4	14	6.11	0.95	-2.50E+03	2.80E+03	213.9	6.9	129.7	7.4	0.004	0.074	1.587	0.085
Output_1_28	3.4	5.1	6.38	0.45	-1.20E+03	1.20E+03	832	23	972	30	0.464	0.097	0.8109	0.0091
Output_1_29	-4	17	7	1.3	-4.30E+03	3.00E+03	141.3	3.8	135.4	3.6	0.099	0.087	0.992	0.013
Output_1_30	23	15	20	9.9	320	700	1130	400	1380	870	2.13	0.23	-1.10E+05	1.00E+05

Table C-2 continued. Data from U-Pb dating of zircons in sample RSW-261 (rhyolite porphyry dike).

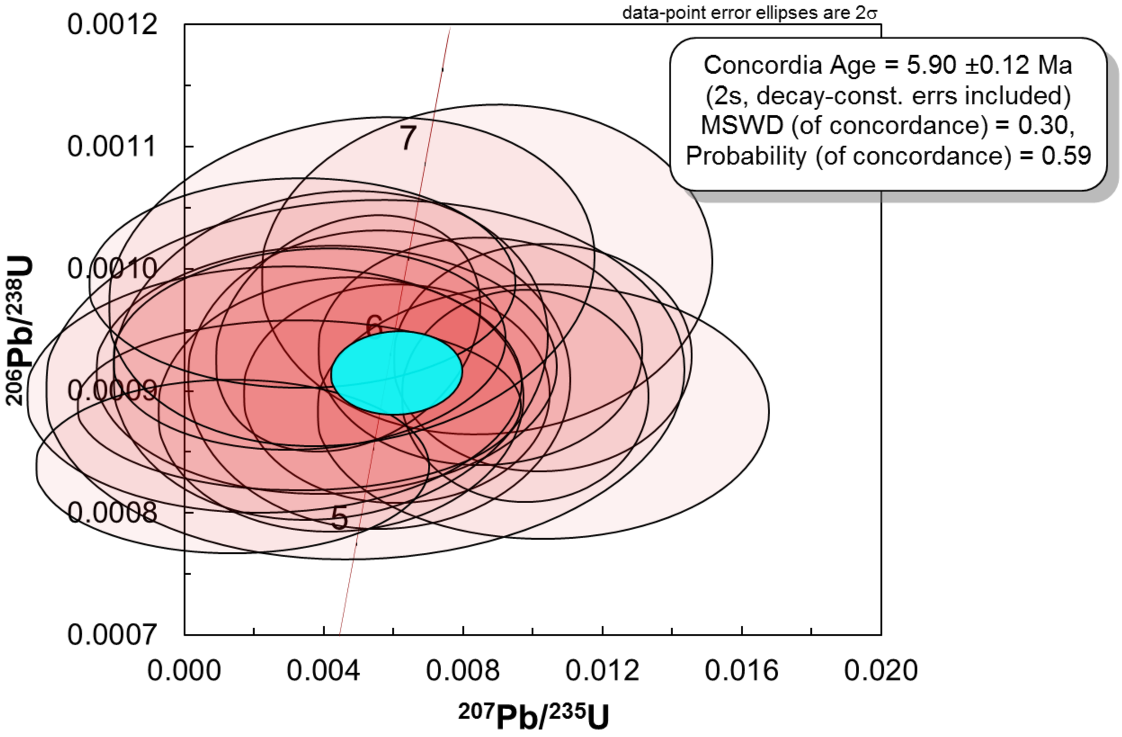

Figure C-2. Concordia diagram ^{206}Pb/^{238}U- ^{207}Pb/^{235}U for zircons in sample RSW-261 (rhyolite porphyry dike). The Concordia age is 5.9 ± 0.12 Ma.

Appendix D. Geochemistry of altered rocks

SAMPLE	RSW007X	RSW010W	RSW010X	RSW010Y	RSW010Z	RSW-217-5	RSW-216-6	RSW-223
Mineral Belt	Cameron	Cameron	Cameron	Cameron	Cameron	Cameron	Cameron	Cameron
Easting	304439	304881	304881	304881	304881	304968	304926	304411
Northing	4254591	4254149	4254149	4254149	4254149	4253949	4253986	4254455
Au (ppm)	0.028	0.244	0.019	0.545	0.112	0.372	0.058	0.07
Ag (ppm)	0.35	3.36	17.95	8.16	15.85	102	2.24	5.85
Al (%)	5.72	2.76	4.66	1.66	4.19	3.63	0.36	1.22
As (ppm)	776	39.3	69.8	198.5	156.5	597	198.5	33.3
Ba (ppm)	370	540	950	340	840	770	40	270
Be (ppm)	6.82	3.15	2.45	5	3.96	4.07	3.96	1.25
Bi (ppm)	0.22	0.1	0.19	0.09	0.15	0.07	0.02	0.07
Ca (%)	0.07	0.1	0.02	0.04	0.03	0.03	0.44	0.05
Cd (ppm)	0.02	0.03	0.02	0.02	<0.02	<0.02	0.07	0.05
Ce (ppm)	36.3	17	35	15.75	41.6	40.4	2.3	13.05
Co (ppm)	1.1	0.5	0.8	1.1	0.7	0.5	1.3	1
Cr (ppm)	9	24	12	23	11	18	36	52
Cs (ppm)	13.45	18.05	7.83	9.35	13.35	13.25	4.19	2.53
Cu (ppm)	7	3.7	20.6	4.8	6.6	4.4	3.5	5.6
Fe (%)	2.08	0.52	0.84	1.51	1.83	2.3	1.08	0.49
Ga (ppm)	19.05	8.41	8.02	5.01	8.07	8.19	5.33	2.5
Ge (ppm)	0.2	0.22	0.22	0.17	0.25	0.17	0.09	0.09
Hf (ppm)	3.4	1	2.4	0.5	2	1.6	0.1	0.7
Hg (ppm)	4.1	0.185	0.136	0.867	0.235	0.384	0.225	0.053
In (ppm)	0.02	0.005	0.006	<0.005	0.009	0.007	<0.005	0.008
K (%)	6.73	3.28	5.49	1.81	5.36	4.31	0.13	1.21
La (ppm)	25.7	8	19.5	6.5	21.9	15.2	1.1	5.8
Li (ppm)	42.5	176	120.5	276	185	195.5	164.5	199
Mg (%)	0.03	0.02	0.04	0.02	0.04	0.04	0.01	0.02
Mn (ppm)	87	90	103	164	134	66	243	55
Mo (ppm)	2.59	2.8	1.62	5.35	9.73	70.3	8.37	26.9
Na (%)	0.21	0.05	0.05	0.02	0.04	0.03	0.01	0.03
Nb (ppm)	22.6	3.4	8.7	2	7.4	5.7	0.4	1.9
Ni (ppm)	2.6	1.2	3.6	2.1	1.4	1.3	1.3	1.9
P (ppm)	80	470	30	410	270	540	5700	120
Pb (ppm)	22.4	10.7	17.9	9.7	18.8	16.5	3.3	3.3
Rb (ppm)	530	245	248	136.5	360	309	12.1	86.5
Re (ppm)	<0.002	<0.002	<0.002	<0.002	<0.002	0.002	<0.002	<0.002
S (%)	1.04	0.12	0.6	1.32	1.72	1.24	0.45	0.15
Sb (ppm)	84.2	22.4	10.55	45.8	21.5	34.3	35.9	12.05
Sc (ppm)	1.9	0.6	0.9	0.3	1.1	1.1	0.1	1.2
Se (ppm)	1	<1	1	1	1	2	1	1
Sn (ppm)	1.4	0.5	0.8	0.3	0.7	0.6	<0.2	0.3
Sr (ppm)	59.1	99	30.5	229	208	284	48	59.2
Ta (ppm)	1.39	0.25	0.61	0.15	0.54	0.4	<0.05	0.12
Te (ppm)	<0.05	<0.05	<0.05	<0.05	<0.05	0.19	0.26	<0.05
Th (ppm)	19.1	3.7	10.9	2.3	9.1	6.32	0.37	2.1
Ti (%)	0.089	0.038	0.067	0.02	0.069	0.066	<0.005	0.042
Tl (ppm)	11.7	2.11	3.68	3.09	4.31	5.22	1.1	0.79
U (ppm)	5.5	4	2.8	3.9	8.9	5.5	24.4	1.7
V (ppm)	5	7	5	8	25	30	8	27
W (ppm)	2.4	2.2	1.4	1.3	2.9	3.7	1.4	3.1
Y (ppm)	6	1.9	5.6	1.8	5	4.7	1.6	3.2
Zn (ppm)	2	<2	3	<2	<2	10	<2	7
Zr (ppm)	86.8	31.8	78.1	17.8	65.2	47.5	2	19.6

SAMPLE	RSW-237-2	RSW237-4	RSW-238-1	RSW-238-3	RSW-MCO	RSW-MC2	RSW-SC-12	SLP-06	SLP-07
Mineral Belt	Cameron	Cameron	Cameron	Cameron	Cameron	Cameron	Cameron	Cameron	Cameron
Easting	303530	303530	303936	303936	304968	304968	304445	303738	304443
Northing	4253092	4253092	4253295	4253295	4253949	4253949	4254379	4253424	4254584
Au (ppm)	8.54	17.9	0.041	0.053	0.468	0.358	0.074	0.008	0.055
Ag (ppm)	152	18	<1	0.67	3	25.2	<1	<1	8
Al (%)	3.75	1.4	4.41	4.44	1.94	1.95	6.35	6.61	5.97
As (ppm)	194	114	496	489	526	323	27	94	5
Ba (ppm)	460	116	216	770	248	230	522	1710	635
Be (ppm)	2.43	2.9	4.9	2.61	4.7	10	2.6	2	1.5
Bi (ppm)	0.3	0.47	0.14	0.09	0.05	0.07	0.12	0.16	0.12
Ca (%)	0.03	0.03	0.03	0.05	0.3	0.1	0.03	0.15	0.03
Cd (ppm)	<0.02	<0.1	<0.1	0.02	<0.1	0.12	<0.1	<0.1	<0.1
Ce (ppm)	41.7	10.2	41.7	107.5	8.02	18.45	82.7	33.9	35
Co (ppm)	0.4	0.2	0.3	6.5	1.9	1.8	0.3	0.4	0.4
Cr (ppm)	28	3	5	31	5	19	2	<1	<1
Cs (ppm)	7.91	<5	17	12	8	8.75	10	19	7
Cu (ppm)	14.3	7.8	2.3	61.5	2.3	7.7	4.5	2.9	9.8
Fe (%)	0.83	0.82	0.78	1.59	2.36	2.01	0.43	1.48	0.27
Ga (ppm)	9.6	6.67	17.3	6.54	6.17	6.89	15.5	16.4	12.4
Ge (ppm)	0.16			0.18		0.12			
Hf (ppm)	1.6			3.2		0.8			
Hg (ppm)	0.099	0.21	1.03	0.513	0.96	0.639	0.01	0.02	0.04
In (ppm)	0.012	<0.02	<0.02	0.015	<0.02	0.007	0.02	<0.02	<0.02
K (%)	4.37	1.41	5.1	4.9	1.96	1.86	8.1	4.86	5.47
La (ppm)	19.3	5	22.5	41.6	3.8	7.9	38.1	19.2	19.9
Li (ppm)	143	271	59	76.7	253	259	67	54	88
Mg (%)	0.03	0.02	0.01	0.01	0.04	0.05	0.01	0.14	0.09
Mn (ppm)	58	31	30	42	53	74	107	338	121
Mo (ppm)	88.6	108	7.37	12.5	45	41.6	3.97	2.08	3.32
Na (%)	0.1	0.03	0.11	0.2	0.02	0.02	0.09	0.13	0.07
Nb (ppm)	7.6	1.7	15.5	6.5	3.2	3.1	18.1	10.6	9
Ni (ppm)	1.2	<0.5	<0.5	9.1	1.6	2.2	<0.5	0.7	0.7
P (ppm)	80	197	54	200	3589	1980	117	330	<50
Pb (ppm)	20.4	53.4	17.8	10.6	6.6	11.2	14.3	25.3	8
Rb (ppm)	277	94	455	440	150	163.5	630	236	387
Re (ppm)	<0.002			<0.002		<0.002			
S (%)	0.16	0.12	0.35	1.34	1.94	1.58	0.03	0.06	0.02
Sb (ppm)	22.2	27.3	52	51	37.6	32.1	4.75	7.97	4.51
Sc (ppm)	1.8	0.9	2.3	5.9	1.1	1.1	2.9	1.7	1.4
Se (ppm)	7	0.6	0.3	1	<0.2	1	<0.2	<0.2	<0.2
Sn (ppm)	0.8	0.4	1.2	0.8	0.4	0.3	1.6	1	0.7
Sr (ppm)	124	60.1	37.9	127	37.2	121	65.9	89.8	66.4
Ta (ppm)	0.51			0.38		0.22			
Te (ppm)	0.13	0.3	<0.1	0.09	1.8	0.08	0.4	1.8	0.5
Th (ppm)	7.55	1.4	13.6	7.82	2.9	3.62	13.5	10.9	9.3
Ti (%)	0.071	0.01	0.08	0.255	0.04	0.045	0.08	0.1	0.08
Tl (ppm)	4.57	2	8.6	6.09	7.7	6.3	6.5	2.4	3.7
U (ppm)	2.9	0.7	4.3	2.5	1.2	3	3.6	3.7	3
V (ppm)	44	40	19	26	22	30	15	28	15
W (ppm)	3.5	1.3	11.2	12.1	2.5	2.2	4.3	8.9	0.7
Y (ppm)	6.1	1.3	10.1	26.9	2.5	3.4	13.8	7.7	7.9
Zn (ppm)	3	5	3	12	6	12	12	23	11
Zr (ppm)	44			118.5		23.5			

SAMPLE	RSW012A	RSW-074	RSW-088	RSW-088-2	RSW-088-5	RSW-088-6	RSW-089-3	RSW-144	RSW-144-3	RSW-172
Mineral Belt	Clinton	Clinton	Clinton	Clinton	Clinton	Clinton	Clinton	Clinton	Clinton	Clinton
Easting	302198	302865	302431	302431	302431	302431	302291	301637	301637	301802
Northing	4258042	4258679	4257941	4257941	4257941	4257941	4257882	4255241	4255241	4254493
Au (ppm)	0.027	<0.005	0.157	0.058	0.012	0.017	0.017	0.017	0.582	1.325
Ag (ppm)	12	1.16	245	88.4	3	12	2	10.4	135	1050
Al (%)	4.18	6.85	4.36	2.57	4.4	6.88	4.46	6.69	5.75	3.94
As (ppm)	20.6	10.5	13.2	6.8	23	6	36	19.3	134.5	11.5
Ba (ppm)	370	1030	680	320	638	1167	733	1500	1140	410
Be (ppm)	1.13	1.46	1.59	1.05	1.2	1.6	2.1	1.78	2.35	1.17
Bi (ppm)	0.1	0.26	0.1	0.04	0.13	<0.04	0.05	0.44	0.19	0.16
Ca (%)	0.04	1.02	0.07	0.04	0.03	0.06	0.04	0.04	0.05	0.03
Cd (ppm)	0.05	<0.02	0.6	0.1	<0.1	0.2	<0.1	<0.02	0.08	0.28
Ce (ppm)	16.55	59	61.1	25.2	47.8	70.1	53.3	67.3	83.7	10.65
Co (ppm)	0.6	3.9	1	0.7	1	1.4	2	0.2	1.2	0.2
Cr (ppm)	8	12	11	22	4	<1	1	9	16	11
Cs (ppm)	3.9	5.3	7.56	3.82	6	9	9	6.72	10.7	4.77
Cu (ppm)	61.2	18.9	668	45.9	5.8	16.7	18.7	9.1	16.6	20.5
Fe (%)	0.66	1.8	0.97	0.5	0.85	1.05	0.97	0.94	2.4	0.49
Ga (ppm)	8.87	15.7	10.2	5.98	11.2	17.8	12.5	13.1	11.9	5.83
Ge (ppm)	0.24	0.18	0.18	0.11				0.18	0.18	0.14
Hf (ppm)	0.3	1.9	0.6	0.4				2	2	0.2
Hg (ppm)	0.086	<0.005	0.108	0.075	0.01	0.05	0.05	0.022	0.587	0.278
In (ppm)	0.014	0.025	0.04	0.008	<0.02	<0.02	<0.02	0.018	0.03	0.03
K (%)	4.77	4.41	3.63	2.3	3.27	4.45	2.85	6.08	4.38	4.29
La (ppm)	9.3	34.8	34.5	12.3	22.9	34.9	26	37.6	32.7	5.8
Li (ppm)	55.9	29.4	68.7	74.7	58	32	54	39.5	57.9	93.9
Mg (%)	0.08	0.45	0.17	0.1	0.18	0.26	0.23	0.16	0.1	0.07
Mn (ppm)	102	286	161	98	114	271	114	121	48	78
Mo (ppm)	105	10.55	36.2	65.9	160	23.9	63.1	70.2	16.85	28.2
Na (%)	0.1	1.59	0.11	0.04	0.2	0.38	0.16	0.27	0.13	0.08
Nb (ppm)	3.3	14	7	3.8	9.3	14.3	9.9	16.7	5.1	1.5
Ni (ppm)	1.2	4.8	1.5	0.9	<0.5	1.3	1	0.9	1.4	1.3
P (ppm)	140	550	420	90	322	255	139	190	970	300
Pb (ppm)	90.8	18	535	29.8	40.7	69.4	23.6	23.7	24.4	413
Rb (ppm)	287	212	210	151	168	243	174	303	296	243
Re (ppm)	<0.002	<0.002	<0.002	<0.002				<0.002	<0.002	<0.002
S (%)	0.3	0.18	0.69	0.41	0.65	0.81	0.91	0.19	0.7	0.08
Sb (ppm)	5.38	2.5	16.3	5.43	4.02	6.94	3.42	3.94	5.6	14.9
Sc (ppm)	0.7	4.8	1.7	0.7	2	2.5	2.3	2.5	6.7	0.5
Se (ppm)	1	1	3	1	0.7	0.2	<0.2	<1	1	4
Sn (ppm)	0.5	1.5	1.4	0.4	0.9	1.2	0.9	1.8	0.7	0.6
Sr (ppm)	55.9	317	187	59.5	50.9	102	101	201	340	112
Ta (ppm)	0.22	0.99	0.48	0.22				1.24	0.26	0.1
Te (ppm)	9.4	0.26	94.8	41.6	4	6	3.5	3.08	77.6	390
Th (ppm)	3	14.8	6.6	2.66	6.1	11.2	5.1	13.6	2.24	1.2
Ti (%)	0.04	0.198	0.094	0.047	0.11	0.15	0.13	0.196	0.29	0.025
Tl (ppm)	4.91	3.29	3.63	2.39	2.2	3.7	2.4	4.73	9.14	5.3
U (ppm)	0.9	3.7	1.8	0.7	1.6	2.6	1.2	3.8	3.1	0.7
V (ppm)	9	49	23	12	23	27	28	23	68	9
W (ppm)	4.7	6	12.2	5.7	9.4	13.7	7.5	7.4	17.7	5.7
Y (ppm)	1.8	8	4.4	2.3	4	5.3	4	7.2	7.5	1.4
Zn (ppm)	15	27	154	30	7	54	30	7	17	73
Zr (ppm)	9.1	46.7	15.6	8.4				52.2	71.4	4.9

SAMPLE	BF 172-3	RSW-176	RSW188-1	RSW188-2	RSW188-3	RSW199-4	RSW199-3	RSW-KTK2	RSW-KTK5	SILM15-1A
Mineral Belt	Clinton	Clinton	Clinton	Clinton	Clinton	Clinton	Clinton	Clinton	Clinton	Clinton
Easting	301802	302089	304924	304924	304924	302444	302444	302110	302110	302444
Northing	4254493	4256539	4256725	4256725	4256725	4257941	4257941	4256496	4256496	4257941
Au (ppm)	0.067	<0.005	0.7	0.933	1.9	0.007	0.01	0.023	0.278	0.683
Ag (ppm)	0.66	1.75	572	1415	2120	<1	2	165	624	803
Al (%)	7.72	5.79	3.91	3.37	4.94	6.06	2.26	4.62	3.8	3.9
As (ppm)	88.2	7.4	10.1	76.8	60.6	22	9	37	25.2	18
Ba (ppm)	1370	1020	320	420	520	665	279	561	570	620
Be (ppm)	2.17	1.56	1.18	1.39	1.09	1.9	1.2	1.6	1.54	1.2
Bi (ppm)	0.14	0.13	0.06	0.08	0.1	0.3	0.07	0.08	0.05	0.41
Ca (%)	0.08	0.08	0.02	0.04	0.03	0.07	0.02	0.02	0.02	0.04
Cd (ppm)	0.02	0.02	0.07	<0.02	0.1	<0.1	<0.1	<0.1	<0.02	2.3
Ce (ppm)	102	48.5	11.55	23.4	7.17	51.2	26.4	48.5	34.7	29.3
Co (ppm)	0.8	0.6	0.2	0.2	0.2	1.3	0.8	0.2	0.2	0.8
Cr (ppm)	6	7	45	54	24	4	5	2	17	7
Cs (ppm)	8.95	7.69	4.83	4.94	4.24	7	<5	8	5.48	<5
Cu (ppm)	6	10	8.8	10.9	11.7	5.4	8.2	32.4	13.7	1666
Fe (%)	1.13	0.93	0.3	0.55	0.51	0.65	0.48	0.39	0.49	0.54
Ga (ppm)	20.4	14.1	7.19	7.45	8.52	15.9	7.15	11.7	10.1	10
Ge (ppm)	0.2	0.16	0.07	0.08	0.07				0.13	
Hf (ppm)	2.2	2.2	0.3	0.3	<0.1				0.8	
Hg (ppm)	0.011	0.007	0.053	0.343	0.234	0.02	0.01	0.02	0.137	0.29
In (ppm)	0.032	0.019	0.013	0.012	0.033	0.02	<0.02	<0.02	0.022	0.11
K (%)	5	4.59	4.17	3.39	5.39	3.18	1.57	3.56	3.46	3.21
La (ppm)	49.5	27.7	6.1	11.2	2.9	24.1	13	23.6	16.4	15.7
Li (ppm)	39.4	50.9	91.2	125	59.7	46	74	54	117	76
Mg (%)	0.25	0.12	0.07	0.1	0.09	0.26	0.12	0.19	0.15	0.09
Mn (ppm)	182	124	71	108	71	161	159	100	84	86
Mo (ppm)	21.3	1.37	72.6	846	635	82.9	123	63.9	166	15.7
Na (%)	1	0.84	0.07	0.06	0.09	1.33	0.03	0.15	0.05	0.28
Nb (ppm)	20.1	9.6	2.3	2.7	0.1	10.9	5.4	10.9	6.2	7
Ni (ppm)	0.8	1.3	1	0.9	0.7	2.1	<0.5	<0.5	0.6	<0.5
P (ppm)	410	140	90	310	420	97	79	173	140	269
Pb (ppm)	18.7	18.3	81.8	1050	1320	27.7	25.5	25.7	40.1	1643
Rb (ppm)	344	266	256	203	295	194	103	220	214	171
Re (ppm)	<0.002	<0.002	<0.002	0.004	0.005				<0.002	
S (%)	0.03	0.01	0.05	0.08	0.04	0.53	0.43	0.14	0.09	0.61
Sb (ppm)	4.26	1.31	7.99	72.2	109.5	4.96	3.76	26.8	35.7	24.4
Sc (ppm)	2.8	2.5	0.7	0.7	0.4	3.7	1.4	2.7	2.1	1.5
Se (ppm)	1	<1	1	3	3	<0.2	<0.2	1	3	3.8
Sn (ppm)	1.6	1	0.6	1.5	0.6	1.2	0.6	1.2	0.8	1.2
Sr (ppm)	206	146	48	137.5	111	93.2	44.3	62.8	91.7	92.9
Ta (ppm)	1.29	0.68	0.15	0.18	<0.05				0.36	
Te (ppm)	<0.05	0.88	147	>500	>500	0.8	1.1	70.3	148	2726
Th (ppm)	16.9	8.5	1.89	5.13	0.48	6.4	3.4	7	3.63	3.8
Ti (%)	0.203	0.151	0.04	0.04	<0.005	0.13	0.06	0.15	0.125	0.06
Tl (ppm)	2.93	3.4	5.5	5.65	9.4	2.3	1.7	4	4.39	4.5
U (ppm)	4.8	2.6	0.5	1.1	0.5	1.7	1	1.8	1.2	0.9
V (ppm)	31	19	16	139	25	28	19	31	63	12
W (ppm)	5	4.3	4.3	3.7	0.4	8.4	8	16.4	20.1	6.2
Y (ppm)	14.2	6.5	1.4	1.7	0.6	3.8	7.1	4.1	3.5	3.1
Zn (ppm)	23	17	28	26	43	9	17	4	10	603
Zr (ppm)	54.9	71.4							23.9	

SAMPLE	SILM15-2	SLP-03	SLP-03(B)	SLP-14	RSW-MtPat	RSW-MP5	RSW-MP6
Mineral Belt	Clinton	Clinton	Clinton	Clinton	Comstock	Comstock	Comstock
Easting	302444	301619	301619	302226	299165	299282	299282
Northing	4257941	4255439	4255439	4254686	4256074	4256454	4256454
Au (ppm)	0.103	0.135	0.474	0.012	1.12	1.55	1.37
Ag (ppm)	171	91	192	1	112	391	223
Al (%)	3.43	6.18	5.35	7.52	1.22	1.68	1.91
As (ppm)	10	84	50	29	5.7	7.9	42
Ba (ppm)	321	942	584	1210	40	290	192
Be (ppm)	1.8	6	5.2	2	29.9	5.28	11.2
Bi (ppm)	0.23	0.44	1.16	0.1	0.38	0.88	0.19
Ca (%)	0.02	0.09	0.03	0.09	0.02	0.03	0.03
Cd (ppm)	0.1	<0.1	<0.1	<0.1	0.07	0.02	<0.1
Ce (ppm)	32.2	32.5	23.8	51.2	1.05	18.6	22.9
Co (ppm)	1	0.5	0.3	0.1	0.6	0.3	0.2
Cr (ppm)	7	3	2	<1	41	26	4
Cs (ppm)	7	<5	<5	6	3.24	1.83	<5
Cu (ppm)	109	14.1	14.4	3.1	184	8.6	7.6
Fe (%)	0.64	1.12	1.46	0.63	0.24	0.54	2.29
Ga (ppm)	12.2	11.4	8.07	17.5	4.49	3.72	7.07
Ge (ppm)					<0.05	0.13	
Hf (ppm)					0.1	0.5	
Hg (ppm)	0.13	0.13	0.42	0.02	0.11	2.26	42.3
In (ppm)	0.1	<0.02	<0.02	0.03	<0.005	0.01	<0.02
K (%)	2.64	4.09	4.83	4.87	1.22	1.22	0.72
La (ppm)	17.8	18.2	12.2	28.5	0.7	8	10.9
Li (ppm)	71	42	69	25	231	85.1	82
Mg (%)	0.14	0.03	0.02	0.05	0.01	0.07	0.09
Mn (ppm)	121	61	70	28	67	153	297
Mo (ppm)	83.9	17.6	15.6	5.88	6.22	0.94	11.8
Na (%)	0.05	2.1	0.35	1.63	0.03	0.01	<0.01
Nb (ppm)	7.4	10.1	2.5	20.2	0.2	2.5	3.5
Ni (ppm)	0.6	2.4	1.1	0.9	1	1.2	2.2
P (ppm)	104	430	670	130	30	100	170
Pb (ppm)	144	36	54.8	6.2	12	120	34.1
Rb (ppm)	163	205	322	311	85.2	76.6	49.1
Re (ppm)					<0.002	<0.002	
S (%)	0.62	0.16	0.07	<0.01	0.03	0.1	0.04
Sb (ppm)	10.1	7.83	7.42	2.68	8.34	3.61	35.7
Sc (ppm)	1.7	1.5	0.6	2.9	0.2	0.7	1.4
Se (ppm)	1.1	0.5	0.2	<0.2	<1	10	2.5
Sn (ppm)	1.1	0.9	0.7	1.5	0.3	0.4	1
Sr (ppm)	52.3	209	136	243	15.5	42.7	49.1
Ta (ppm)					<0.05	0.17	
Te (ppm)	52.9	70	132	0.2	5.64	2.44	4.9
Th (ppm)	4.7	7.6	1.5	11.2	0.27	2.23	2.9
Ti (%)	0.07	0.09	0.03	0.2	<0.005	0.035	0.04
Tl (ppm)	2.9	2.7	5.9	3.3	1.78	1.06	0.7
U (ppm)	1.2	3.1	1.5	3.7	0.1	1	1
V (ppm)	18	18	16	21	2	6	11
W (ppm)	8.3	2.9	1.2	8.3	0.1	0.4	1.2
Y (ppm)	2.7	7	4	6.6	0.2	1.7	1.8
Zn (ppm)	30	10	13	8	4	8	12
Zr (ppm)						12.2	

SAMPLE	RSW-085	RSW-114	RSW-138	RSW-195	RSW-204	SLP-01	SLP-09	SLP-10
Mineral Belt	N/A	N/A	N/A	N/A	N/A	N/A	N/A	N/A
Easting	302293	303814	303654	303926	304170	304568	300167	299743
Northing	4257976	4258397	4256521	4257957	4254769	4258325	4254829	4256951
Au (ppm)	0.088	<0.005	0.023	<0.005	0.017	0.003	0.004	0.016
Ag (ppm)	16	15.1	6.82	<1	0.57	<1	<1	<1
Al (%)	2.51	5.26	5.1	9.45	7.69	6.27	6.85	6.58
As (ppm)	12	6.3	4.8	3	12.1	69	9	14
Ba (ppm)	52	540	190	665	970	438	1070	1550
Be (ppm)	0.4	2.28	1.75	3	2.46	2.4	2.7	2.3
Bi (ppm)	1.12	35.1	0.5	0.14	0.35	0.12	0.16	<0.04
Ca (%)	0.02	0.08	0.14	1.98	1.21	0.05	0.06	0.05
Cd (ppm)	<0.1	<0.02	0.14	<0.1	<0.02	<0.1	<0.1	<0.1
Ce (ppm)	6.09	20	24	40.1	79.2	49.4	77.1	57.3
Co (ppm)	0.4	0.2	3.2	9.2	0.3	0.5	0.3	0.2
Cr (ppm)	1	17	9	15	9	14	<1	<1
Cs (ppm)	<5	6.07	2.91	5	8.78	<5	7	<5
Cu (ppm)	4.9	3.8	30.1	24.7	24.8	3.5	1.6	2.1
Fe (%)	0.23	0.4	0.54	3.06	0.34	0.53	0.34	0.86
Ga (ppm)	36.8	11.55	11.75	17.4	18.9	13.3	17	15.5
Ge (ppm)		0.15	0.12		0.19			
Hf (ppm)		0.2	0.1		0.2			
Hg (ppm)	0.06	0.032	0.048	0.01	0.032	0.09	0.02	0.07
In (ppm)	0.35	0.014	0.017	0.04	0.023	<0.02	0.03	<0.02
K (%)	0.9	3.41	1.49	1.94	4.7	4.64	5.24	4.74
La (ppm)	4.6	11.9	11.5	18.3	29	32.4	37.9	32.2
Li (ppm)	64	27.8	39.3	44	21.8	48	45	38
Mg (%)	0.01	0.14	0.16	1.02	0.08	0.1	0.14	0.23
Mn (ppm)	24	51	429	595	140	139	83	136
Mo (ppm)	10.8	107	9.54	22.7	>10000	7.07	1.95	4.86
Na (%)	0.05	1.44	3.43	2.82	1.23	0.36	0.37	0.06
Nb (ppm)	27.5	5.8	4.9	9.1	11.4	23	27.2	16.6
Ni (ppm)	0.5	1	1.3	5.9	0.7	7.7	1.1	<0.5
P (ppm)	<50	80	310	1055	6190	90	90	130
Pb (ppm)	120	43.9	316	11.9	35.4	11.5	15.8	9.5
Rb (ppm)	72.6	217	91.3	140	281	224	363	267
Re (ppm)		<0.002	<0.002		2.11			
S (%)	0.07	0.05	0.01	0.29	1.09	0.03	<0.01	0.25
Sb (ppm)	17.8	3.09	5.97	0.41	2.9	3.86	2.2	3.9
Sc (ppm)	0.7	3	1.8	17	2	2.3	4.2	4.4
Se (ppm)	0.5	<1	<1	<0.2	5	<0.2	<0.2	<0.2
Sn (ppm)	1.1	1.5	1	2.1	1.6	1.2	1.9	1.3
Sr (ppm)	12.9	61.3	43.9	406	201	71.2	143	163
Ta (ppm)		0.61	0.54		0.96			
Te (ppm)	1.8	3.14	3.63	0.2	0.73	0.3	0.3	0.2
Th (ppm)	4.2	6.6	26	9.2	24.9	17.4	18.2	10
Ti (%)	0.08	0.109	0.075	0.37	0.081	0.14	0.1	0.24
Tl (ppm)	0.7	2.35	1.64	1.2	2.49	2	4.6	2.8
U (ppm)	2.3	2.9	8.8	2	5.5	4.9	5.2	2.8
V (ppm)	4	27	12	91	13	17	16	28
W (ppm)	25.3	4.1	4.6	4.2	4.2	5	4.9	8.2
Y (ppm)	0.8	2.1	8.9	13.3	69.7	8.3	17.8	10.6
Zn (ppm)	2	3	23	49	11	9	31	7
Zr (ppm)		4.5	3		4.5			

Table D-1. Multielement geochemistry for altered rocks from the Patterson mining district. Coordinates are given in NAD83, zone 11N. Some elemental concentrations are not given because of differences in analytical packages between laboratories.

Appendix E. Correlation matrices

	Au	Ag	Al	As	Ca	Cd	Cu	Fe	Hg	K	Li	Mg	Mo	Na	Pb	S	Sb	Se	Te	Ti	Tl	V	W	Zn
Au	1	0.56	-0.54	0.0059	0.077	0.43	-0.13	0.16	-0.041	-0.53	0.76	0.14	0.71	-0.5	0.072	0.082	-0.044	0.25	0.1	-0.68	-0.21	0.6	-0.15	0.2
Ag		1	-0.033	-0.18	-0.62	0.33	0.25	-0.077	-0.31	-0.051	0.41	0.45	0.5	-0.15	0.44	-0.064	-0.47	0.42	-0.24	-0.2	-0.059	0.62	0.0044	0.043
Al			1	-0.1	-0.51	-0.66	0.35	-0.18	-0.14	0.98	-0.79	0.14	-0.53	0.8	0.38	-0.18	-0.21	0.021	0.033	0.85	0.59	-0.31	0.28	0.05
As				1	0.33	-0.26	-0.25	0.83	0.89	-0.069	-0.024	0.009	0.26	-0.0015	0.16	0.7	0.88	0.071	-0.33	0.14	0.59	0.087	0.32	-0.34
Ca					1	0.73	-0.4	0.34	0.39	-0.53	0.22	-0.15	0.058	-0.39	-0.57	0.31	0.47	0.00	-0.091	-0.23	-0.012	-0.15	-0.091	0.21
Cd						1	-0.39	-0.18	-0.25	-0.66	0.46	0.072	0.67	-0.67	-0.37	-0.13	-0.33	-	-0.5	-0.33	-0.34	0.62	-0.0064	0.52
Cu							1	-0.09	-0.3	0.28	-0.12	0.28	0.0059	0.37	0.35	-0.063	-0.3	0.19	-0.45	0.32	-0.11	0.21	-0.15	0.06
Fe								1	0.74	-0.1	0.26	0.33	0.29	-0.27	0.12	0.9	0.6	0.43	-0.27	-0.065	0.41	0.1	0.11	-0.16
Hg									1	-0.094	0.065	-0.009	0.062	-0.052	0.11	0.71	0.91	-0.3	-0.28	0.0036	0.53	-0.099	0.12	-0.37
K										1	-0.76	0.16	-0.55	0.77	0.46	-0.11	-0.2	0.021	0.17	0.8	0.6	-0.35	0.29	-0.14
Li											1	0.27	0.55	-0.84	-0.22	0.3	-0.041	0.025	-0.067	-0.89	-0.48	0.4	-0.42	0.21
Mg												1	0.063	-0.19	0.12	0.27	-0.33	0.45	0.11	-0.12	0.11	0.12	-0.38	0.036
Mo													1	-0.36	0.063	0.23	0.11	0.25	-0.25	-0.34	-0.059	0.93	0.24	0.099
Na														1	0.48	-0.3	0.038	-0.046	-0.18	0.84	0.48	-0.14	0.47	-0.3
Pb															1	-0.035	0.037	-0.088	-0.28	0.17	0.31	0.16	0.11	-0.62
S																1	0.53	0.22	-0.35	-0.054	0.35	0.093	0.17	0.028
Sb																	1	-0.25	-0.27	0.068	0.42	-0.078	0.22	-0.31
Se																		1	-0.33	0.12	0.0042	0.27	0.23	0.11
Te																			1	-0.16	0.067	-0.49	-0.35	-0.27
Ti																				1	0.62	-0.18	0.52	0.029
Tl																					1	-0.013	0.52	-0.092
V																						1	0.33	0.17
W																							1	0.18
Zn																								1

Table E-1. Spearman correlation matrix for Cameron belt deposits.

	Au	Ag	Al	As	Ca	Cd	Cu	Fe	Hg	K	Li	Mg	Mo	Na	Pb	S	Sb	Se	Te	Ti	Tl	V	W	Zn
Au	1	0.89	-0.14	0.29	-0.11	0.25	0.3	-0.14	0.79	0.32	0.59	-0.64	-0.13	-0.23	0.62	-0.48	0.74	0.6	0.91	-0.45	0.73	-0.12	-0.34	0.46
Ag		1	-0.37	0.22	-0.38	0.65	0.31	-0.41	0.76	-0.054	0.72	-0.53	0.3	-0.41	0.8	-0.17	0.88	0.67	0.96	-0.57	0.61	-0.11	-0.13	0.32
Al			1	0.32	0.68	-0.4	-0.036	0.74	-0.23	0.72	-0.78	0.44	-0.43	0.88	-0.46	0.0027	-0.33	-0.35	-0.26	0.67	0.19	0.32	-0.084	-0.024
As				1	0.14	-0.18	-0.058	0.3	0.28	0.31	-0.026	-0.093	0.037	0.27	-0.0038	-0.12	0.31	0.037	0.39	0.21	0.36	0.36	-0.066	-0.2
Ca					1	-0.24	0.12	0.75	-0.092	0.39	-0.6	0.34	-0.46	0.74	-0.35	0.16	-0.4	-0.11	-0.28	0.48	-0.023	0.24	-0.18	0.21
Cd						1	0.72	-0.24	0.57	-0.53	0.48	-0.028	0.0035	-0.22	0.76	0.59	0.8	0.61	0.56	-0.29	0.074	-0.22	0.51	0.93
Cu							1	0.13	0.37	0.06	0.21	-0.045	-0.23	-0.037	0.3	0.4	0.29	0.36	0.38	-0.16	0.32	-0.22	0.098	0.63
Fe								1	0.062	0.49	-0.61	0.34	-0.42	0.72	-0.4	0.3	-0.46	-0.34	-0.24	0.5	0.1	0.32	-0.12	0.078
Hg									1	0.094	0.46	-0.55	0.017	-0.22	0.56	-0.028	0.56	0.41	0.78	-0.46	0.61	-0.0039	-0.25	0.27
K										1	-0.38	0.01	-0.21	0.49	-0.12	-0.36	-0.048	-0.11	0.17	0.28	0.68	0.11	-0.38	0.095
Li											1	-0.55	0.32	-0.74	0.63	-0.12	0.6	0.58	0.66	-0.7	0.26	-0.3	0.0092	0.3
Mg												1	0.091	0.38	-0.51	0.41	-0.42	0.032	-0.48	0.69	-0.33	0.65	0.38	-0.01
Mo													1	-0.53	0.28	0.052	0.2	0.37	0.22	-0.31	0.029	0.26	-0.11	-0.13
Na														1	-0.4	0.052	-0.39	-0.4	-0.29	0.52	7.70E-04	0.21	-0.15	-0.085
Pb															1	-0.014	0.78	0.49	0.7	-0.7	0.34	-0.41	-0.083	0.4
S																1	-0.19	-0.08	-0.23	0.22	-0.27	0.1	0.54	0.22
Sb																	1	0.52	0.8	-0.38	0.45	-0.094	0.11	0.22
Se																		1	0.68	-0.21	0.37	0.095	-0.014	0.54
Te																			1	-0.52	0.7	-0.055	-0.24	0.41
Ti																				1	-0.16	0.6	0.45	-0.19
Tl																					1	0.11	-0.32	0.31
V																						1	0.15	-0.16
W																							1	-0.13
Zn																								1

Table E-1. Spearman correlation matrix for Clinton belt deposits.

Appendix F. Additional backscatter SEM images

SEM images from deposits of the Cameron belt:

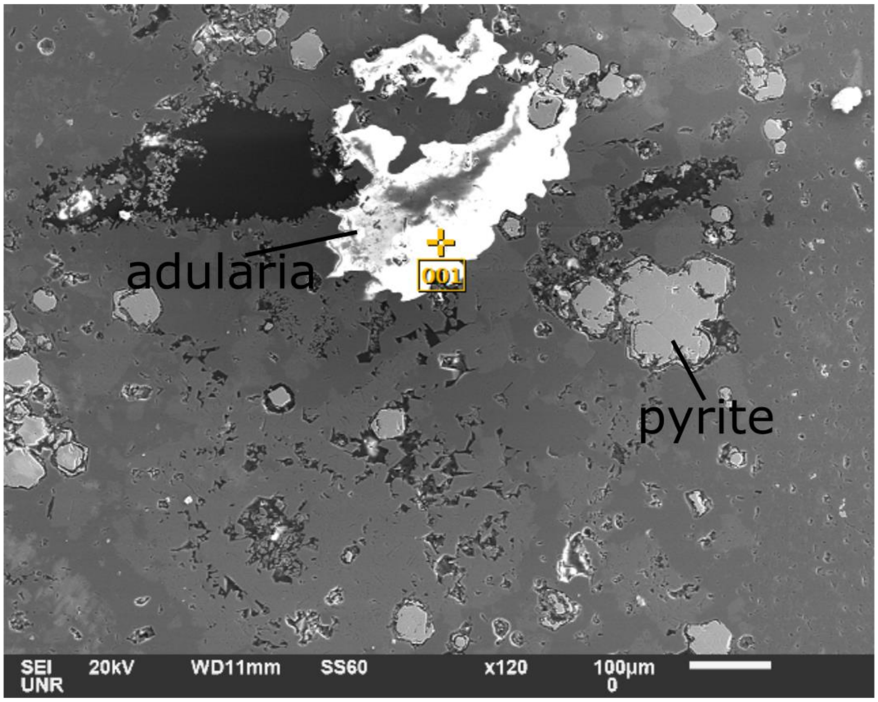

Figure F-1. Adularia and rimmed pyrite in sample RSW217-5 from the Monte Cristo mine.

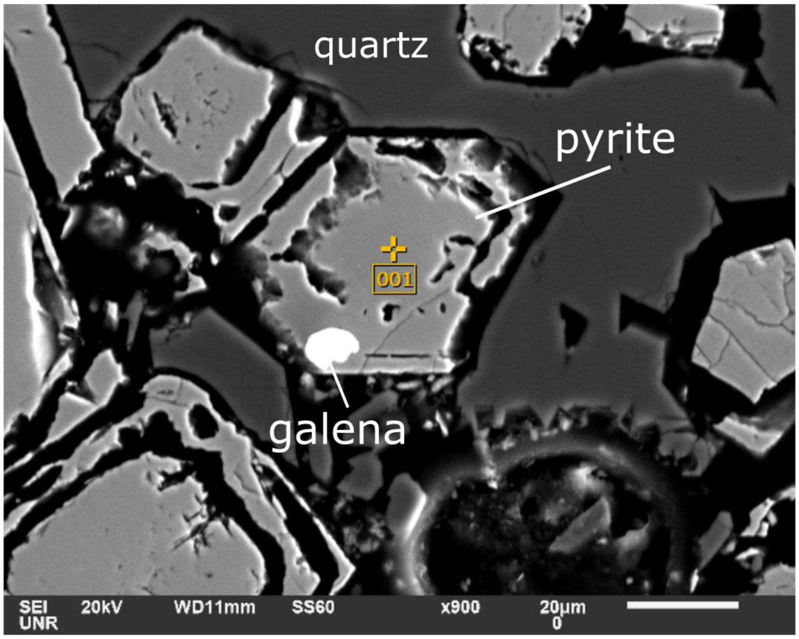

Figure F-2. Galena inclusion in rimmed pyrite in sample RSW217-5 from the Monte Cristo mine.

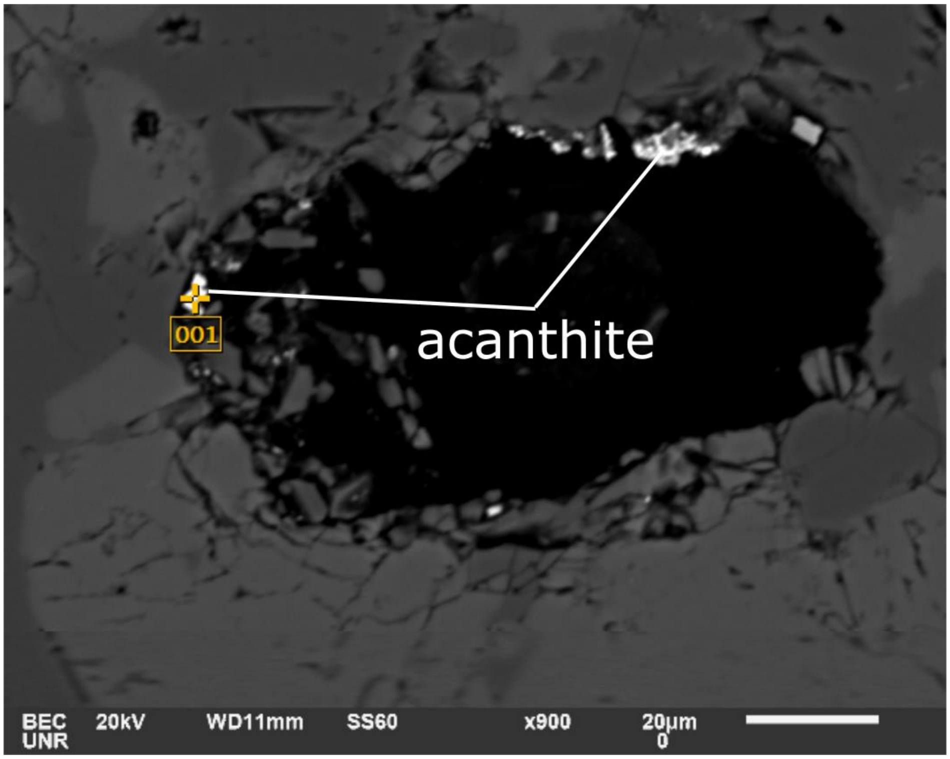

Figure F-3. Acanthite on the edge of a void in sample RSW237-2 from the Fryingpan Canyon mine.

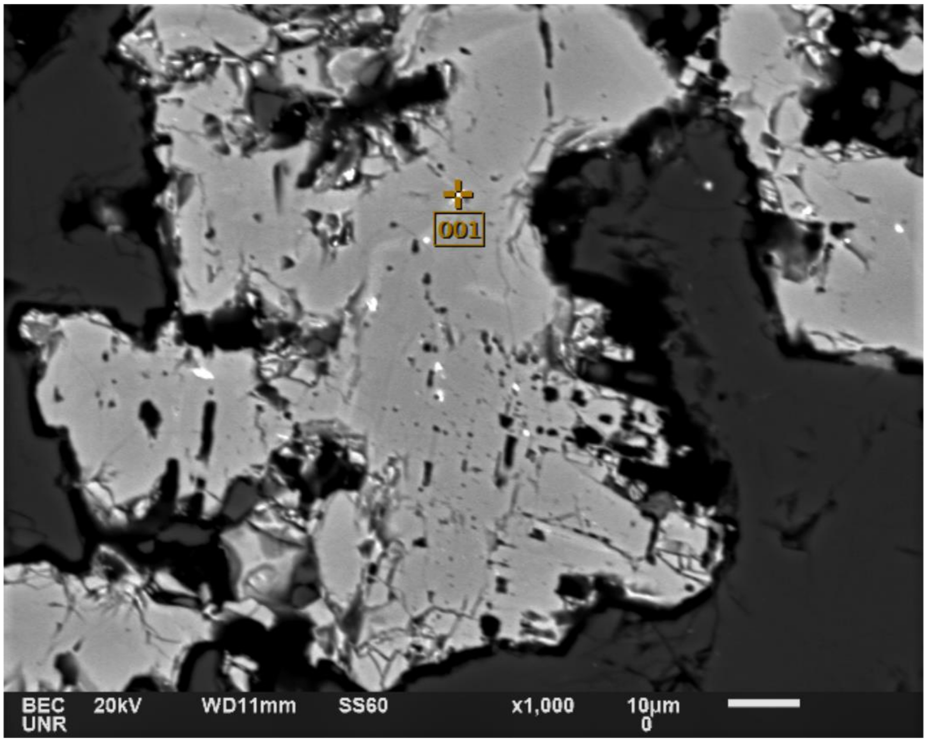

Figure F-4. Inclusions of acanthite and galena within pyrite in sample RSW237-2 from the Fryingpan Canyon mine.

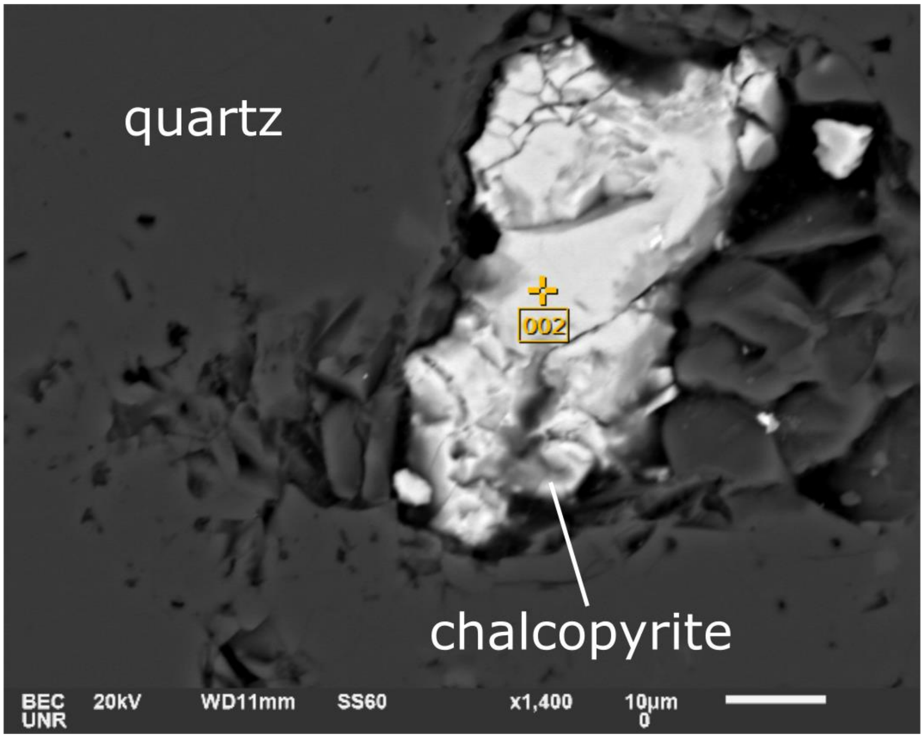

Figure F-5. Fine-grained chalcopyrite in sample RSW237-2 from the Fryingpan Canyon mine.

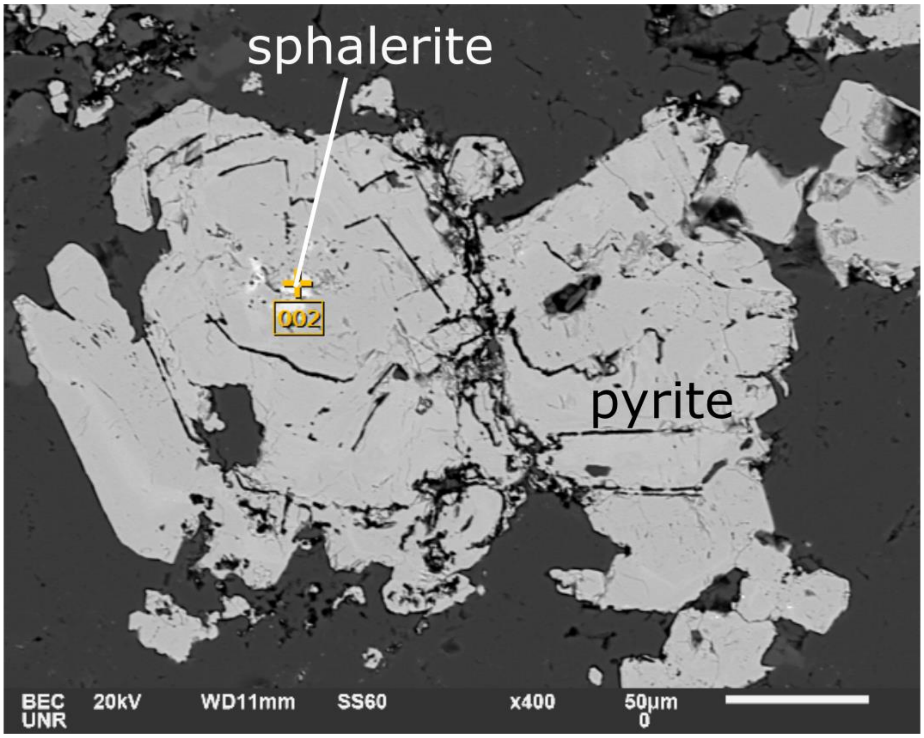

Figure F-6. Sphalerite inclusions within pyrite in sample RSW237-2 from the Fryingpan Canyon mine.

SEM images from deposits of the Clinton belt:

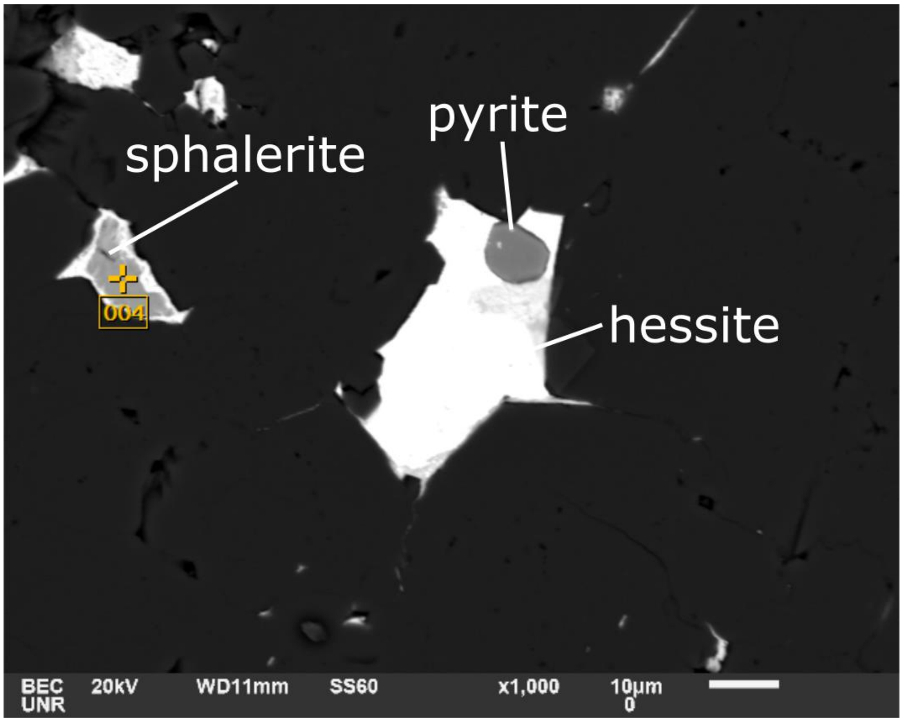

Figure F-7. Hessite after pyrite and sphalerite in sample RSW188-1 collected at a mill site at Clinton.

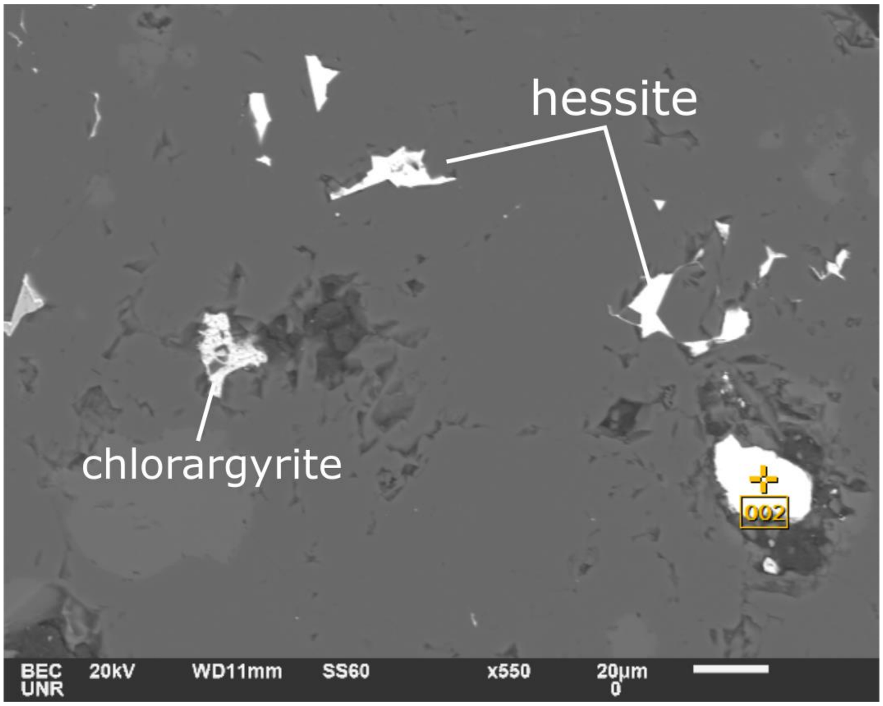

Figure F-8. Hessite and chlorargyrite in sample RSW188-1 collected at a mill site at Clinton.

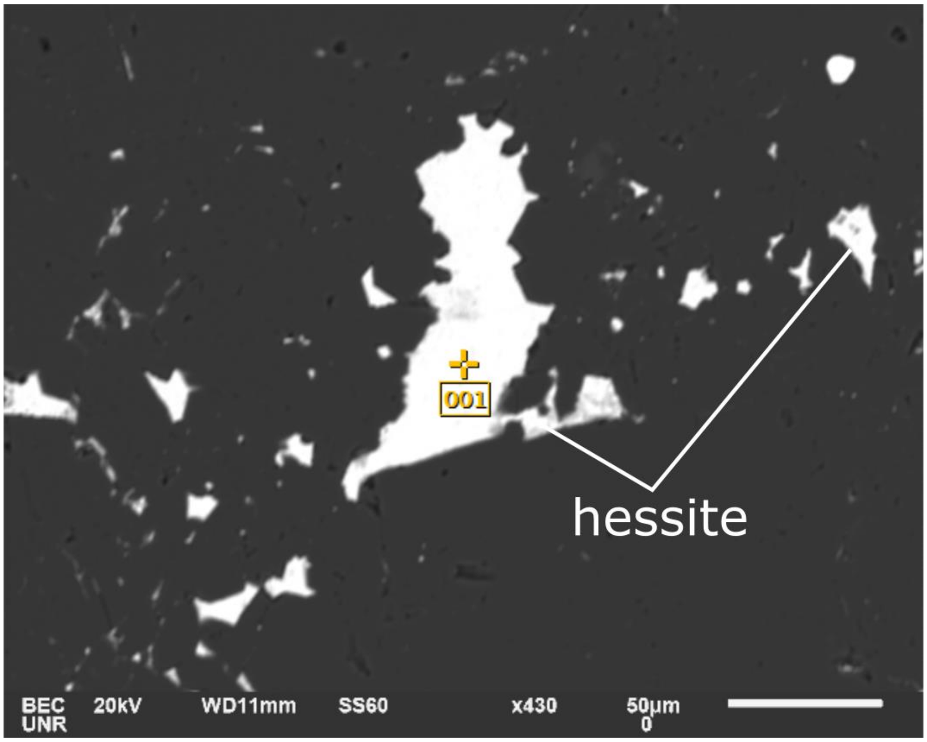

Figure F-9. Hessite in fine-grained quartz in sample RSW188-2 collected at a mill site at Clinton.

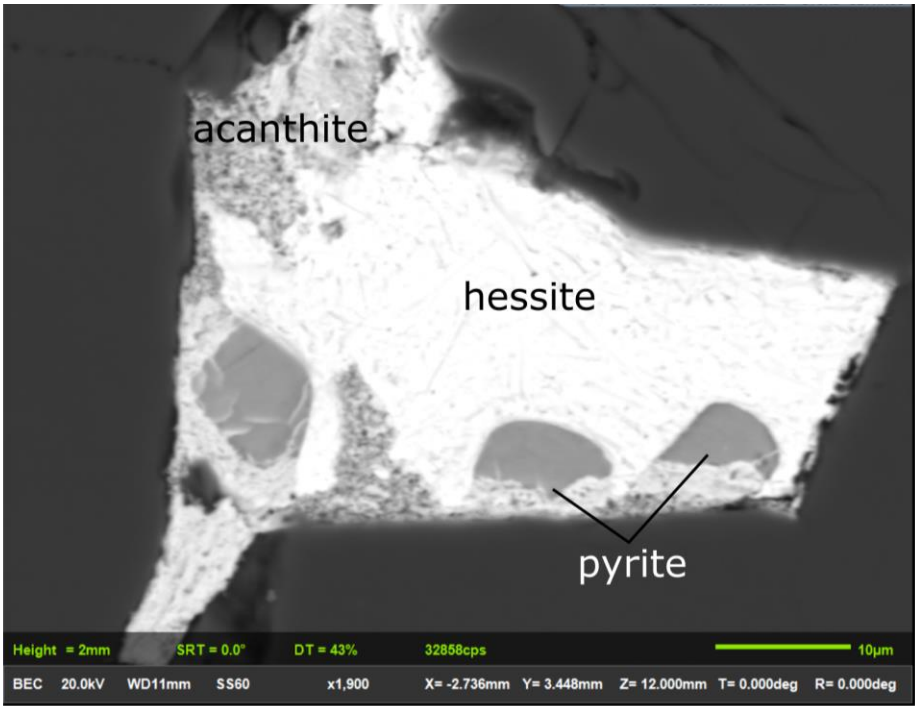

Figure F-10. Hessite after pyrite and acanthite in sample KTK-5 from the Kentuck mine.

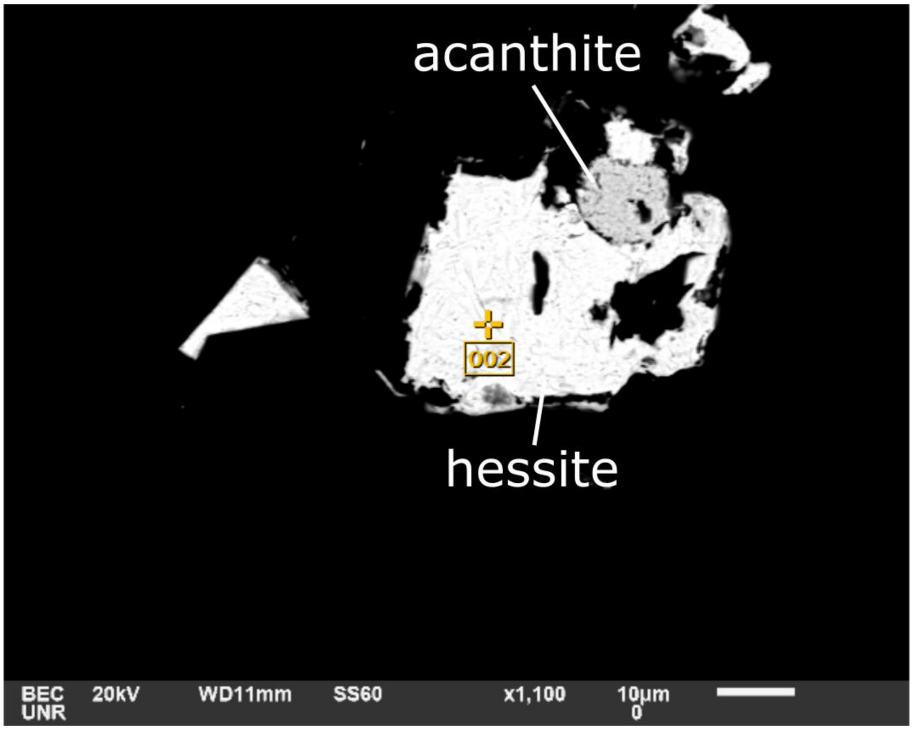

Figure F-11. Hessite after acanthite in sample KTK-5 from the Kentuck mine.

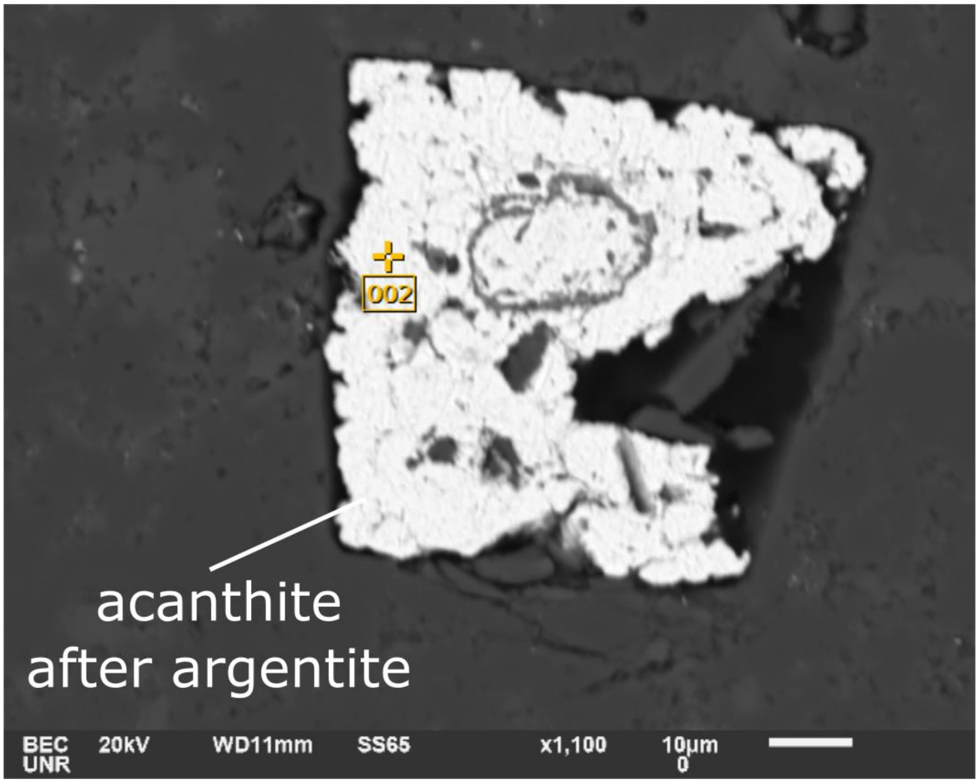

Figure F-12. Cubic acanthite which precipitated as argentite in sample KTK-3 from the Kentuck mine.

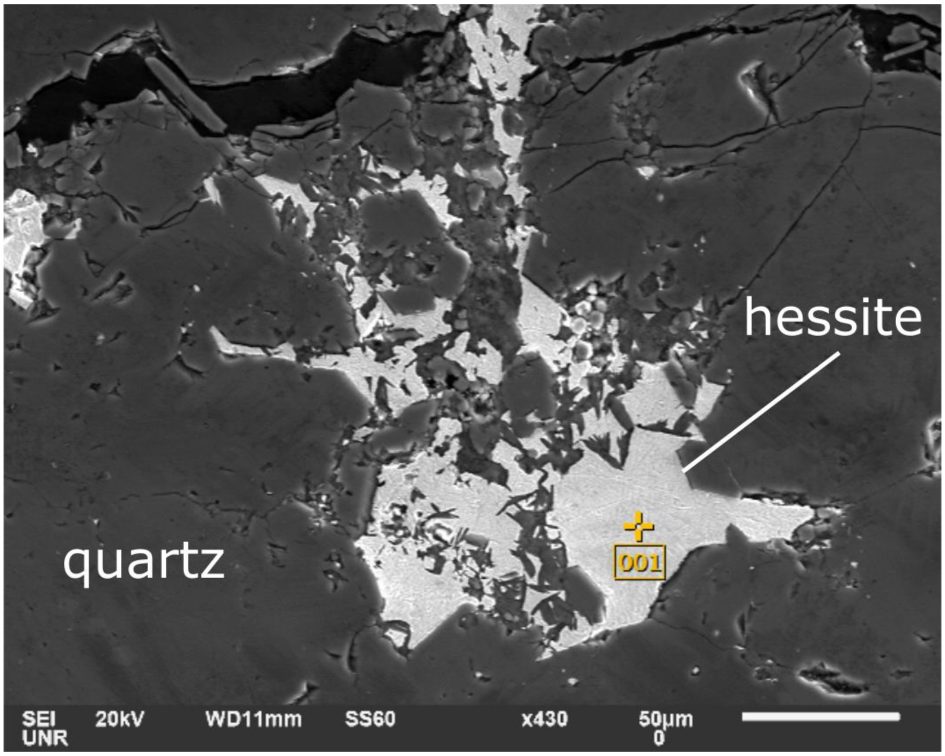

Figure F-13. Hessite in fine-grained quartz in sample USV-1 from the Silverado mine.

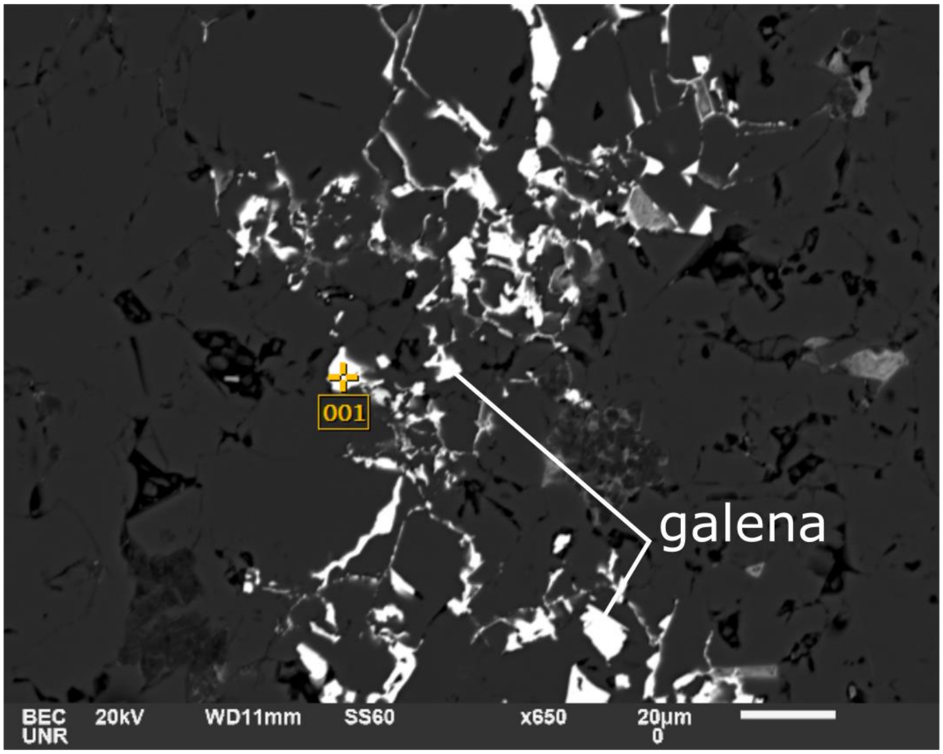

Figure F-14. Galena filling fractures and voids in fine-grained quartz in sample RSW188-1 collected at a mill site at Clinton.

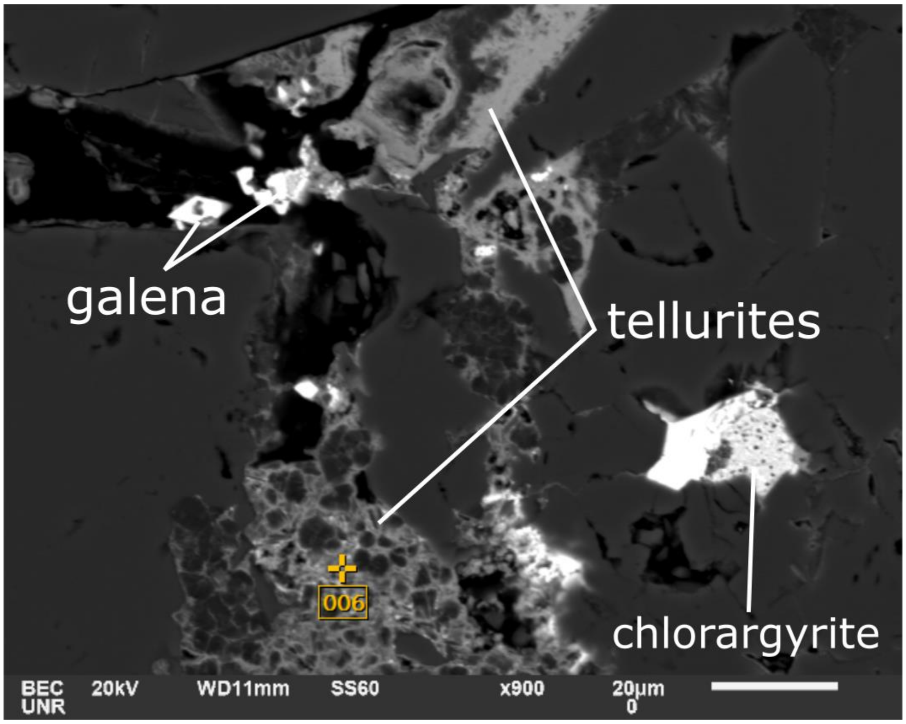

Figure F-15. Galena, acanthite partially replaced by chlorargyrite, and iron tellurites that are the result of oxidation of hessite in sample RSW188-1 collected from a millsite in Clinton.

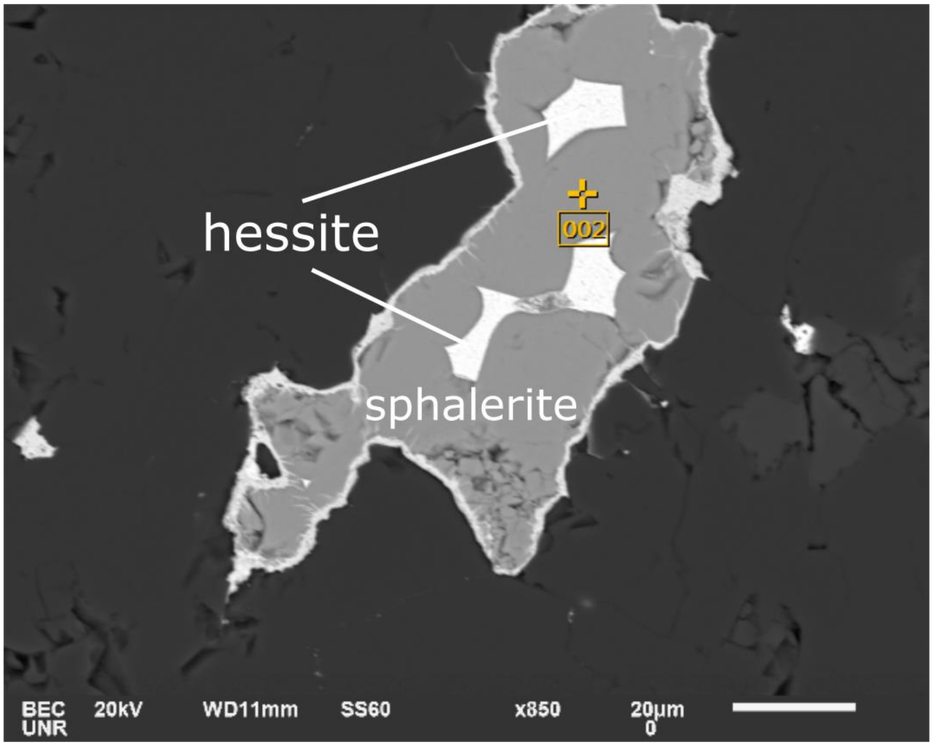

Figure F-16. Hessite filling a void within sphalerite in sample RSW188-2 collected from a millsite in Clinton.

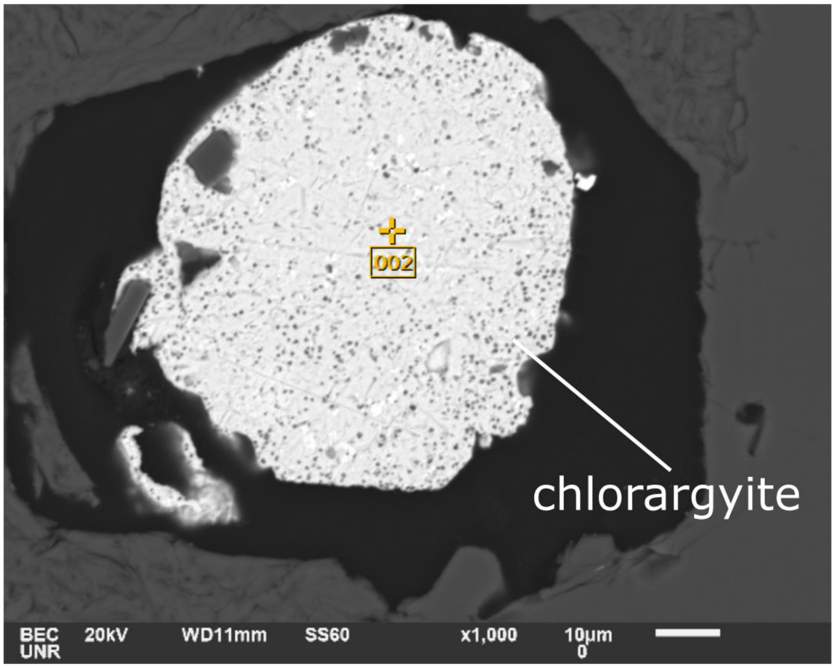

Figure F-17. Anhedral chlorargyrite in sample RSW188-2 collected from a millsite in Clinton.

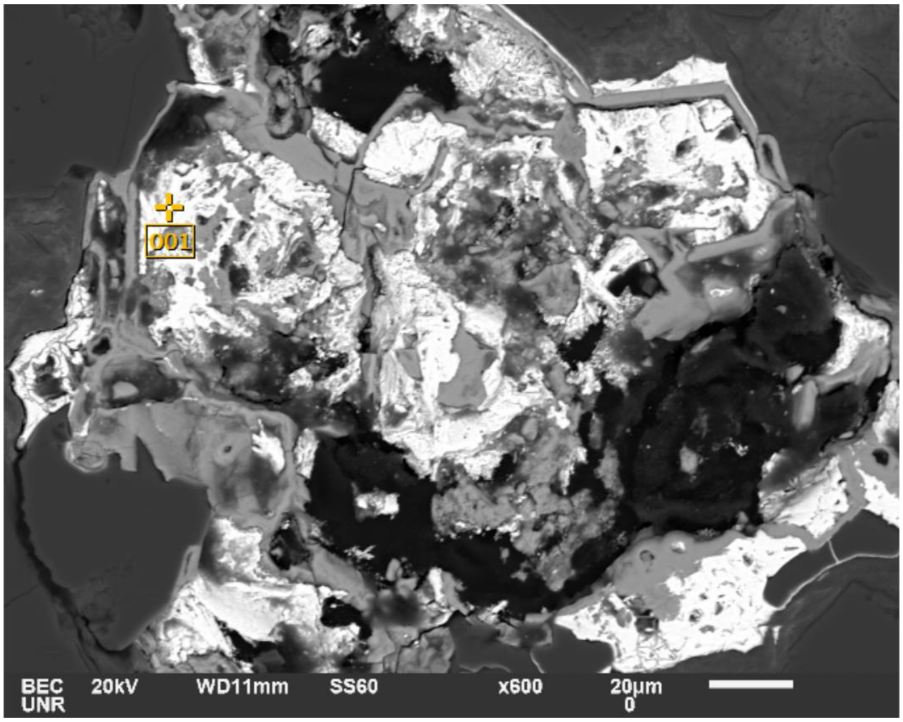

Figure F-18. Complex intergrowths of galena, acanthite, chlorargyrite, hessite, and iron tellurites in sample RSW188-4 collected from a millsite in Clinton.

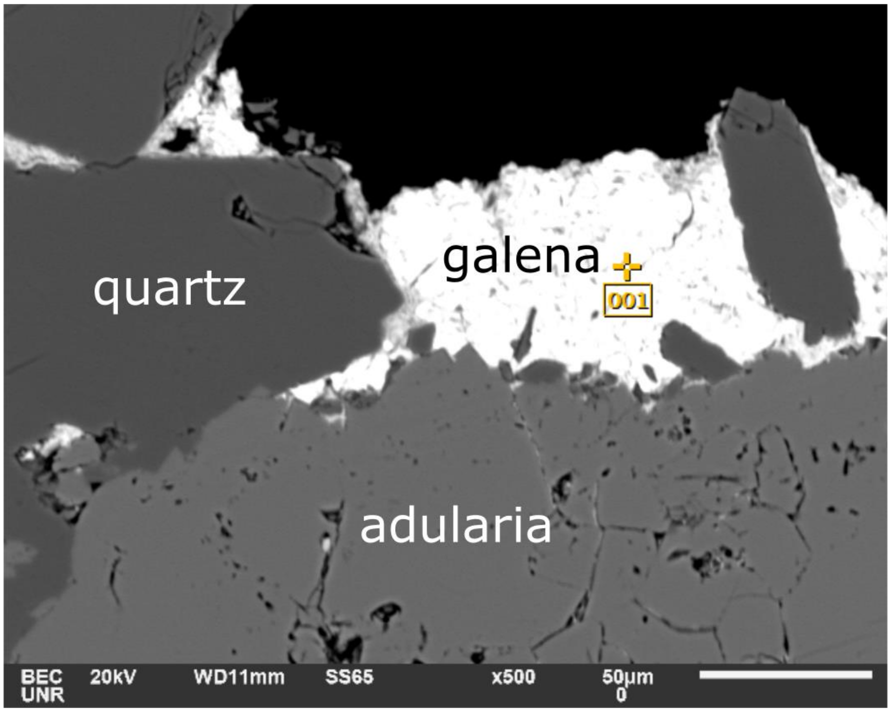

Figure F-19. Galena filling a void formed in quartz and adularia in sample CL-3 collected at Clinton.

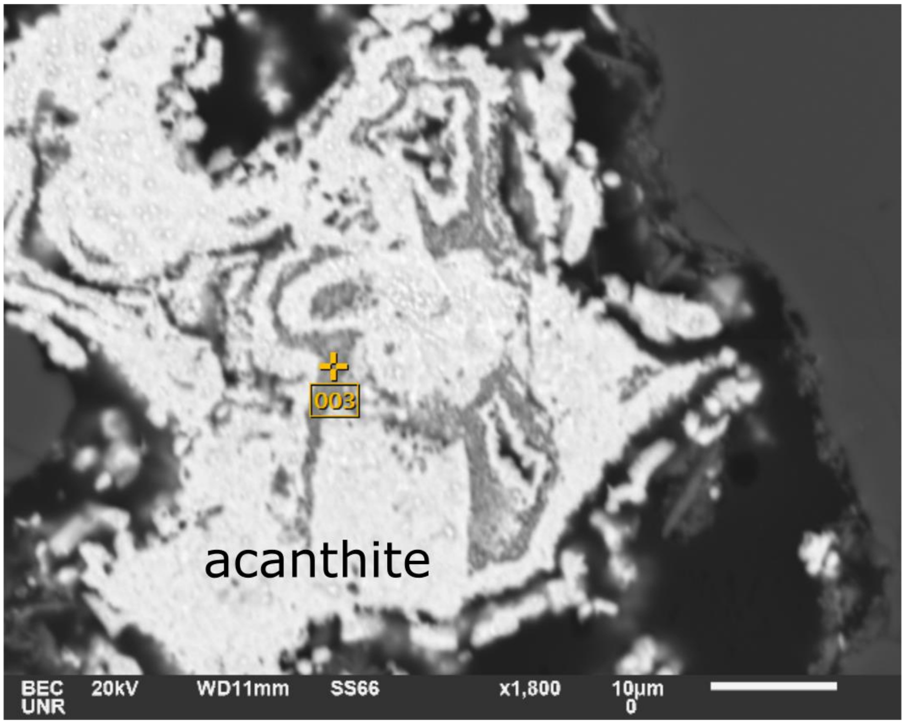

Figure F-20. Colloform acanthite in a void in sample KTK-5 from the Kentuck mine.

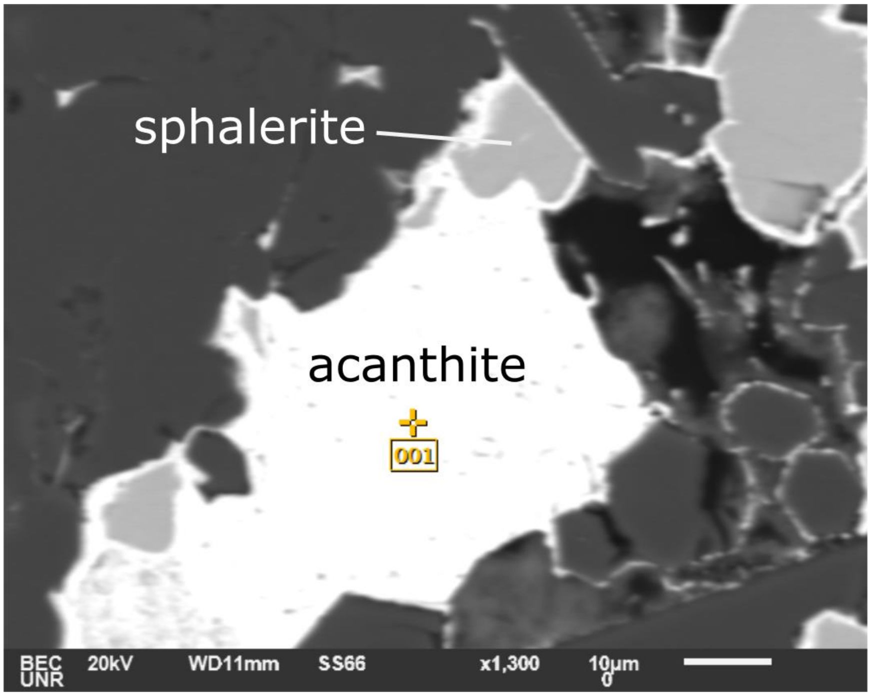

Figure F-21. Acanthite surrounding quartz and sphalerite in sample KTK-3 from the Kentuck mine.

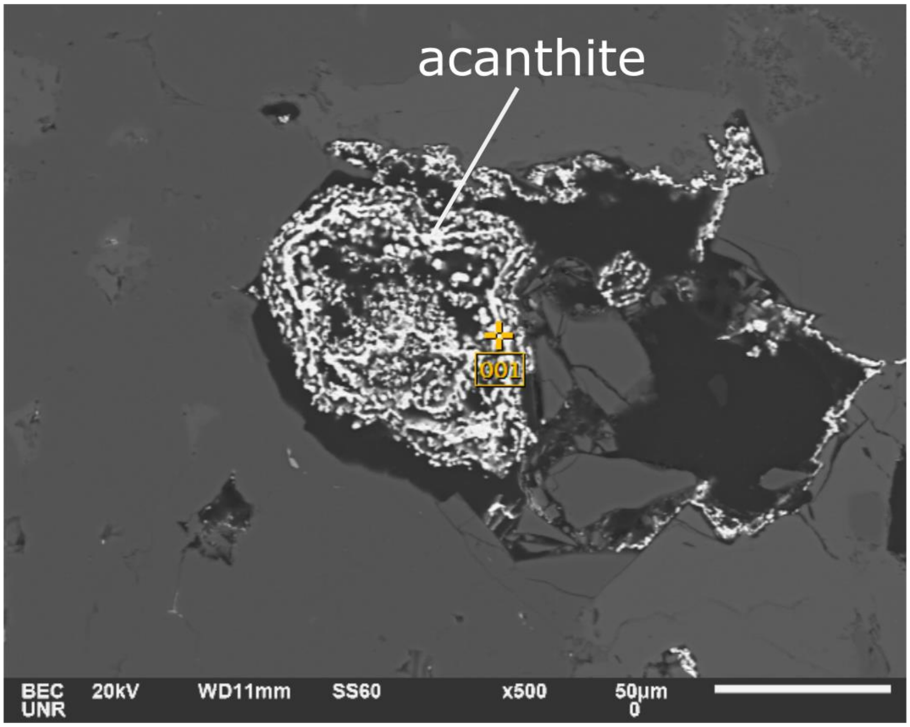

Figure F-22. Acanthite (in part with a colloform habit) filling a void in sample KTK-5 from the Kentuck mine.

SEM images from deposits of the California Comstock belt:

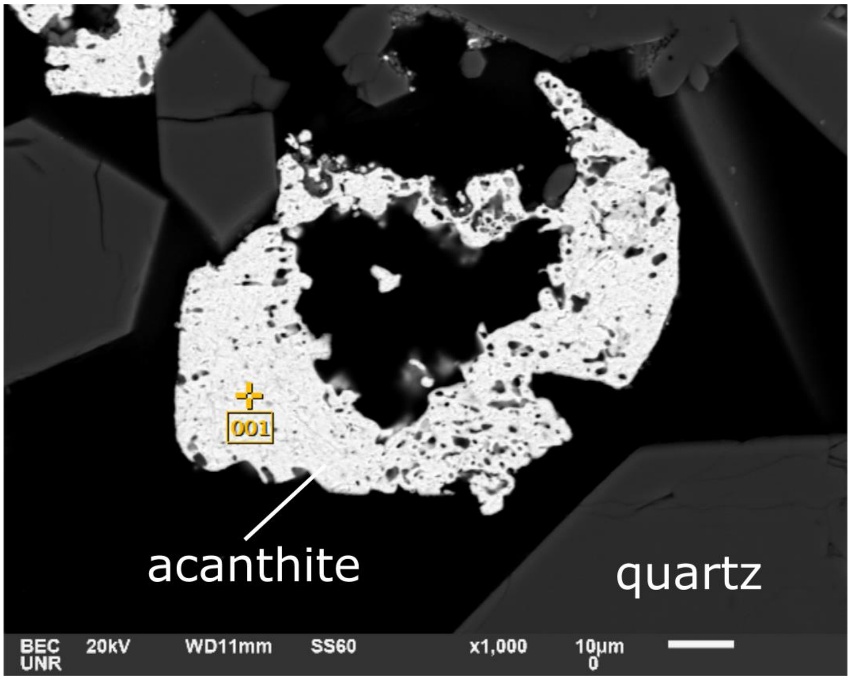

Figure F-23. Acanthite (that contains ~4% Se) in a void in quartz in sample MP-5 from the Star & Great Western claims near Mt. Patterson.

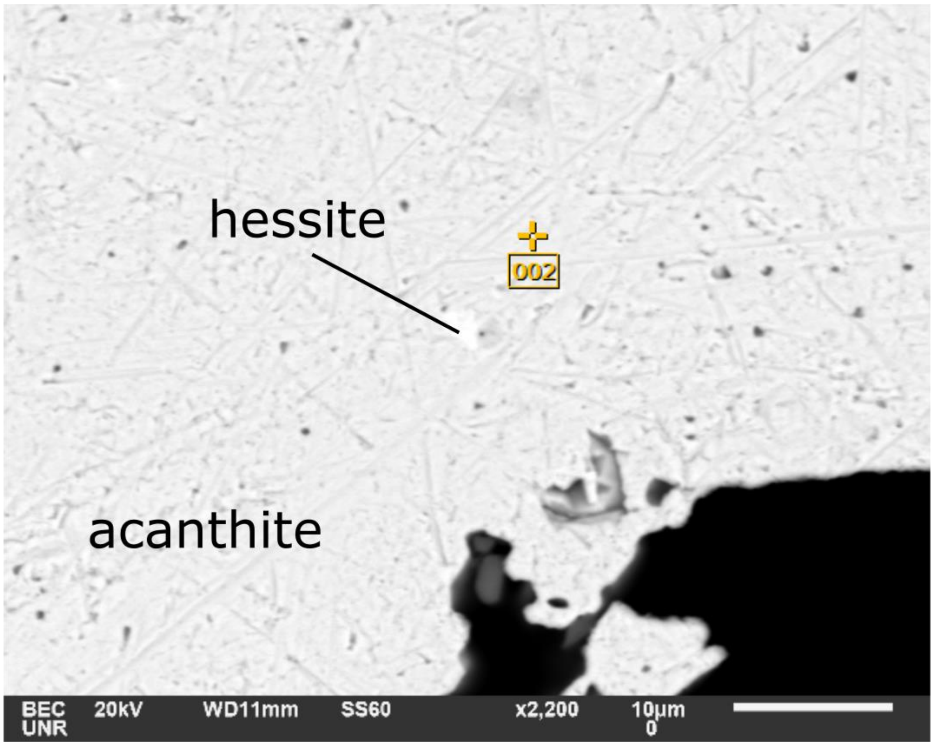

Figure F-24. A small grain of hessite within acanthite in sample MP-5 from the Star & Great Western claims near Mt. Patterson.

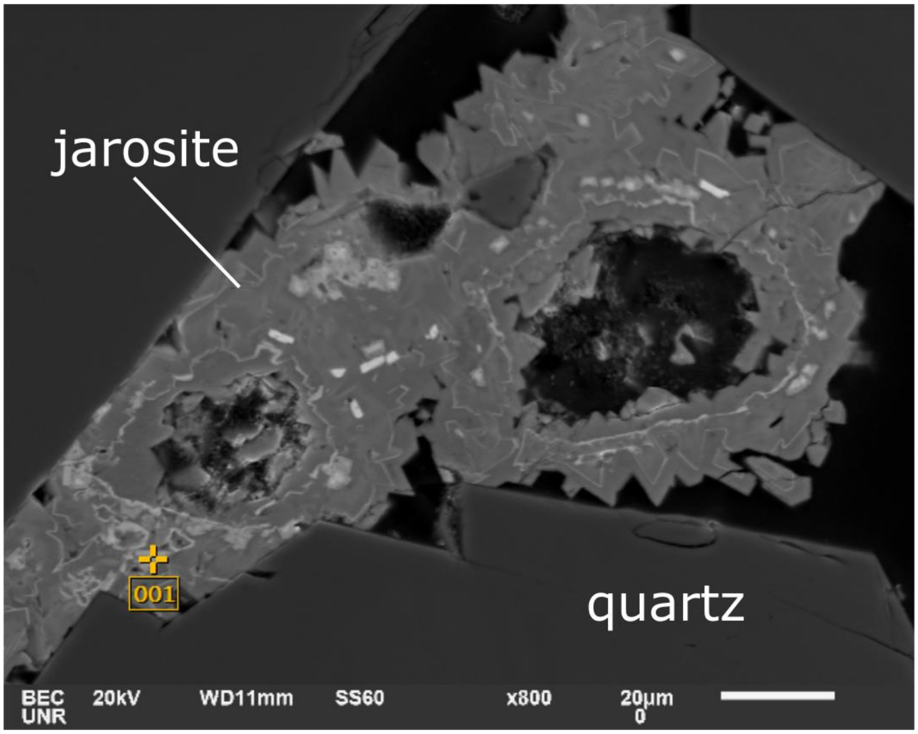

Figure F-25. Supergene jarosite filling a void in quartz in sample MP-5 from the Star & Great Western claims near Mt. Patterson.

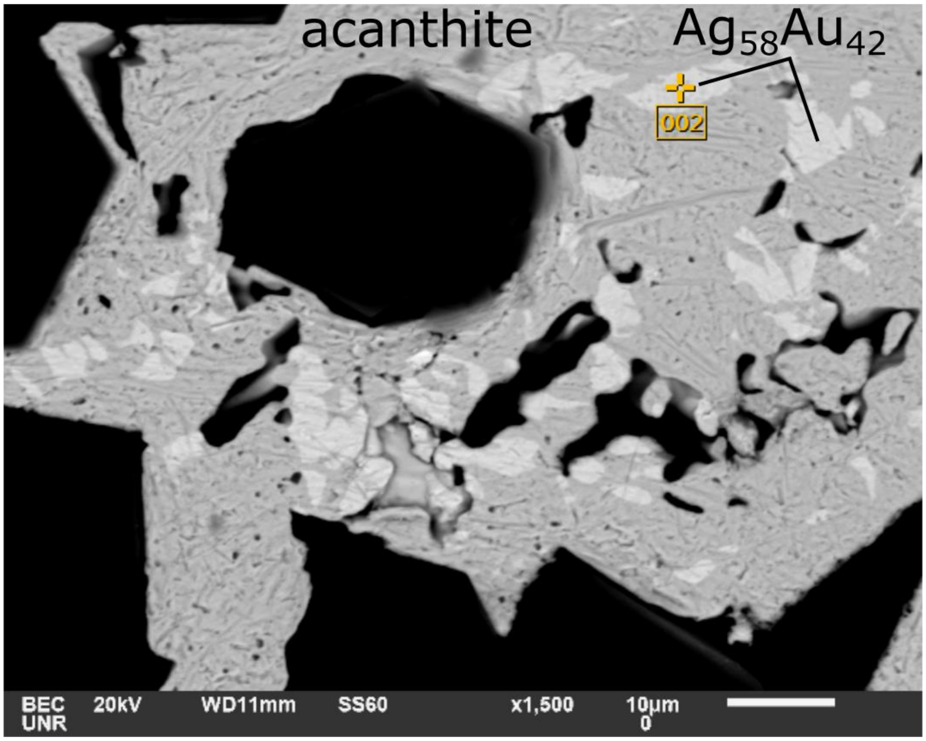

Figure F-26. Electrum (wt. %) within acanthite in sample MP-5 from the Star & Great Western claims near Mt. Patterson.

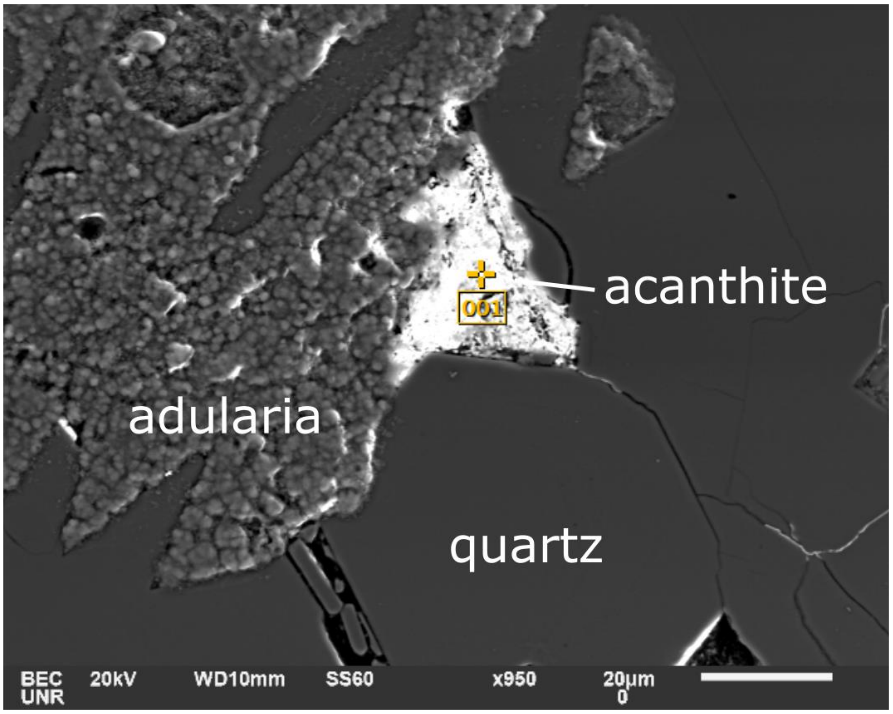

Figure F-27. Acanthite, adularia, and quartz in sample MtPat from the Star & Great Western claims near Mt. Patterson.

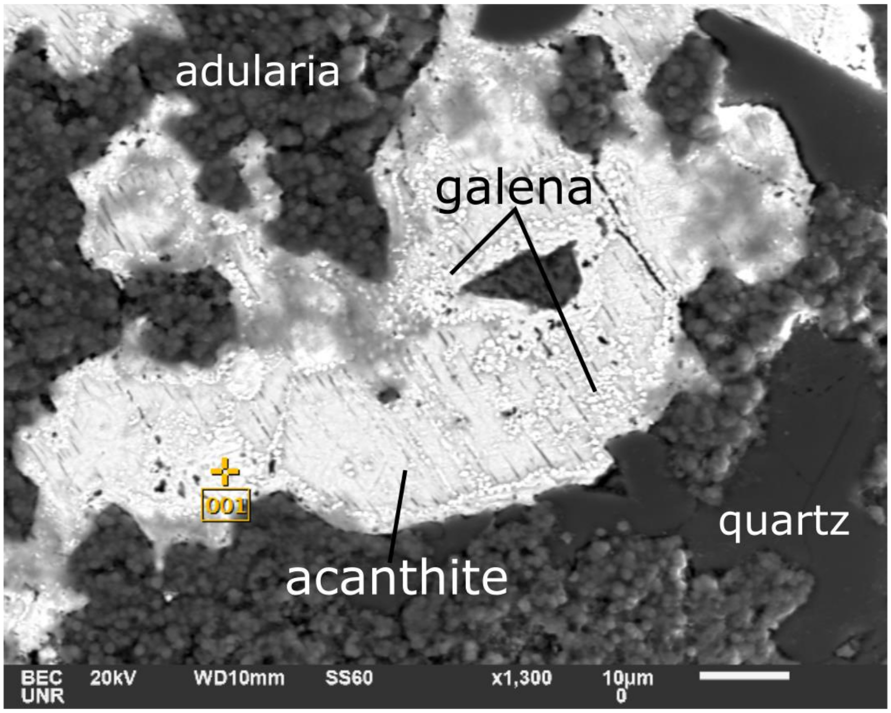

Figure F-28. Galena and fine-grained electrum (?) in acanthite in sample MtPat from the Star & Great Western claims near Mt. Patterson.

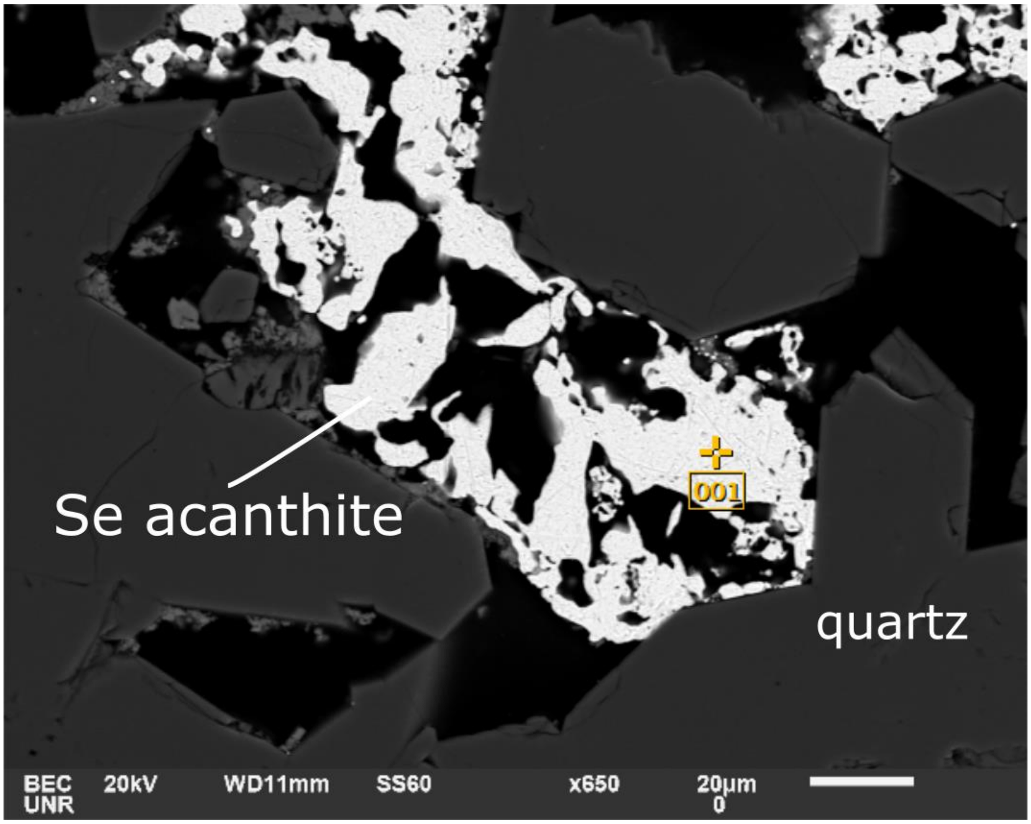

Figure F-29. Se-bearing acanthite within a void in euhedral quartz in sample MP-5 from the Star & Great Western claims near Mt. Patterson.

Plate I. Geologic Map of the Patterson Mining District, Sweetwater Mountains, Mono County, California and Lyon County, Nevada

Carli Balogh

2016

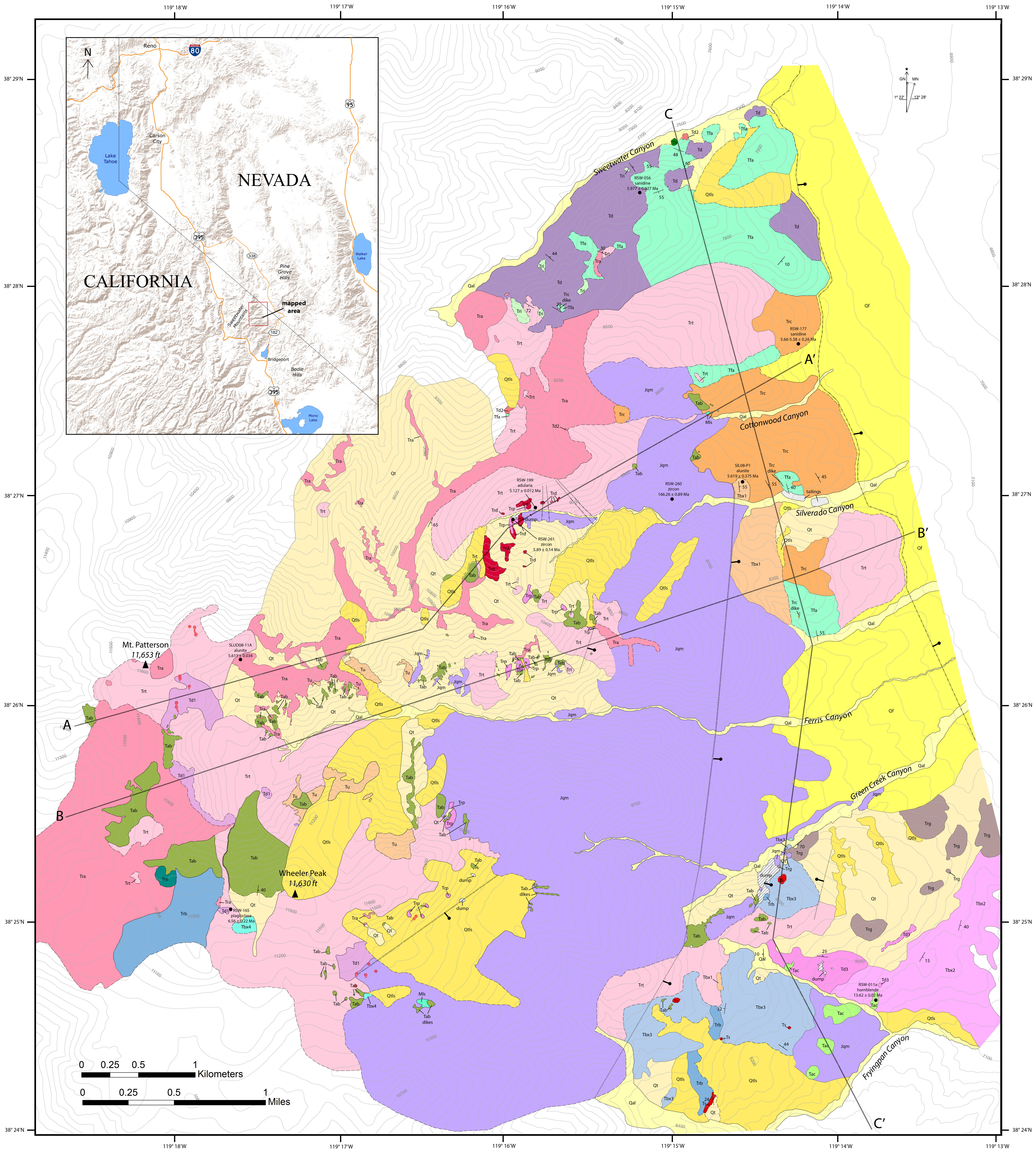

1:10,000
NAD 1983
Contour interval 100 feet

Topography generated from a DEM
acquired from the National Elevation Dataset

Legend

Quaternary

Qal	alluvium and colluvium
Qf	alluvial fan deposits
Qt	talus deposits
Qtls	land slide deposits
Dump	Dump material
Tailings	Mill tailings

Tertiary

Northern portion of map

Tb	Basaltic andesite. Vesicular, brown-red, and largely aphanitic.
Tfa	Tuff a. Consists of two members, one homogeneous white to greenish tuff containing sparse angular clasts of dacite glass and white lithic fragments, the other a red-pink to grey layered lapilli tuff with <5 cm lithics fragments, cross-bedding, and local lenses of sandstone and gravel. Matrix is silt-to-sand sized ash.
Tri	Rhyolite intrusion containing 4-7 mm sanidine phenocrysts (10-15%) in a white to green fine-grained matrix.
Trt	Rhyolite tuff breccia. Block + ash flow associated with Tra. Contains subangular clasts of Tra and pumice in a matrix of ash. Clasts are usually 1-4 cm but can be up to 1 m in width. Orange-tan and mottled.
Tra	Rhyolite a. Flow banded, fissile with <3 mm quartz and feldspar phenocrysts (3-4%). Red to pink on weathered surfaces, can have <7 mm vesicles. Altered to illite and/or kaolinite.
Trp	Rhyolite porphyry. Grey- green with .5-2 cm orthoclase (2-4%), 1 mm plagioclase (1%), 1-3 mm biotite (5%) phenocrysts, locally as glomerocrysts, and minor sphene. Occurs as a >8 m wide silicified dike and shallow intrusions. U-Pb zircon date of 5.9 ± 0.12 Ma.
Trd	Rhyolite d. Fine-grained, clay altered to silicified, with <1 mm quartz (1%), 2 mm sanidine (1%), 2 mm biotite (1%) and 3 mm plagioclase (2%). All phenocrysts except for quartz are leached in Silverado Canyon. Occasional columnar jointing.
Tab	Trachyandesite b. Dark grey to purple-teal. Porphyritic with 2-4mm corroded hornblende (2-5%) and 1-5 mm plagioclase laths (5-10%). Small associated lahars.
Tbx1	Breccia 1. Debris flow of blocks of Trc up to 1 m in width cemented by quartz and alunite. Commonly contains voids. Occurs in resistant knobs.
Trc	Rhyolite c. Porphyritic, spherulitic, flow banded with a green to pink glassy matrix. 2-6 mm sanidine (4%) phenocrysts with 1-2 mm quartz and plagioclase (2%). ^{40}Ar/^{39}Ar sanidine date of 5.66 ± 0.26 Ma.
Td	Trachydacite. Porphyritic with 2-6 mm sanidine phenocrysts (10%) and 1-3 mm biotite (3%) and hornblende (3%). Purple-grey and often flow-banded. ^{40}Ar/^{39}Ar sanidine date of 5.977 ± 0.012 Ma.
Td2	Trachydacite 2. Dark reddish to purple with 2-4 mm feldspars (5%) and 1-2 mm biotite (1%) and hornblende (1%) phenocrysts. Contains wavy glassy layers.
Tre	Rhyolite e. Porphyritic with 1-2 mm biotite and hornblende (2% each), and 2-3 mm feldspars (1%) and quartz (3%) phenocrysts. Light grey matrix.
Td1	Trachydacite 1. Dark purple and glassy with <1 mm biotite (3%) phenocrysts and feldspar (1%) phenocrysts. ^{40}Ar/^{39}Ar plagioclase date of 6.56 ± 0.22 Ma.

Southern portion of map

Ts	Sinter composed on very fine grained layers of chalcedony deposited by a hot spring
Tbx4	Breccia 4. Hydrothermal breccia with angular to subrounded clasts of quartz and country rock cemented by silica and iron oxides.
Tbx3	Breccia 3. Clast rich volcaniclastic breccia of poorly sorted clasts of various volcanic rocks with occasional layers of finely-layered black tuff. Most clasts are larger than 4 cm.
Trb	Rhyolite b. Fine-grained red-purple rhyolite with abundant <2 mm biotite (3-5%), 1-3 mm plagioclase (1-2%), 2-7 mm sanidine (2-5%), and sparse 1-2 mm hornblende (<1%) phenocrysts. Weakly flow banded.
Tbx2	Breccia 2. Clast-supported volcaniclastic breccia with very large clasts of clay altered dacite from 0.3 to 3 m wide. Forms flat terraces in Fryingpan Canyon.
Td3	Trachydacite 3. Purple, flow-banded with <3 mm quartz (2%), 2-5 mm sanidine (3%), and 3-4 mm biotite and hornblende (4-5%) phenocrysts.
Trg	Rhyolite g. Purple, spherulitic flow banded rhyolite with 1-2 mm sanidine and quartz (1-5% total) phenocrysts and sparse biotite (<1%) crystals. ^{40}Ar/^{39}Ar date of 5.549 Ma ± 0.005 Ma.
Tac	Trachyandesite c. Porphyritic with 10% hornblende phenocrysts up to 7 mm in a dark grey matrix. ^{40}Ar/^{39}Ar hornblende date of 13.62 ± 0.02 Ma. May correlate with trachyandesite of Masonic in the Bodie Hills.

Mesozoic and Paleozoic

Jqm	Jurassic quartz monzonite Intrusion containing orthoclase megacrysts 1-3 cm in a medium grained interlocking matrix of plagioclase and lesser quartz + biotite. U-Pb zircon date of 166.26 ± 0.8 Ma.
Mls	Paleozoic to Mesozoic limestone Micritic marine limestone composed of crystalline calcite with locally interbedded siltstones and volcanic rocks. Potentially belong to the Pine Nut assemblage of Triassic to Jurassic age.

Additional map symbols

- Contact, certain
- Contact, approximately located
- Contact, concealed
- Normal fault, certain
- Normal fault, approximately located
- Normal fault, suspected
- Strike and dip, bedding
- Strike and dip, igneous foliation
- Vein
- Vein, concealed
- Cross section line
- ● Geochronology sample site

Cross sections

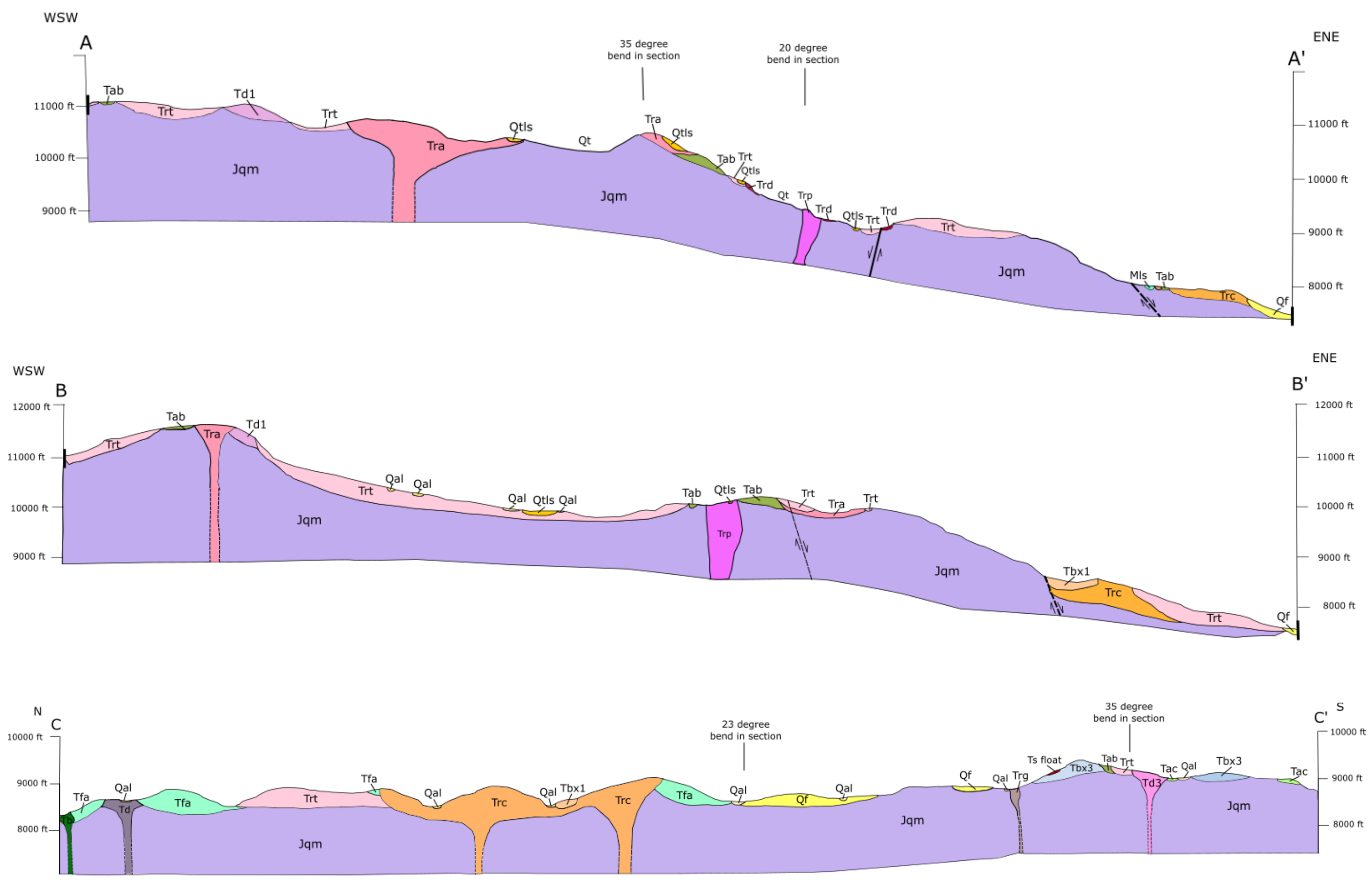

Plate II. Map of alteration mineral assemblages in the Patterson mining district